



**Università degli Studi di Napoli “Federico II”**

**A thesis submitted for the degree of Doctor of Philosophy in  
Industrial Engineering (XXXI Cycle - October 2018)**

***Innovative Solutions  
for Navigation and Mission Management  
of Unmanned Aircraft Systems***

***Rita Fontanella***

**Supervisor:**

***Prof. Domenico Accardo***

*Ai miei genitori, con affetto*  
*(To my parents, with love)*

# Abstract

The last decades have witnessed a significant increase in Unmanned Aircraft Systems (UAS) of all shapes and sizes. UAS are finding many new applications in supporting several human activities, offering solutions to many dirty, dull, and dangerous missions, carried out by military and civilian users. Consequently, many industries are considering to employ UAS as a replacement of human driven applications. Currently, UAS perform several civilian missions, among them: traffic monitoring air pollution monitoring, precision agriculture, mapping, on-demand package delivery, inspection of infrastructure, and law enforcement. Recent acquisitions by Google, Facebook, and Amazon suggest there is keen interest in strategic positioning as this market, technology, and regulations mature.

Today, limited access to the airspace is the principal barrier to the realization of the full potential that can be derived from UAS capabilities. The integration of UAS operations is one of the key challenges of the European and American programs Single European Sky ATM Research (SESAR) and Next Generation Air Transportation System (NextGen). These programs aim at increasing the airspace safety and efficiency as well as at improving the whole air traffic management system.

Given the number and types of UAS operations envisioned, it is clear that the existing Air Traffic Management (ATM) system cannot cost-effectively scale to deliver services for UAS. The nature of most of these operations does not require direct interaction with the ATM system. Therefore, it is globally acknowledged the need to develop a parallel air traffic management system, named Unmanned Traffic Management or UTM system, separate from, but collaborative with the ATM system.

In the United States, Federal Aviation Administration, NASA, other federal partner agencies and industry are collaboratively developing the UAS Traffic Management system. In Europe, gathering experts from aviation, research and academia, the Concept of Operation for European UTM Systems (CORUS) consortium is developing a concept of

operations for U-Space, the European system for management of UAS. The Civil Aviation Administration of China is defining the use of a civil UAS Operation Management System, while the Japanese UTM system is being built by the Japan UTM Consortium and a national project founded by New Energy and Industrial Technology Development.

Several stakeholders are working in defining the best solutions to integrate UAS operations in the civil airspace. However, significant challenges must still be addressed. In this thesis, the main technical and operational issues, considered among the principal inhibitors to the integration and wide-spread acceptance of UAS, are analysed and two types of key enabling technologies for safe UAS operations are identified:

- Technologies for autonomous navigation. Autonomous navigation of UAS is typically based on the integration of low-cost Global Navigation Satellite Systems (GNSS) and inertial sensors. However, traditional gyroscopes can be either too expensive or bulky, especially for small UAS applications. In recent years, the improvement of micro-fabrication techniques has allowed the development of Micro Electro-Mechanical Systems inertial sensors, well-suited for UAS navigation due to their characteristics of low-cost, light-weight, and low power consumption. However, they suffer more than traditional inertial sensors for environment dependent errors.
- Technologies for mission management. Novel solutions are needed to support the UTM system in monitoring and coordinating the operations of several small UAS, handling the diversity in UAS and payload types and assessing a broad range of mission conditions.

The aim of this thesis is to support the safe integration of UAS operations, taking into account the user's requirements and flight regulations. To achieve this aim, two objectives are defined, i.e. improving the navigation performance of UAS by exploiting low-cost sensors and proposing novel methods to improve UAS mission management.

#### A. Improving the navigation performance of UAS by exploiting low-cost sensors.

Two approaches are proposed to improve dead-reckoning performance for handling intermittent GNSS coverage in the integrated navigation system:

- Thermal Compensated Zero Velocity Update (TCZUPT) filter.

It is a novel method to estimate and correct MEMS gyros bias, which drifts with temperature with a strongly non-linear trend. While the traditional process is characterized by a cascading of two processing steps, i.e. thermal calibration by exploiting polynomial fitting and Zero Velocity Update (ZUPT) filter, the TCZUPT filter embeds the compensation of thermal effect on bias in the filter itself and uses Back-Propagation Neural Networks to build the calibration function.

Experimental tests have been performed in the laboratory of G.M.A. S.r.l.<sup>TM</sup> company, by exploiting the Attitude and Heading Reference System (AHRS) Axitude AX1-[ ]<sup>TM</sup> in two conditions, i.e. 1) nominal condition, and 2) residual bias after rough initial alignment. Results show that the TCZUPT filter is faster in mapping significant bias variations and presents better performance in the overall testing period. Moreover, no calibration pre-processing stage is required to keep measurement drift under control, improving the accuracy, reliability, and maintainability of the AHRS processing software.

- Redundant configuration of inertial sensors.

A calibration solution for consumer grade MEMS gyros, which exploits a redundant configuration of sensors, is proposed in this thesis. It is tested by exploiting the world's densest sensor board, the SensorTile<sup>TM</sup> by STMicroelectronics<sup>TM</sup>, in a cubic configuration.

Results show that the redundancy of each axis in the navigation framework is efficiently improved, as well as the accuracy of the whole IMU. Indeed, it is able to make full use of the redundant observation data of sensors, by averaging multiple measurements about the same axis. The result is a partial self-calibration of typical inertial sensors biases, and a consequent reduction of the uncertainty in attitude determination.

This activity is the object of the project named "POLYTILE: Self-Compensating IMU Exploiting Redundant Configuration on Regular POLYhedron of SensorTILEs" awarded for the Special Mention at the IEEE International Sensors and Measurement Systems Student Contest 2018, at Houston, TX, USA (14-17 May 2018).

## B. Proposing novel methods to improve UAS mission management.

Two solutions are proposed in this thesis to support the UTM system in monitoring and coordinating the operations of large-scale UAS missions, speeding up the flight authorization process and supporting the increasing level of autonomy in UAS operations:

- Trajectory prediction for small UAS.

A trajectory prediction tool for small UAS, based on Learning Vector Quantization (LVQ) Neural Networks, is proposed in this thesis. It is tested by flying the DJI Phantom 4<sup>TM</sup> in waypoint mode. Telemetry data acquired in real-time are used to train and test the LVQ Neural Network.

Results show that, by exploiting flight data collected when the Phantom 4<sup>TM</sup> executes a pre-assigned flight path, the tool is able to predict the time taken to fly generic trajectory elements. Moreover, being self-adaptive in constructing a mathematical model after several training and testing steps, LVQ Neural Networks allow creating different models for the myriad of different UAS types in several environmental conditions.

- Standardized procedures for decision-making process.

The thesis proposes a software tool, aimed at supporting standardized procedures for decision-making process to identify UAS types, payload, and prescriptions suitable for any type of missions that can be authorized standing flight regulations. The tool is developed in JAVA and is linked to an external eXtensible Markup Language database composed by several UAS and payload types, which can be stored on a different server and updated online, considering all new technologies that will be developed with time.

The mission considered to test the tool is the aerial photography of a field, by using a multispectral camera to obtain information related to the productivity of the soil. By setting the mission requirements and the weather conditions in the user-input interface, the tool identifies the required and recommended on-board equipment and suggests off-the-shelf solutions to realize the customer needs, taking into account the current regulations. Moreover, by using a scoring system defined by the user, the tool classifies the available UAS/payload configurations, selecting the most suitable to the mission.

This activity has been carried out in collaboration with the Ecole de l'Air, France.

The investigated technologies make great impact to enable large-scale UAS operations, particularly in view of the increasing number of small UAS applications. Indeed, they can be exploited for several enabling technologies, such as, a Mission Manager for UAS operations, Sense & Avoid systems, surveillance systems, and flight termination systems. The proposed solutions will be exploited in the Laboratory for Innovative Flight Technologies (LIFT), realized to support the increasing local request for professional activities carried out by exploiting small UAS.

**Keywords:** Unmanned Aircraft Systems; Navigation; Mission Management.

# Acknowledgements

First and foremost, my deepest appreciation and gratitude goes to my supervisor, Professor Domenico Accardo for providing me constant support, advice and wisdom throughout my PhD. I would like to thank him for being an exceptional guide throughout this journey and for giving me the opportunity to get international experiences and to collaborate with industry partners. These opportunities opened my research horizon, pushing me to do always my best.

I would like to thank everyone in the Aerospace Systems Team of the Department of Industrial Engineering at the University of Naples Federico II. It has been a great privilege and a pleasure to be part of this team throughout my PhD. Very special thanks go to Professor Giancarmine Fasano for his precious advice on Unmanned Aircraft Systems and to Professor Michele Grassi and Professor Giancarlo Rufino for their constant support and advice since my Bachelor's degree thesis.

Very special thanks go to Professor Rosario Schiano Lo Moriello, Professor Leopoldo Angrisani and the Centre for Advanced Metrology Services (CeSMA) at the University of Naples Federico II, for their precious support on my research on MEMS-based IMUs, especially on the redundant configuration of consumer grade inertial sensors. I would like to thank Professor Rosario Schiano Lo Moriello, for his happiness and willingness and for becoming a real friend.

I am exceedingly grateful to Professor Washington Yotto Ochieng, Head of the Centre for Transport Studies at Imperial College London, and Dr Arnab Majumdar, Director of the Lloyds Register Foundation Transport Risk Management Centre at the Centre for Transport Studies, for giving me the great opportunity to conduct a 6-months visiting period at Imperial College London. I would like to thank them for letting me being part of their great research team and for providing me an insightful support during the writing of this thesis. I

also would like to thank everyone in the Centre for Transport Studies, especially Dr Elena Psyllou, for having made my life in London so wonderful.

Very special thanks go to MBDA for supporting my initial research activities on MEMS-based IMUs. In particular, I would like to thank Stefano Cimmino and Egidio Caricati.

I am grateful to Generale Meccatronica Applicata (G.M.A) for making its laboratories and equipment available for several experimental tests to support my research activities on improving navigation performance of UAS by exploiting low-cost sensors. In particular, I would like to thank Dr Alessandro Simonetti, Domenico De Simone, and Giovanni Lucignano.

Very special thanks go to STMicroelectronics for providing the SensorTiles™ used to develop the redundant IMU prototype. In particular, I would like to thank Mauro D'Angelo for his precious advice.

To Antonio, for being by my side throughout this journey with his constant encouragement.

To my grandmother, nonna Rita, for her support in all my life and for being always so great!

To my beloved parents, Leonardo and Elena Fontanella, for their constant support and belief in me. Thank you for encouraging me in reaching my dreams and for being an exceptional example of life that makes me the person I am today. This thesis is for you.

# Contents

Abstract.....	iii
Acknowledgements .....	viii
List of Figures.....	xiv
List of Tables.....	xvii
List of Acronyms.....	xviii
1. Introduction .....	1
1.1.    Background to the research.....	1
1.2.    Key enabling technologies for UAS .....	2
1.2.1.    Technologies for autonomous navigation .....	3
1.2.2.    Technologies for mission management.....	4
1.3.    Developed research solutions .....	4
1.3.1.    Improving navigation performance of UAS by exploiting low-cost sensors.....	6
1.3.1.1.    Industrial grade MEMS gyros .....	7
1.3.1.2.    Consumer grade MEMS gyros.....	7
1.3.2.    Novel methods for UAS mission management.....	8
1.3.2.1.    UAS trajectory prediction .....	8
1.3.2.2.    Standardized procedures for decision-making.....	8
1.4.    Summary of thesis chapters .....	9
2. Unmanned Aircraft Systems: State-of-the-Art and Challenges .....	10
2.1.    General context about Unmanned Aircraft Systems.....	10
2.2.    Classification.....	15
2.3.    Missions .....	17
2.4.    Research trends .....	19
2.4.1.    Research challenges .....	19
2.4.2.    Future UAS applications .....	22
3. Safe Airspace Access of UAS .....	24
3.1.    Introduction.....	24
3.2.    Airspace integration approaches .....	25
3.3.    Unmanned Traffic Management system.....	26
3.3.1.    Introduction .....	26
3.3.2.    Operational framework .....	28
3.3.3.    Enabling technologies .....	29

3.4.	Technology limitations for safe integration of UAS.....	30
3.4.1.	GNSS errors .....	31
3.4.1.1.	Sources of uncertainty .....	31
3.4.1.2.	Intentional hacking and signal jamming .....	34
3.4.2.	Collision avoidance .....	34
3.4.2.1.	Air traffic.....	34
3.4.2.2.	Risks to people and property on the ground.....	35
3.4.3.	Standards addressing UAS systems and operations.....	36
4.	Solutions for Autonomous Navigation .....	37
4.1.	Overview on MEMS-based IMUs for UAS navigation.....	37
4.1.1.	Introduction .....	37
4.1.2.	MEMS gyroscopes .....	39
4.1.2.1	Introduction .....	39
4.1.2.2	Principle of operation .....	39
4.1.2.3	Performance grades .....	41
4.1.3.	MEMS accelerometers .....	43
4.1.4.	UAS navigation .....	44
4.1.4.1.	Magnetometer/INS integration.....	44
4.1.4.2.	GNSS/INS integration.....	46
4.1.4.3.	Data fusion techniques .....	49
4.1.4.4.	Integrity monitoring .....	52
4.2.	Improving thermal compensation of MEMS gyro bias .....	54
4.2.1.	MEMS gyro bias temperature dependence model .....	55
4.2.2.	Traditional bias estimation and compensation process.....	56
4.2.2.1.	Thermal compensation through polynomial fitting.....	57
4.2.2.2.	ZUPT filter .....	58
4.2.3.	Contribution of this thesis .....	64
4.2.3.1.	Bias drift modelling through Back-Propagation Neural Networks .	65
4.2.3.2.	Thermal Compensated ZUPT filter.....	66
4.2.4.	Experimental tests .....	68
4.2.5.	Comparison of polynomial and BPNNs thermal calibration .....	72
4.2.5.1.	Polynomial order selection.....	72
4.2.5.2.	BPNNs structure selection .....	73
4.2.5.3.	Effect of polynomial and BPNNs calibration on flight attitude.....	75
4.2.6.	TCZUPT filter implementation and testing .....	78
4.2.6.1.	Derivation of thermal correction function.....	78
4.2.6.2.	ZUPT & TCZUPT: comparative performance analysis.....	79
4.3.	Improving consumer grade MEMS gyros performance by redundancy.....	85

4.3.1.	Introduction .....	85
4.3.2.	Exploiting redundancy .....	86
4.3.3.	Reference hardware system.....	88
4.3.4.	System integration.....	90
4.3.4.1.	Hardware configuration.....	91
4.3.4.2.	Software implementation .....	92
4.3.5.	Relative alignment among MEMS gyros .....	93
4.3.6.	Application and results .....	95
5.	Solutions for Mission Management.....	98
5.1.	UAS Trajectory Prediction .....	98
5.1.1.	Introduction .....	98
5.1.2.	UAS trajectory model.....	100
5.1.3.	Trajectory prediction through LVQ Neural Networks.....	102
5.1.3.1.	LVQ Neural Networks general description.....	102
5.1.3.2.	LVQ Neural Networks for trajectory prediction .....	104
5.1.4.	Experimental tests .....	105
5.1.4.1.	Tests description.....	105
5.1.4.2.	LVQ Neural Networks training data .....	107
5.1.5.	Tool application and results .....	112
5.2.	Standardized Procedures for Decision-Making .....	114
5.2.1.	Introduction .....	114
5.2.2.	Methodology .....	115
5.2.2.1.	Tool description.....	115
5.2.2.2.	Missions vs. features .....	116
5.2.2.3.	Features vs. equipment.....	119
5.2.2.4.	Missions vs. equipment.....	121
5.2.3.	System architecture .....	124
5.2.3.1.	Reference packages .....	124
5.2.3.2.	“Input/Output” package.....	125
5.2.3.3.	“XML Data” package.....	127
5.2.3.4.	“Test” package .....	127
5.2.3.5.	“Scoring” package.....	129
5.2.4.	Application and results.....	130
6.	Conclusions and Future Developments .....	133
6.1.	Improving navigation performance of UAS by exploiting low-cost sensors .....	134
6.1.1.	Thermal Compensated Zero Velocity Update filter.....	134
6.1.2.	Redundant configuration of MEMS inertial sensors.....	135

6.2.	Novel solutions for UAS mission management.....	136
6.2.1.	Trajectory prediction.....	136
6.2.2.	Standardized procedures for decision-making.....	137
6.3.	Future developments.....	137
6.4.	Publications and awards.....	139
References	.....	141

# List of Figures

Figure 1. Flow-chart of the research carried out in this thesis. ....	6
Figure 2. General organization of this thesis. ....	9
Figure 3. Northrop Grumman RQ-4 Global Hawk. ....	11
Figure 4. Northrop Grumman’s MQ-4C Triton. ....	11
Figure 5. Predator B developed by General Atomics. ....	11
Figure 6. Aerovironment’s pioneering solar-powered HELIOS. ....	12
Figure 7. Example of a multicopter UAS (DJI Phantom 4 <sup>TM</sup> ), with the remote controller. .	13
Figure 8. Projected global UAS market in 2020, by area of application, in billion U.S. dollars (Fortune; Frost & Sullivan ID 431717). ....	13
Figure 9. Projected commercial UAS revenue worldwide from 2015 to 2025, in million U.S. dollars (Tractica ID 607922). ....	14
Figure 10. Top industries using UAS (BI Intelligence). ....	14
Figure 11. NATO UAS Classification. ....	15
Figure 12. Aerovironment Hummingbird. ....	23
Figure 13. UTM operational framework. ....	28
Figure 14. Example of UAS avionics architecture (RAMA UAV Control System 2009). ....	38
Figure 15. Schematics of a z-axis MEMS gyroscope. ....	40
Figure 16. Bias and scale factor stability performance for traditional gyro technologies, such as mechanical, FOG, RLG and DTG, and MEMS gyros (revised version of the figure in (Schmidt 2010)). ....	42
Figure 17. Earth’s magnetic field (revised version of the figure in (Moir <i>et al.</i> 2013)). ....	45
Figure 18. Earth’s magnetic field components (revised version of the figure in (Moir <i>et al.</i> 2013)). ....	46
Figure 19. Loosely coupled GNSS/INS integration. ....	48
Figure 20. Tightly coupled GNSS/INS integration. ....	48
Figure 21. Ultra-tightly coupled or deeply integrated GNSS/INS system. ....	49
Figure 22. Kalman filter scheme. ....	50
Figure 23. ZUPT filter block diagram model. ....	59
Figure 24. Standard ZUPT filter: $a$ is the accelerometer output, $\omega_{RAW}$ is the raw gyro data, $\omega_{CALIBRATED}$ is the calibrated gyro data and $b_a$ and $b_g$ are respectively the accelerometer and gyro bias. ....	62
Figure 25. Flow chart of the Back Propagation Neural Network training process. ....	66
Figure 26. TCZUPT filter: $a$ is the accelerometer output, $\omega_{RAW}$ is the raw gyro data and $b_a$ and $b_g$ are respectively the accelerometer and gyro bias. ....	67

Figure 27. Axitude AX1-[ ]™.....	68
Figure 28. Setup equipment.....	71
Figure 29. Gyro output ( $\omega_x, \omega_y, \omega_z$ ) vs. temperature for the soak test. ....	71
Figure 30. Gyro output ( $\omega_x, \omega_y, \omega_z$ ) vs. temperature for the ramp test. ....	72
Figure 31. Polynomial fitting performance parameter $Sr_{PF}$ vs. polynomial order. ....	73
Figure 32. Neural Network performance parameter $Sr_{NN}$ vs. number of hidden layers neurons.....	74
Figure 33. Structure of the BPNN adopted for bias drift modelling. ....	75
Figure 34. Evolution of $\Delta\omega$ parameter versus temperature.....	77
Figure 35. Trend of the rotation angle $\theta$ with temperature ( $\Delta\omega_{MAX}$ ). ....	77
Figure 36. Trend of the rotation angle $\theta$ with temperature ( $\Delta\omega_{RMS}$ ). ....	78
Figure 37. Performance parameter $Sr_{TCZUPT}$ vs. number of hidden layers neurons (TCZUPT filter). ....	79
Figure 38. Input data of the standard ZUPT filter. ....	80
Figure 39. Input data of the TCZUPT filter. ....	81
Figure 40. Gyro output bias (nominal condition, x-axis). ....	81
Figure 41. Gyro output bias (nominal condition, y-axis). ....	81
Figure 42. Gyro output bias (nominal condition, z-axis). ....	82
Figure 43. Gyro output bias (residual error of 15 deg/h, x-axis). ....	82
Figure 44. Gyro output bias (residual error of 15 deg/h, y-axis). ....	82
Figure 45. Gyro output bias (residual error of 15 deg/h, z-axis). ....	83
Figure 46. a) SensorTile board along with all integrated components, b) cradle expansion board. ....	90
Figure 47. Redundant IMU prototype designed and realized by using six SensorTiles™. ....	91
Figure 48. System integration (Hardware & Software). ....	93
Figure 49. Faces of a cubic configuration of MEMS inertial sensors. ....	95
Figure 50. Triaxial MEMS gyro output.....	96
Figure 51. Trend of the rotation angle $\theta$ with time.....	96
Figure 52. Example of a generic UAS trajectory between the initial point A and the final point B. ....	100
Figure 53. Symmetric combination of features. ....	102
Figure 54. LVQ Neural Network structure adopted for trajectory prediction.....	105
Figure 55. LVQ Neural Network training process. ....	105
Figure 56. DJI Phantom 4™.....	106
Figure 57. Selected waypoints.....	107
Figure 58. Trajectory elements used to train the LVQ Neural Network. ....	108
Figure 59. 1 <sup>st</sup> training element in the local projected coordinate system. ....	108
Figure 60. 2 <sup>nd</sup> training element in the local projected coordinate system. ....	109
Figure 61. 3 <sup>rd</sup> training element in the local projected coordinate system.....	109
Figure 62. 4 <sup>th</sup> training element in the local projected coordinate system.....	110
Figure 63. Trajectory elements used to test the LVQ Neural Network.....	112
Figure 64. 1 <sup>st</sup> testing element in the local projected coordinate system.....	113

Figure 65. 2 <sup>nd</sup> testing element in the local projected coordinate system. ....	113
Figure 66. Tool processing logic. ....	116
Figure 67. Tool Architecture. ....	124
Figure 68. Flow-chart of the tool. ....	125
Figure 69. Layout of the user-input interface. ....	126
Figure 70. Layout of the output interface. ....	126
Figure 71. Test to compare the UAS maximum velocity ( $V_{UAS}$ ) with the wind velocity ( $V_{wind}$ ). ....	128
Figure 72. Required HFOV. ....	128
Figure 73. Flow-chart of the testing phase. ....	129
Figure 74. Scoring system transfer function. ....	130
Figure 75. User-input interface (precision agriculture). ....	132
Figure 76. Output interface. ....	132

# List of Tables

Table 1. Aggravating and mitigating factors (Ministry of Defence & Military Aviation Authority 2016). .....	16
Table 2. Gyro Grades Based on Bias Stability (KVH 2014).....	43
Table 3. Angular random walk $\sigma_{ARW}$ and gyro bias instability $\sigma_{GBI}$ (ZUPT filter). .....	69
Table 4. Velocity random walk $\sigma_{VRW}$ and accelerometer bias instability $\sigma_{ABI}$ (ZUPT filter). .....	69
Table 5. Angular random walk $\sigma_{ARW}$ and gyro bias instability $\sigma_{GBI}$ (TCZUPT filter). ...	69
Table 6. Velocity random walk $\sigma_{VRW}$ and accelerometer bias instability $\sigma_{ABI}$ (TCZUPT filter). .....	69
Table 7. Time in which the flight attitude accuracy meets the imposed requirements ( $\Delta\omega_{MAX}$ ).....	77
Table 8. Time in which the flight attitude accuracy meets the imposed requirements ( $\Delta\omega_{RMS}$ ).....	78
Table 9. Mean value of residuals of the moving average.....	80
Table 10. RMS error of ZUPT and TCZUPT filters. ....	84
Table 11. Convergence time of the ZUPT and TCZUPT filters in case of residual error of 15 degree/h. ....	84
Table 12. Mean and Standard Deviation of the RMS error (nominal conditions, 5 data sets). .....	85
Table 13. Mean and Standard Deviation of the RMS error (residual error of 15 degree/h, 5 data sets). .....	85
Table 14. Fraction of gyro bias standard deviation for each redundant cubic configuration. ....	87
Table 15. Time in which the flight attitude accuracy meets the imposed requirements. ..	97
Table 16. DJI Phantom 4 <sup>TM</sup> specifications. ....	106
Table 17. LVQ Neural Network Performance .....	114
Table 18. Mission vs. features compliance matrix. ....	118
Table 19. Features vs. equipment compliance matrix (• - necessary; ✓ - optional; no symbol indicates incompatibility). .....	120
Table 20. Missions vs. required equipment (• - necessary; ✓ - optional; no symbol indicates incompatibility). .....	123
Table 21. Structure of the XML databases. ....	127
Table 22. Mission requirements (precision agriculture).....	131
Table 23. Target and maximum (or minimum) values for the scoring system (precision agriculture). .....	131
Table 24. Best UAS/payload configurations (precision agriculture). ....	131

# List of Acronyms

ABL	Atmospheric Boundary Layer
ADC	Analog-to-Digital Converter
ADS-B	Automatic Dependent Surveillance – Broadcast
AGC	Automatic Gain Control
AGL	Above Ground Level
AHRS	Attitude and Heading Reference System
AI	Artificial Intelligence
AIS	Automated Identification System
ANFIS	Adaptive Neural Fuzzy Information System
ANNs	Artificial Neural Networks
AP	Airborne Part
AUVSI	Association of Unmanned Vehicle Systems International
BLE	Bluetooth Low Energy
BLOS	Beyond Line of Sight
BPNNs	Back-Propagation Neural Networks
BRLOS	Beyond Radio Line of Sight
BVLOS	Beyond Visual Line of Sight
CAAC	Civil Aviation Administration of China
CMOS	Complementary Metal Oxide Semiconductor
CORUS	Concept of Operation for European UTM Systems
CS	Chip Select
DAM	Data Acquisition Module
DOP	Dilution of precision
EASA	European Aviation Safety Agency
EKF	Extended Kalman Filter
EO	Electro Optical
ERAINT	Evaluation of the RPAS-ATM Interaction in Non-Segregated Airspace
ERAST	Environmental Research and Sensor Technology
EU	European Union
FAA	Federal Aviation Administration

FOG	Fiber Optic Gyros
GCS	Ground Control Station
GI-RAIM	GNSS Inertial - RAIM
GNSS	Global Navigation Satellite System
GPIO	General Purpose I/O
GPS	Global Positioning System
GS	Ground Station
GUI	Graphical User Interface
H	High
HAL	Horizontal Alert Limit
HALE	High-Altitude Long Endurance
HFOV	Horizontal Field of View
HPL	Horizontal Protection Level
IC	Inter Integrated Circuit
IMUs	Inertial Measurement Units
INS	Inertial Navigation System
IR	Infrared Radiation
JUTM	Japan UTM Consortium
L	Low
LIDAR	Laser Identification Detection and Ranging
LKF	Linearized Kalman Filter
LMS	Least Mean Squares
LOS	Line of Sight
LRF/D	Laser Range Finder and/or laser Designator
LSB	Least Significant Bit
LVQ	Learning Vector Quantization
M	Medium
MALE	Medium-Altitude Long-Endurance
MCC	Main Control Computer
MEMS	Micro Electro-Mechanical Systems
MISO	Master Input/Slave Output
MMW	Millimeter Wave
MOSI	Master Output/Slave Input
MTOW	Maximum Takeoff Weight

NAS	National Airspace System
NASA	National Aeronautics and Space Administration
NATO	North Atlantic Treaty Organization
NED	North-East-Down
NEDO	New Energy and Industrial Technology Development
NextGen	Next Generation Air Transportation System
NU	Navigation Unit
P2P	Point to Point
PDF	Probability Density Function
PPP	Precise Point Positioning
PVT	Position, Velocity, Time
RA	Resolution Advisories
RC	Radio Control
RMS	Root Mean Square
RNP	Required Navigation Performance
RPAS	Remotely Piloted Air System
RSTA	Reconnaissance, Surveillance, and Target Acquisition
RTK	Real Time Kinematic
SAA	Sense & Avoid
SAR	Synthetic Aperture Radar
SATCOM	SATellite COMmunication
SBAS	Spaced Based Augmentation System
SCU	Servo Control Unit
SESAR	Single European Sky ATM Research
SIGINT	SIGNals INTelligence
SPI	Serial Peripheral Interface
SWaP	Size, Weight, and Power
TA	Traffic Advisories
TAM	Three-Axis Magnetometer
TAWS	Terrain Awareness and Warning System
TCAS	Traffic alert and Collision Avoidance System
TCZUPT	Thermal Compensated Zero Velocity Update
UAS	Unmanned Aerial Systems
UAS-NAS	UAS Integration in the National Airspace System

UCAV	Unmanned Combat Aerial Vehicle
UKF	Unscented Kalman Filter
UNITE	UAV National Industry Team
UOMS	UAS Operation Management System
USART	Universal Serial Asynchronous Receiver-Transmitter
UTM	Unmanned Traffic Management
VLOS	Visual Line of Sight
WCU	Wireless Control Units
WDCU	Wireless Data Communication Unit
XML	eXtensible Markup Language
ZUPT	Zero Velocity Update



# Chapter 1

---

## Introduction

### 1.1. Background to the research

Since the beginning of the twentieth century, Unmanned Aerial Systems (UAS) have been encountered in an increasing number of applications (Kendoul 2012). They were developed to support several dull, dirty and dangerous missions, many driven by military needs (Francis 2016). Indeed, UAS offer a unique range of features, most notably ultra-long endurance and high-risk mission acceptance, which cannot be reasonably performed by manned aircraft (Degarmo 2004). Consequently, many industries are considering the opportunity to let UAS perform jobs traditionally done by humans, or never before done at all (Foina *et al.* 2015). These features, when coupled with advances in automation and sensor technologies, make a strong case for the rise of a robust civil, government, and commercial UAS market (Degarmo 2004).

The last several decades have witnessed an even more explosive increase in unmanned aircraft of all shapes and sizes, including an increasingly large number intended for civil and commercial applications. These applications include aerial photography, precision agriculture, infrastructure inspection, construction, insurance investigation, film and entertainment, wildlife and resources management, climate monitoring and observation,

search and rescue, newsgathering, security, and geographical surveys, to name just a few (Austin 2010).

Despite the potential of UAS across a range of economically beneficial and compelling applications, there are significant obstacles to their successful introduction and implementation. Today, limited access to the airspace is the principal barrier to the realization of the full economic potential that can be derived from UAS capabilities (Francis 2016).

To support the reduction of barriers that prevent unmanned aircraft from flying without the required waivers from the Federal Aviation Administration (FAA), the National Aeronautics and Space Administration (NASA) has investigated and integrated technologies, under the UAS Integration in the National Airspace System (NAS) Project (hereby known as UAS-NAS), which has been formulated to address the need for routine access to the global airspace for all classes of UAS (FAA 2013a). Moreover, a series of human in the loop simulations and flight test activities that integrate key concepts, technologies and/or procedures in a relevant air traffic environment has been conducted (Murphy *et al.* 2016b)(Murphy & Otto 2017)(NASA 2016). Human-in-the-loop real-time simulations have also been performed within the European project ERAINT, which is the acronym of Evaluation of the Remotely Piloted Air System (RPAS) - Air Traffic Management (ATM) Interaction in Non-Segregated Airspace (SESAR 2015). The work done within the above mentioned project is described in (Pastor *et al.* 2014).

Significant challenges must still be addressed in order to enable UAS to reach their full potential, allowing a safe integration of UAS operations. This is one of the key objectives of the European and American programs Single European Sky ATM Research (SESAR) (SESAR 2012a) and Next Generation Air Transportation System (NextGen) (FAA 2013b). Safety is the overriding principle in performing this integration. In the near to mid-term, research will need to focus on technology and systems deemed necessary to integrate UAS operations (FAA 2013a), satisfying both the user's requirements and flight regulations.

## **1.2. Key enabling technologies for UAS**

The integration of UAS will depend in large part on the ability to safely and effectively operate in varied environments and with varied tasking (Wheeler 2016). Current autonomous systems typically require external sensing or computation, such as a motion

capture system, Global Navigation Satellite System (GNSS) localization, prior map of the environment, or at least off-board sensor fusion and decision making. Other systems are affected by important limitations, due to highly structured environment, such as vertical walls, flat floors, and stationary scenes, and Size, Weight, and Power (SWaP) constraints (Wheeler 2016). Two key enabling technologies for safe UAS operations have been identified in this thesis:

- Technologies for autonomous navigation;
- Technologies for mission management.

### **1.2.1. Technologies for autonomous navigation**

A noted obstacle in reaching the navigation robustness necessary for the integration of UAS operations is the heavy reliance on GNSS. Indeed, GNSS loss, even for a brief period, often results in catastrophic failure. As a result, GNSS-degraded navigation has become a strong emphasis of research over the last decade (Vetrella *et al.* 2015b, 2016; Wheeler 2016).

Navigation performance and fault tolerance can be improved using inertial sensors for augmentation, combining measurement of both sensors typically through an extended Kalman Filter. In such integration, the GNSS derived positions and velocities update the inertial sensors, while the Inertial Navigation System (INS) is used for providing the high-rate navigation information available also during GNSS signal outages (Groves 2013). Therefore, a robust output is requested for inertial sensors in case of temporary non-nominal operation of measurement systems in the Kalman Filter.

Traditional gyroscopes, such as gimballed gyros, optic gyros and dynamically tuned gyros provide high-precision information for navigation and control systems, but they can be either too expensive or bulky, especially for small UAS applications. In recent years, the improvement of advanced micro-fabrication techniques has allowed the development of Micro Electro-Mechanical Systems (MEMS) inertial sensors (Barbour *et al.* 2011). Due to their characteristics of low-cost, light-weight, low power consumption, MEMS inertial sensors are well suited for UAS applications. However, they suffer more than traditional inertial sensors for environment dependent errors (Bhatt *et al.* 2012).

### **1.2.2. Technologies for mission management**

In recent years, the commercial applications of small UAS are growing rapidly (FAA 2018). The predicted volume of small UAS operations across both controlled and uncontrolled airspace could be on a scale comparable to that of present-day manned air traffic. The combined hobbyist and commercial fleet is projected to reach 3 to 6 million by 2021, up from less than 1.5 million in 2016 (FAA 2018). Consequently, mission management solutions are needed to ensure safe and efficient UAS operations.

It is envisioned that small UAS operations will be managed by a parallel air traffic system that would provide airspace services to participating UAS (Airbus 2018; Kopardekar *et al.* 2016). That system has been called Unmanned Traffic Management, or UTM. According to (Airbus 2018), it is “not a single, central system that mandates one way of operating for everything. Instead, it is a framework. It is a networked collection of services that join together and understand each other, based on common rules”. Several countries and trans-national bodies have already adopted this approach as the foundation for their own UTM implementations, described in (Airbus 2018). Each government has a slightly different view on how authority should be distributed.

The most significant benefit of UTM is that it would not rely on as many unproven technologies as concepts that require the UAS itself to equip fully for safe operations in the existing airspace (Mueller 2016). However, novel solutions are needed to support the UTM system in monitoring and coordinating the operations of a large number of small UAS (Wargo *et al.* 2014), handling the diversity in UAS and payload types and assessing a broad range of mission conditions.

### **1.3. Developed research solutions**

The aim of this thesis is to support the safe integration of UAS operations (FAA 2013a), taking into account both the user's requirements and flight regulations. To achieve this aim, two objectives have been defined:

- Improving navigation performance of UAS by exploiting low-cost inertial sensors;
- Proposing novel solutions to improve UAS mission management.

The developed research solutions, illustrated in Figure 1, make great impact to enable large-scale UAS operations, particularly in view of the increasing small UAS applications. These applications are affected by important limitations, due to SWaP constraints and their low-altitude operational environment, characterized by a variety of challenges to remote operations, such as people, personal property along UAS routes and other hazards.

The proposed solutions can be exploited for several enabling technologies, among them:

- A Mission Manager for UAS (Santamaria *et al.* 2009)(Royo *et al.* 2013) capable of identifying and assessing a broad range of mission-level conditions and then projecting an acceptable solution to execute successful outcomes throughout the mission timeline;
- Sense & Avoid (SAA) systems that replace the fundamental manned aircraft capability of “see and avoid”. SAA represents one of the main roadblocks to the integration of UAS operations by aviation authorities around the world (Melega *et al.* 2015)(Fasano *et al.* 2016b). SAA systems should detect not only air traffic, but also obstacles, terrain elevation and weather conditions;
- Improving UAS mission surveillance, which is a relevant technology to enable safe UAS application. For example, NASA has developed a prototype system that leverages the existing command and control link between the aircraft and ground control station, which includes periodic updates of the aircraft position, to provide the location of the aircraft to the national surveillance system, as well as provide the pilot with a display of aircraft in the vicinity of the unmanned aircraft (Murphy *et al.* 2016a);
- Flight termination systems, utilized as a last resort to bring down an UAS expeditiously in order to maintain some level of safety to the public or property (Santamaria *et al.* 2009)(Stansbury *et al.* 2009).

Moreover, the investigated technologies can be exploited for novel applications in other research fields, such as autonomous cars or autonomous ships.

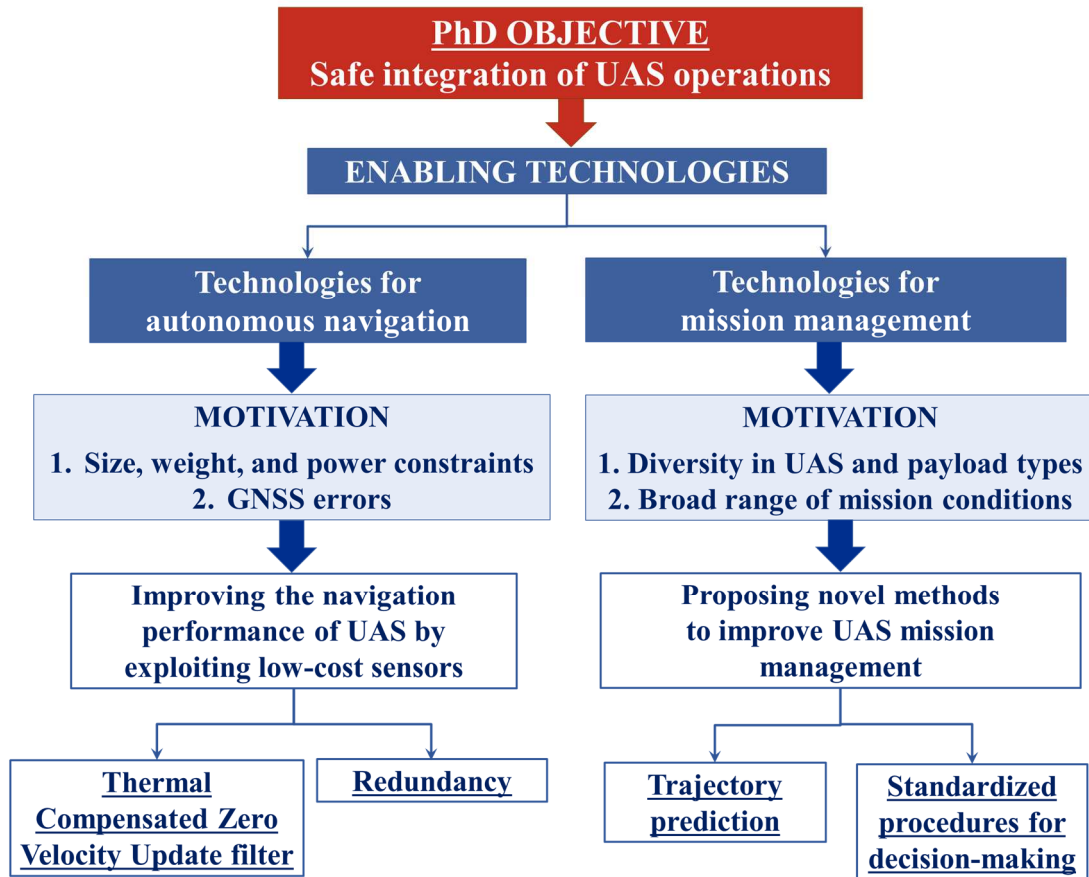


Figure 1. Flow-chart of the research carried out in this thesis.

### 1.3.1. Improving navigation performance of UAS by exploiting low-cost sensors

Gyro and IMU accuracy can be classified into performance grades according to bias stability specifications (as explained in Chapter 4), with the lowest grade being used for consumer products, and the highest performing grade being used for mission critical strategic applications (KVH 2014).

This thesis presents innovative solutions for improving the dead-reckoning performance of industrial and consumer grade MEMS inertial sensors (typically used for UAS navigation) for handling intermittent GNSS coverage in an integrated GNSS/MEMS-based inertial navigation solution (Gross *et al.* 2010b).

### **1.3.1.1. Industrial grade MEMS gyros**

These sensors have significant limitations in terms of sensitivity to environmental conditions. Their output average value, i.e., sensor bias, drifts with temperature, with a strongly non-linear trend (Niu *et al.* 2013). The traditional approach to estimate and correct gyro bias is a cascading of polynomial thermal calibration and Kalman filtering (Groves 2013). Consequently, it is time consuming and expensive. This aspect also reduces system accuracy, reliability, and maintainability.

This thesis proposes an innovative method, named Thermal Compensated Zero Velocity Update or TCZUPT filter, that unifies in a single algorithm the two steps of the traditional approach, saving time and economic resources and simplifying the management of thermal correction process. In this innovative approach, the calibration transfer function is exploited within the Kalman filter, with the aim of embedding the compensation of thermal effect on bias in the filter itself. Moreover, Back-Propagation Neural Networks (BPNNs) are exploited to obtain the calibration transfer function, since they guarantee better performance on mapping the highly non-linear bias trend with temperature than traditional polynomial fitting. The proposed algorithms have been tested on the Attitude and Heading Reference System (AHRS) Axitude AX1-[ ]™ developed by the Italian company GMA S.r.l.™.

### **1.3.1.2. Consumer grade MEMS gyros**

Last generation consumer grade MEMS inertial sensors have several distinctive features that make their use of interest also for professional navigation applications such as the ones related to attitude determination of advanced small UAS. Several advantages arise when using low-cost consumer grade MEMS gyros, such as reduced weight, compact configuration, low power consumption and easy integration with electronic boards (Barbour *et al.* 2011). Indeed, they are manufactured by using the same technology of micro-chips (Titterton & Weston 2004). Conversely, the overall error is more than an order of magnitude worse than industrial grade sensors, increasing the uncertainty in attitude determination.

A high-performance and low-cost calibration solution for consumer grade MEMS gyros is proposed in this thesis by exploiting redundancy. Indeed, redundancy guarantees a partial self-calibration of typical inertial sensors biases, reducing the uncertainty in attitude determination. To test the proposed redundant configuration, the world's densest sensor

board, SensorTile™, by STMicroelectronics™ has been adopted. In particular, a redundant IMU prototype, composed by a cubic configuration of SensorTiles™ has been developed.

### **1.3.2. Novel methods for UAS mission management**

#### ***1.3.2.1. UAS trajectory prediction***

As explained above, future scenarios envisage the use of small UAS within intense traffic systems, with their operations managed by the UTM system. Thus, a trajectory prediction tool is needed to support UTM in predicting small UAS separation and collision threats within a safe time-frame. Trajectory predictions can also be exploited by the on-board Sense & Avoid (SAA) system (Melega *et al.* 2014) and can support mutual tracking of UAS swarms by cooperative navigation systems (Leonard *et al.* 2012; Vetrella *et al.* 2015a). The tool must be able to predict trajectories for several UAS types, in different weather and wind conditions.

This thesis proposes a trajectory prediction tool for small UAS, based on the use of Artificial Neural Networks (ANNs). Being self-adaptive in constructing a mathematical model, ANNs can allow creating different models for the different UAS types, in several wind and weather conditions. ANNs can exploit flight data collected when the UAS executes a pre-assigned flight path to support trajectory prediction in standard traffic scenarios, by using an adaptive model learned during the network training. The algorithm has been tested on DJI Phantom 4™ flight data.

#### ***1.3.2.2. Standardized procedures for decision-making***

Due to the rapid growth in small UAS operations at low-altitude, the UTM system will have to manage numerous UAS operations in real-time. Furthermore, UAS/payload configurations must satisfy both the user's requirements and flight regulations. However, since the amount of available UAS platforms, payload configurations and requested missions is growing rapidly, misleading solutions can be derived without proper standard indications. This will also slow down the flight authorization process by the UTM system.

The thesis proposes a software tool that aims at supporting standardized procedures for decision-making process in order to identify UAS types, payload, and prescriptions that are adequate for any type of missions that can be authorized standing flight regulations. The

tool is designed to be scalable, thus adapting to the UAS mutable scenarios, characterized by the continuous development of new technologies and the evolution of regulations.

## 1.4. Summary of thesis chapters

This thesis is organized into six chapters, starting with the introduction. Figure 2 represents the overall configuration of the thesis.

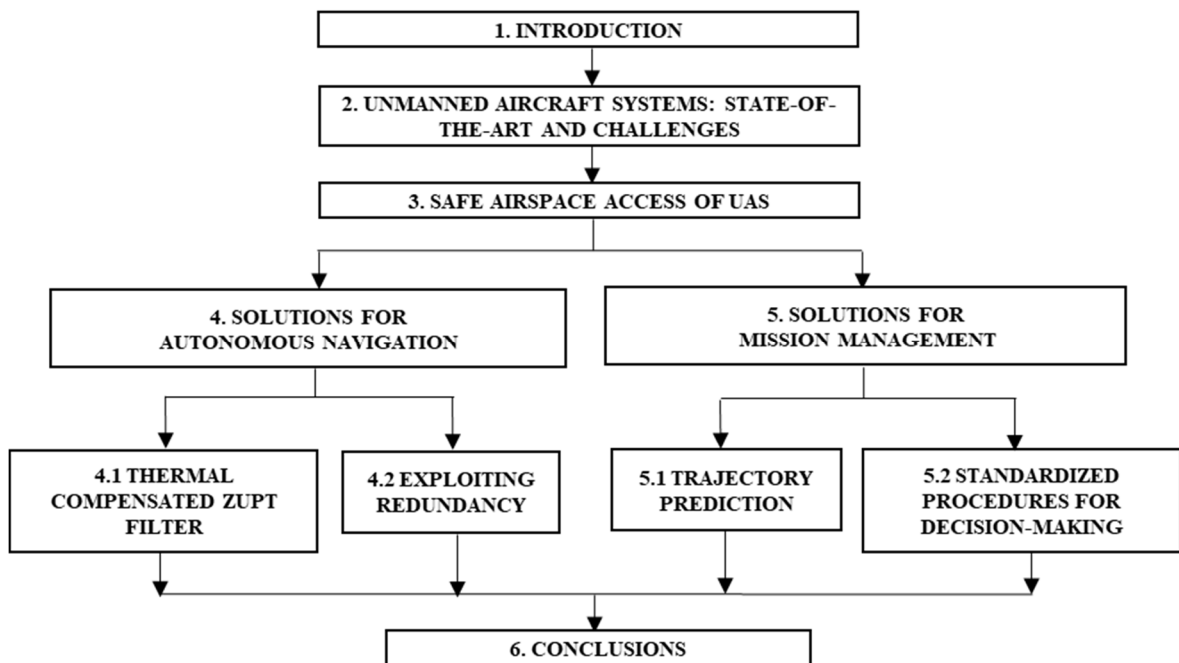


Figure 2. General organization of this thesis.

Chapter 2 describes the state of the art of UAS, in terms of classification and main applications. It also presents the research challenges and the expected future applications.

Chapter 3 investigates the current airspace integration approaches and points out the main technology limitations for safe UAS integration. It also presents an overview on the Unmanned Traffic Management system and its operational framework and identifies the enabling technologies for safe UAS integration.

The developed research solutions are extensively described in Chapter 4 and 5, which are organized according to the following structure: 1) Problem definition; 2) System Architecture; 3) Testing; 4) Results.

Finally, Chapter 6 presents the overall conclusions of this thesis.

# Chapter 2

---

## Unmanned Aircraft Systems: State-of-the-Art and Challenges

### 2.1. General context about Unmanned Aircraft Systems

Early unmanned aircraft were intended for military purposes, serving as aerial targets or actual weapons. However, they lacked the level of navigational precision necessary to reliably accomplish military objectives. The introduction of modern, compact, high-performance computer technology made UAS become attractive enough to its user community to earn a permanent place in the defence inventory (Francis 2016). Examples of UAS currently used for military purposes are: Northrop Grumman RQ-4 Global Hawk (Figure 3), Northrop Grumman MQ-4C Triton (Figure 4) and the General Atomics MQ-9 Reaper (sometimes called Predator B) (Figure 5). While Predator B is also known as a combat drone, since it can be used to deliver precision-guided munitions, the others are used for surveillance applications, loitering for long periods of time over suspected locations of possible targets.



Figure 3. Northrop Grumman RQ-4 Global Hawk.



Figure 4. Northrop Grumman's MQ-4C Triton.



Figure 5. Predator B developed by General Atomics.

The investments and the technological advances made by military organizations have generated a growing interest in their potential use for civil government, scientific research, and commercial applications (Degarmo 2004). The first highly visible civil applications of modern UAS were in the pursuit of scientific understanding. In the mid-to-late 1990s, NASA funded a number of then fledgling UAS developers to demonstrate very high altitude,

long-endurance civil UAS under its Environmental Research and Sensor Technology (ERAST) program. Aircraft such as Aurora Flight Sciences' Pegasus and AeroVironment's pioneering solar-powered HELIOS (Figure 6) were developed and flown as part of that effort. However, UAS application to non-military missions has risen dramatically in just the past few years. And, despite the success of several well-known military UAS models over the past two decades of conflicts, it is a new generation of platforms and technology that have captured the public's attention and interest (Francis 2016).



Figure 6. AeroVironment's pioneering solar-powered HELIOS.

The rapid increase in information technology over the last several decades, coupled with concomitant decreases in the size and cost of enabling electronics, would help usher in the era of affordable small-size UAS. Indeed, starting around 2010, there was a convergence of many technologies that made it feasible to design and produce small and very small UAS that could be sold in quantity at prices that were easily affordable by hobbyists or potential commercial users (Francis 2016). Multirotor, electric motor UAS, controlled by using economic remote control consoles or even by an App on a smartphone or tablet computer, became available on the consumer market. One of the most common multirotor UAS (DJI Phantom 4™), with the remote controller is shown in Figure 7. The availability of these inexpensive, highly manoeuvrable, easy-to-fly platforms, capable of carrying high-definition video cameras, and other sorts of sensors has resulted in an explosion of actual and proposed commercial applications (Gleason & Fahlstrom 2016).



Figure 7. Example of a multirotor UAS (DJI Phantom 4™), with the remote controller.

UAS are now being produced and deployed in many countries. The vast majority are small and very small UAS. An aerospace consulting firm predicted that UAS would be “the most dynamic growth sector of the world aerospace industry” (Thompson 2015). Figure 8 displays the projected global UAS market in 2020, by area of application. “Commercial” and “Hobby” applications, put together, will reach the same market size, in billion of U.S. dollars, of the military UAS. Figure 9 illustrates the projected commercial UAS revenue worldwide from 2015 to 2025, which is expected to increase with an exponential rate. Finally, Figure 10 shows the main civilian UAS applications.

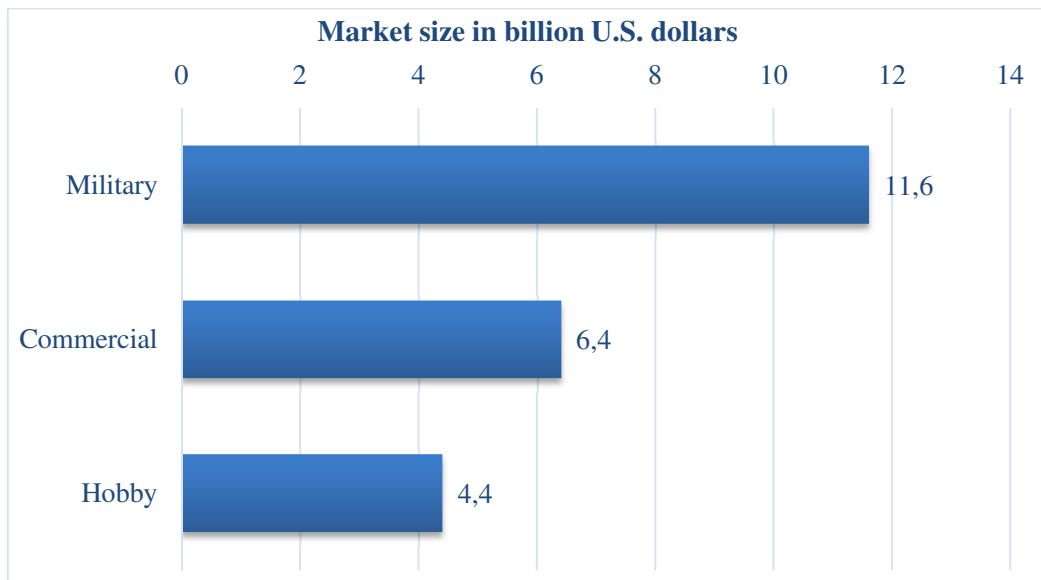


Figure 8. Projected global UAS market in 2020, by area of application, in billion U.S. dollars (Fortune; Frost & Sullivan ID 431717).

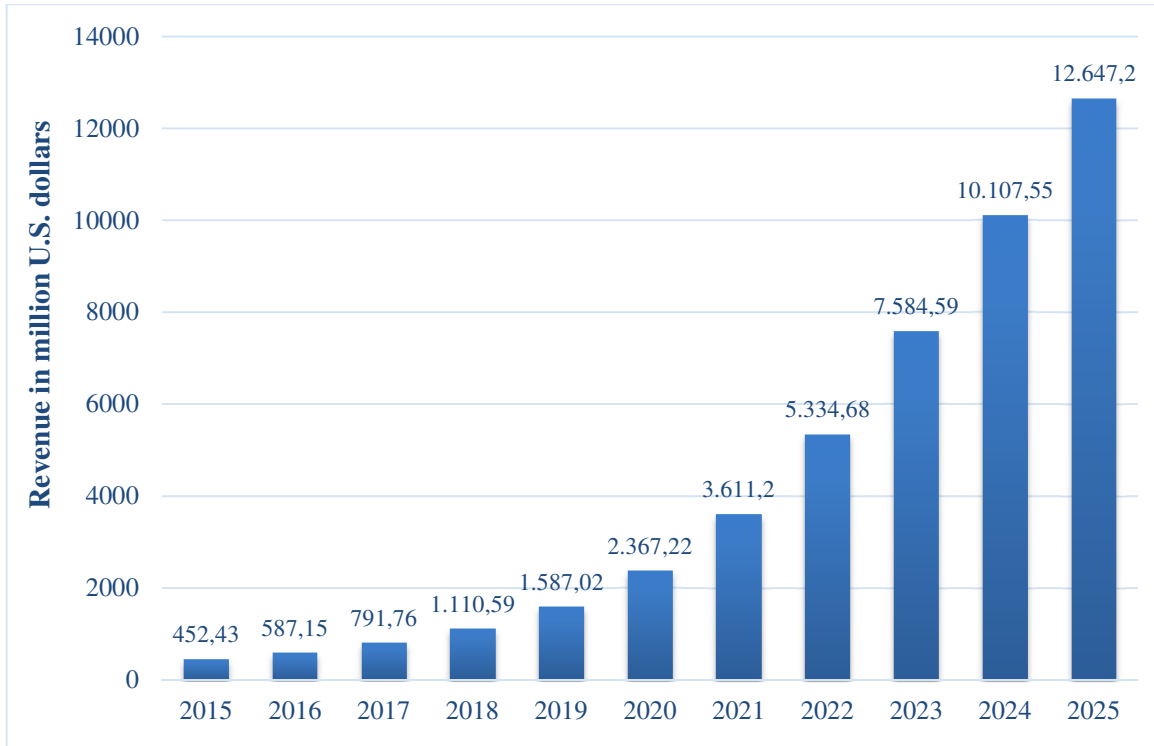


Figure 9. Projected commercial UAS revenue worldwide from 2015 to 2025, in million U.S. dollars (Tractica ID 607922).

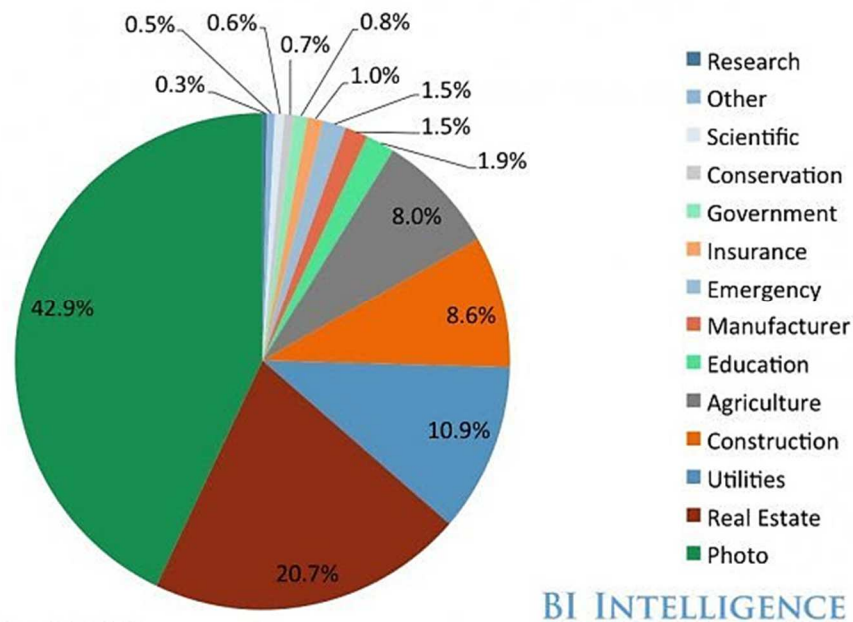


Figure 10. Top industries using UAS (BI Intelligence).

## 2.2. Classification

UAS can be categorized in a variety of ways based on vehicle attributes including the type of aircraft (fixed wing or rotorcraft), weight, operating altitude, and range. The categorization system is an important step in UAS operations management and permits a proportional regulatory regime across the entire spectrum of UAS (Ministry of Defence & Military Aviation Authority 2016).

The North Atlantic Treaty Organization (NATO) classification, which is based on Maximum Takeoff Weight (MTOW) and normal operating altitude, is generally used as the baseline for categorization. The NATO UAS Classification is shown in Figure 11 (Joint Air Power Competence Centre 2010). Categories start with weight classes. These weight classes are further divided on the basis of the operational altitude of the UAS. However, MTOW and altitude should not be considered the sole determinants of the final categorization of an UAS but also the aggravating and mitigating factors of its operation should be taken into account. Some of them are presented in Table 1 (Ministry of Defence & Military Aviation Authority 2016).

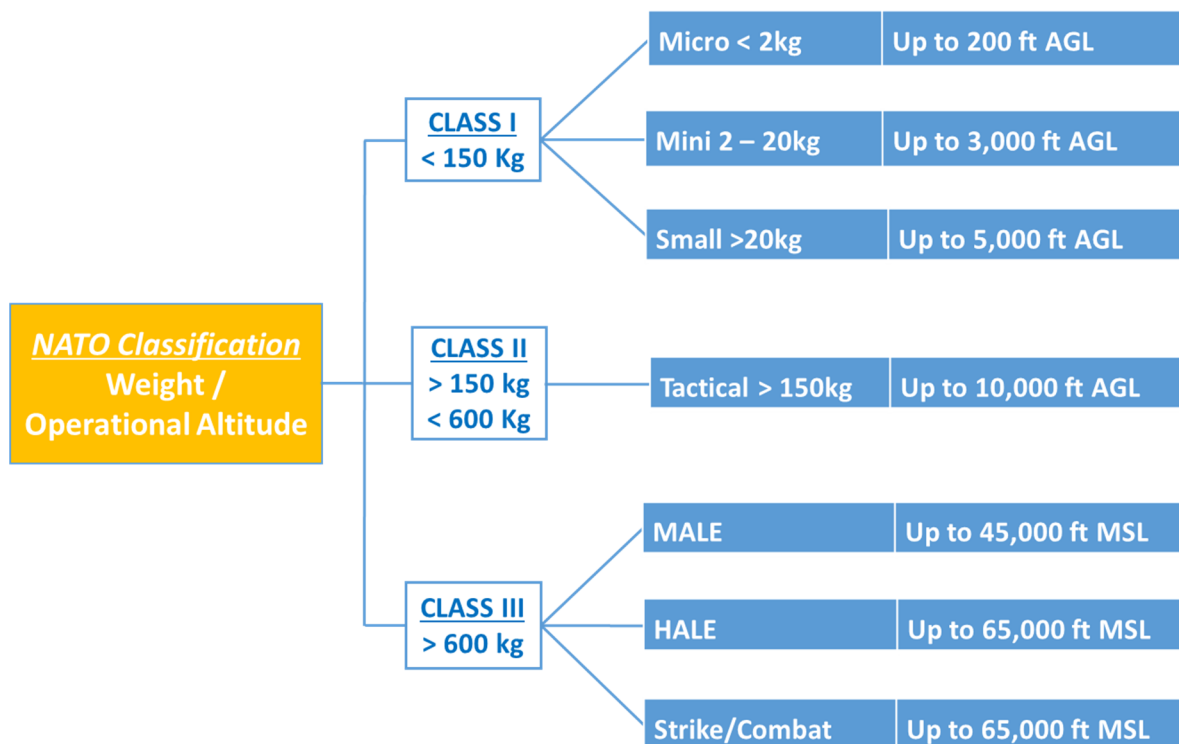


Figure 11. NATO UAS Classification.

Table 1. Aggravating and mitigating factors (Ministry of Defence & Military Aviation Authority 2016).

<b>Mitigating Factors</b>	<b>Aggravating Factors</b>
Operation in Visual Line of Sight (VLOS)	Extended range operation Beyond VLOS (BVLOS)
Operation in segregated airspace	Operation in non-segregated airspace
Overflight of low population density	Overflight of congested areas/high population density
Flight termination system	Weaponization
Redundancy	Failure mode – high Kinetic Energy
Frangibility of UAS structure	Complexity

Furthermore, in order to harmonize the implementation of small UAS regulation across the European Union (EU), the European Aviation Safety Agency (EASA) has proposed its regulatory framework, known as EASA Opinion 01/18 (European Aviation Safety Agency 2018), to the EU Commission. Indeed, small UAS are increasingly being used in the EU, but under a fragmented regulatory framework.

Key to the EASA operation centric, proportionate, risk- and performance-based regulatory framework is the breaking down of UAS flights into three categories, i.e. open, specific, and certified, with different safety requirements, proportionate to the risk (European Aviation Safety Agency 2015a, 2015b):

- ‘Open’ category is a category of UAS operation that, considering the risks involved, does not require a prior authorization by the competent authority nor a declaration by the UAS operator before the operation takes place;
- ‘Specific’ category is a category of UAS operation that, considering the risks involved, requires an authorization by the competent authority before the operation takes place, except for certain standard scenarios where a declaration by the operator is sufficient or when the operator holds a light UAS operator certificate (LUC) with the appropriate privileges;
- ‘Certified’ category is a category of UA operation that, considering the risks involved, requires the certification of the UAS, a licensed remote pilot and an

operator approved by the competent authority, in order to ensure an appropriate level of safety.

The objective of the Opinion is to create a new regulatory framework that defines measures to mitigate the risk of operations in the:

- ‘Open’ category, through a combination of limitations, operational rules, requirements for the competency of the remote pilot, as well as technical requirements for UAS;
- ‘Specific’ category, through a system that includes a risk assessment being conducted by the UAS operator before starting an operation, or an operator complying with a standard scenario, or an operator holding a certificate with privileges.

Of great concern to UAS operators is the EU requirement for UAS which are “able to transfer ‘80 J’ of terminal kinetic energy in an impact with a person” to be registered, other criteria notwithstanding. This is further defined as meaning the terminal velocity of the drone when falling from a height of 396ft (120m).

## **2.3. Missions**

Defining the missions for UAS is a non-trivial task because of their large diversity. There have been repeated efforts to come up with comprehensive lists of UAS missions, but all such lists tend to become out of date as new mission concepts continually arise (Fahlstrom & Gleason 2012). Two major divisions of missions for UAS are *civilian* and *military*, but there is significant overlap between these two in the area of reconnaissance and surveillance. These missions, often combined, are defined as follows (Gleason & Fahlstrom 2016):

- Reconnaissance: The activity to obtain by visual or other detection methods information about what is present or happening at some point or in some area;
- Surveillance: The systematic observation of aerospace, surface or subsurface areas, places, persons or things by visual, aural, electronic, photographic, or other means.

The development of UAS has been led by the military and there are other areas along recognized as potential military missions that also have civilian equivalents. These include atmospheric sampling for radiation and/or chemical agents, providing relays for line-of-sight communications system, and meteorological measurements. An area of interest to both the military and civilian sectors is to provide a high-altitude platform capable of lingering indefinitely over some point on the Earth. This platform can perform many of the functions of a satellite at lower cost and with the capability of landing for maintenance or upgrade and of being redeployed to serve a different part of the world (Gleason & Fahlstrom 2016). UAS can be also used to perform flight inspection, which is the task of validating the radio signal emitted by ground navigation aids (Barrado *et al.* 2013).

Recently, public interest in social media coupled with the development of low-cost systems have put them in high demand for commercial and recreational uses. In a recent publication addressing the civil and commercial marketplace, the Association of Unmanned Vehicle Systems International (AUVSI) highlighted several applications (Francis 2016):

- Package delivery;
- Taking overhead picture of real estate for sale;
- Inspections of inaccessible roofs (or bridges, towers, chimneys, power lines, steeples, trees, etc.) using a high-definition video camera that can be positioned a few feet from the area to be inspected and can adjust its point of view;
- Surveying/inspecting fields of crops;
- Spraying crops with pesticides;
- Observing scenes of accidents, flooding, landslides, or other incidents;
- Providing video feeds for “breaking news” reports;
- Performing precision three-dimensional surveys using stereoscopic cameras and precision locating of the platform at low altitude over the area to be surveyed;
- Delivery of supplies to remote areas;
- Search for people missing in rough terrain;
- Monitoring forest areas for wildfires;
- Sensing of pollutants near their source;
- Providing flexible and dynamic camera positioning for cinema and television video production;

- Law enforcement;
- Weather monitoring.

This array of applications has also been animated by the proliferation of very low cost, miniature commercial imaging sensors that have flooded the cell phone and tablet computer markets. The integration of sensors with other payload elements affords an opportunity for further expansion of missions and applications. As an example, the combination of multispectral imaging with real-time nutrient/pesticide dispensing can potentially take “precision agriculture” to another level. Similarly, real-time infrared imaging with concurrent fire suppressant application could greatly improve the ability to mitigate incipient wildfires. Although the remote sensing capability adds great value by itself, the ability to integrate it with a timely response/action mechanism greatly increases the utility of the resultant system (Francis 2016).

## **2.4. Research trends**

### **2.4.1. Research challenges**

The levels of innovation and discovery that have led to recent growth in UAS capabilities are expected to continue. Several research challenges have been identified in (FAA 2013a; Francis 2016; Ishihara *et al.* 2016).

#### **A. Increasingly Autonomous Capability.**

The recent advance of modern computing power is opening the door to even higher levels of autonomous operation, where the human element is fully relieved of many minor decisions and becomes essentially supervisory in nature. However, much remains to be done in this domain. For example, many systems today limit UAS operations to one vehicle by one operator. Studies have been conducted to illustrate the possibility of managing multiple aircraft with a single human operator, if the level of supervisory interaction is high enough (Ruff *et al.* 2002). However, for the latter to occur, the level of autonomy must increase dramatically.

## B. Cooperative Navigation.

Cooperative Navigation can be exploited to improve the absolute navigation performance of formation flying UAS. This has been done in (Vetrella *et al.* 2016), where the authors presented the concept of improving the absolute navigation performance of a UAS (chief) by exploiting a formation of cooperative flying vehicles (one/more deputies). Specifically, the proposed navigation architecture combines differential GNSS and relative sensing by vision within an original sensor fusion scheme based on an Extended Kalman Filter (EKF).

## C. Sense and Avoid.

One of the key requirements for enabling UAS operations is how to provide the UAS with a Sense and Avoid (SAA) capability, to replace the fundamental manned aircraft capability of “see and avoid”. SAA represents one of the main roadblocks to the integration of UAS operations by aviation authorities around the world. There will be fundamental differences between SAA for large UAS (operating in controlled airspace) and small UAS (operating at low altitudes in minimally or uncontrolled airspace). Large UAS will be required to deal with manned aircraft operating in the same airspace, as the main obstacle to avoid. Instead, though the UAS operations will vary widely by mission, many of them will require operating more closely to people and obstacles (for photography, inspections, etc.) than current aviation separation standards permit (Fasano *et al.* 2016b).

## D. Flight Termination System.

It is an emergency component. In case of contingencies that interrupt the UAS flight, the Flight Termination System guarantees that the potential impact to the ground of the UAS will not fatally damage any person or infrastructure (Santamaria *et al.* 2009).

## E. Small Size/Scale.

Small UAS have proliferated in military missions for over a decade and performed admirably in a variety of tactical roles. Recently, they have enabled for a variety of civil and commercial applications ranging from highway/bridge infrastructure inspection to precision agriculture. Even though smaller variants, so-called “micro air vehicles” have begun to appear in real operational roles, the further reduction of dimensions is another relevant

research trend. This reduction allows UAS operations in highly confined airspace. However, to reach this aim, it is necessary a further miniaturization of the on-board systems, e.g. navigation systems, payload, etc.

#### F. Extreme Endurance.

UAS capability to stay aloft for periods that well exceed normal crew limitations has been demonstrated to a large extent in current operational systems. 24-h endurance capabilities are commonplace for larger platforms and are rapidly becoming possible also for small UAS. However, designers are currently focused on week-long operation, with some experimental systems attempting even longer durations, to allow future missions, such as aerial cell-phone relay and Internet distribution platforms. Several research efforts have been made to tackle it. For example, the design and development of a hybrid fuel cell/battery propulsion system for a long endurance small UAS is described in (Savvaris *et al.* 2016).

#### G. Novel Shapes and Configurations.

The lack of need for a conventional cockpit can result in novel shapes and configurations more suitable to niche missions and unique flight environments. Designers have already provided numerous examples of unconventional configurations ill-suited to manned flight. For example, the design and system integration of a novel coaxial, flap actuated, spherical UAS for operations in complex environments, such as buildings, caves or tunnels is presented in (Malandrakis *et al.* 2016). The spherical design protects the inner components of the vehicle and allows the UAS to roll along the floor if the environment permits.

#### H. Unconventional Launch and Recovery.

Novel approaches for launching and recovering are increasing significantly, especially for smaller UAS. For example, assisted rail launch capability and net or tether recovery techniques are largely employed. Larger UAS may find similar opportunities as in the shipboard concept where a high performance, Unmanned Combat Aerial Vehicle (UCAV) is tube-launched like a cruise missile and later recovered shipside. Future novel launch and recovery techniques may well enable UAS operations in otherwise impractical civil and commercial environments as well.

### I. Extreme Manoeuvring Capability.

UAS are, in principal, capable of sustaining accelerations and forces limited only by structural considerations, operating well beyond the tolerance of any human pilot. However, the introduction of other new technologies, such as structural morphing capabilities is being investigated to increase manoeuvre accelerations in future unmanned combat aircraft.

## 2.4.2. Future UAS applications

As explained above, new capabilities that improve operational versatility seem to emerge on a regular basis. Consequently, there are major commercial development programs underway to implement at least the following missions (Francis 2016):

- Search and rescue using a UAS that is capable of landing and carrying a person found (not a pilot) back to its base;
- Long-endurance, high-altitude platforms for communication relays, serving as local area satellites for telephone or digital broadband services;
- Applications in highly confined spaces, such as pipe interiors. Indeed, the reduction of dimensions is another relevant research trend. Currently, the smallest UAS variations, such as the Aerovironment Hummingbird (Figure 12) are still in the experimental stage. Its linear dimensions do not exceed 15 cm in any axis. With further miniaturization, they may even prove useful in internal bio-medical applications, exploring the internal of the human anatomy.
- Self-piloted personal aircraft and on-demand air taxi service. However, this application is subject to public perceptions about the safety of small aircraft and autonomous flight operations.
- Micro UAS Swarms. Micro UAS exhibit limitations due to their size. Their payload is usually only a few hundred grams allowing just light and compact sensors. Furthermore, they have a rather short endurance. Most of these limitations can be eased by employing teams or swarms of cooperating UAS (Leonard *et al.* 2012, 2014). Some complex monitoring and surveillance missions (Skinner *et al.* 2018) and remote sensing applications (Albani *et al.* 2017) can be implemented with groups of flying platforms. However, the use of multiple platforms simultaneously still needs investigation. For example, a visual-based approach that allows an UAS to detect and track a cooperative

flying vehicle autonomously using a monocular camera is presented in (Opromolla *et al.* 2018).



Figure 12. AeroVironment Hummingbird.

# Chapter 3

---

## Safe Airspace Access of UAS

### 3.1. Introduction

Despite the potential of UAS across a range of economically beneficial and compelling applications, there are significant obstacles to their successful introduction and implementation. These include the lack of acceptable infrastructure to coordinate several different UAS operations, technical issues, institutional conservatism combined with legal issues, along with the concomitant consequences of negative public perceptions. The current operational approval process imposes limitations on UAS operations to ensure airspace safety while those issues are addressed (Francis 2016).

The integration of UAS in the NAS was investigated in the past through the Access 5 project run by NASA in collaboration with industry, FAA, and the United States Department of Defence, in order to introduce HALE remotely operated aircraft. Access 5 started in May 2004 and was slated to run for five years. However, the project was terminated on February 28, 2006 after a reorganization of NASA's research program and (NASA 2006).

Today, limited access to the airspace is still the principal barrier to the realization of the full economic potential that can be derived from UAS capabilities (Francis 2016). A

reference statement for integrated unmanned aircraft operations is that UAS shall not increase the current level of risk for other aircraft or compromise safety to people or property on the ground (Elias 2012). Therefore, significant challenges, technical and otherwise, must be addressed in a manner that will enable UAS of all types to reach their full potential. A safe integration of UAS operations is one of the key challenges of the European and American programs Single European Sky ATM Research (SESAR) (SESAR 2012a) and Next Generation Air Transportation System (NextGen) (FAA 2013b).

### **3.2. Airspace integration approaches**

Several approaches have been proposed to support the access of UAS to the airspace (Lacher *et al.* 2010; Mueller 2016). The most conservative approach consists in requiring UAS to meet all existing traditional aviation regulations, either through direct compliance or through alternative means if direct compliance is difficult. This approach has multiple benefits: UAS will operate in the airspace in a way that is indistinguishable from existing users. However, the drawbacks are significant too. The requirements for alternative means of compliance with all regulations are difficult to determine. Furthermore, complying with all existing regulations will likely be possible only by very large UAS capable of equipping with heavy, expensive and power-intensive sensors and processors (Mueller 2016).

The disadvantages mentioned above may be avoided by building a parallel air traffic system that would provide airspace services to participating UAS. Many of the challenges in terms of separation assurance, contingency management, surveillance to traffic flow management and privacy concerns would be addressed by shifting responsibility from on-board systems to a centralized command and control system. This traffic management system could allow many more UAS to operate in a wider variety of ways than would the first approach that required significant equipment on-board each aircraft (Mueller 2016).

The separate traffic management system would differentiate the requirements for operating in airspace environments with different risk-based classifications. While at high altitude the specific characteristics of the overflown property are not important, small UAS operating at low-altitude will impact that property by supporting desired missions. Consequently, the low-altitude airspace will be classified in operating environments or zones, which would be defined by four risk-based criteria: population density, density of man-made structures, likelihood of encountering manned aircraft, and the number of

planned UAS operations. It is worth noting that these classes relate only to the services provided by the UTM system in existing Class G airspace (Atkins & Di Donato 2016).

Another concept is the temporal and geographic airspace segregation. The low-altitude airspace could be set aside for UAS operations. Existing users of that airspace, such as helicopters, hang gliders, and powered parachutes, would either be forbidden from operating in the designated airspace or would have to comply with additional requirements to enter it. Segregation of airspace could simplify requirements for UAS to operate in those set-aside areas because the mix of users would be more homogeneous.

However, the concept of airspace segregation has not received significant research attention for several reasons. One of the most relevant is that the aviation authorities, such as FAA, prefer to move from the current paradigm in which the air traffic system “accommodate” UAS to one in which UAS are “integrated” (FAA 2013a). Indeed, enabling a segregated airspace of this magnitude would be more akin to designing an entirely new type of airspace, which would entail a set of requirements potentially more complex than those required to integrate with existing airspace users. Moreover, a segregated airspace design would likely not be suitable for most proposed UAS operations (Mueller 2016).

In conclusion, UAS have been proposed for use in a wide variety of areas, but the regulatory framework will be a major factor in determining whether the technological, economic and public policy hurdles will be low enough that UAS will be preferred over existing alternatives. The current adopted approach is that unmanned aircraft will share airspace with manned counterparts, configuring the airspace so that they can coexist. It is worth noting that access to airspace must be dependent on equipage and performance, not mission (Airbus 2018).

### **3.3. Unmanned Traffic Management system**

#### **3.3.1. Introduction**

Due to the number and variety of UAS operations envisioned, it is clear that the existing ATM system cannot cost-effectively scale to deliver services for all participating UAS. Furthermore, the nature of most of these operations does not require direct interaction with the ATM system. Therefore, it is globally acknowledged the need to develop a parallel air traffic management system that is separate from, but collaborative with the ATM system

(FAA 2018). That system is named Unmanned Traffic Management, or UTM (Airbus 2018).

In a scenario of rapid growing small UAS applications, the UTM system is envisioned to enable safe and efficient operations, by providing services such as airspace design, corridors, dynamic geofencing, severe weather and wind avoidance, congestion management, terrain avoidance, route planning and re-routing, separation management, sequencing and spacing, and contingency management (Ren *et al.* 2017). The most significant benefit of the UTM system is that it would not rely on as many technologies as concepts that require the UAS itself to equip fully for safe operation in the existing airspace.

Standing on current guidelines, UTM will adopt the principle of distributed authority rather than relying on centralized control (Kopardekar *et al.* 2016). This opens up the system to more service providers. Decentralization privatizes the cost of serving and adapting to market needs, while government regulators remain key for ensuring that safety, access, and equity are maintained (Airbus 2018).

Several countries and trans-national bodies have already adopted this overall approach as the foundation for their own UTM implementations (Airbus 2018):

- In the United States, FAA, NASA, other federal partner agencies and industry are collaboratively developing the UAS Traffic Management system, which is a traffic management ecosystem for UAS operations that is separate but complementary to the FAA's Air Traffic Management (ATM) system (FAA 2015). A detailed description on how the UTM would work, is detailed in (Prevot *et al.* 2016);
- In Europe, gathering experts from aviation, research and academia, the Concept of Operation for European UTM Systems (CORUS) consortium is developing a concept of operations for U-Space, the European system for management of UAS;
- The Civil Aviation Administration of China (CAAC) is defining the use of a civil UAS Operation Management System (UOMS) (CAAC 2018);
- The Japanese UTM system is being built by the Japan UTM Consortium (JUTM) (METI 2017) and a national UTM project founded by New Energy and Industrial Technology Development (NEDO).

### 3.3.2. Operational framework

The UTM operational framework, shown in Figure 13, ensures the safe conduct of UAS operations through the issuance of performance authorizations that ensure operational and performance requirements are met, the sharing of flight intent and airspace constraint information among operators, and the use of services, technologies, and equipage to de-conflict operations (FAA 2018).

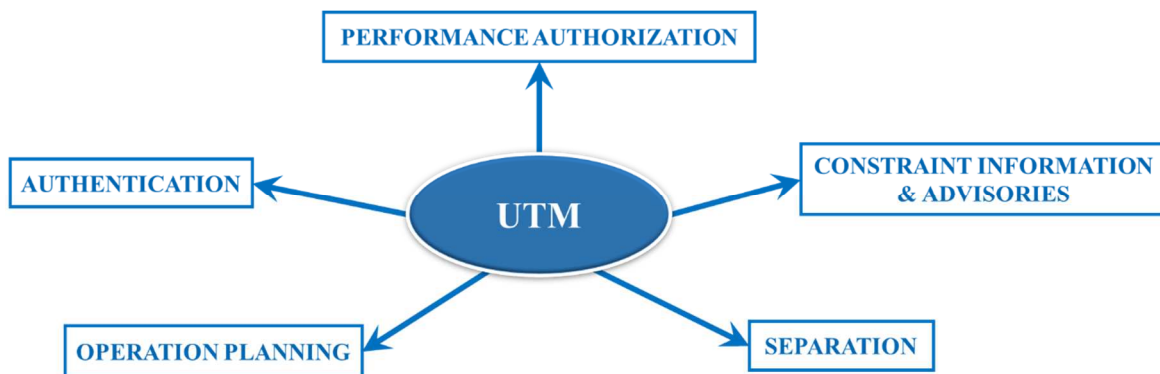


Figure 13. UTM operational framework.

#### A. Performance authorization

All BVLOS operators are required to obtain a performance authorization from the FAA prior to conducting a UTM operation. The FAA grants a performance authorization when a UAS operator’s proposed ground and air assets are sufficient to meet an established level of performance in the airspace in which they intend to operate (FAA 2018).

#### B. Authentication

Operators are required to certify, register, and obtain all appropriate authorizations and to demonstrate compliance with performance and capability requirements per regulatory policy prior to performing UTM operations. UTM expects an operator’s registration is valid and may audit should conditions warrant (FAA 2018).

#### C. Operation planning

Flight intent is submitted and shared among operators for situation awareness in the form of an operation plan, which is the equivalent of the flight plan for manned aircraft operations managed by ATM. The operation plan is developed prior to the operation and

should indicate the volume of airspace within which the operation is expected to occur, the times and locations of the key events associated with the operation, including launch, recovery, and any other information deemed important (e.g., segmentation of the operation trajectory by time) (FAA 2018).

#### D. Constraint information & advisories

Central to UTM is a shared situational awareness based on knowledge of all available constraint and advisory information in the UTM network. Advisories, weather information, other UTM participant observations, and a variety of other information may be made available through the UTM network and should be considered into the operator's planning and execution to ensure safe conduct of UTM operations. Furthermore, UAS operators within UTM are responsible for identifying unexpected operational conditions or flight hazards that may affect their operations (FAA 2018).

#### E. Separation

Although UTM provides traffic management services, operators are ultimately responsible for maintaining separation from other aircraft, airspace, weather, terrain, and hazards, and avoiding unsafe conditions throughout their operations. The operator is responsible for remaining within the bounds of the assigned flight volume and tracking the aircraft location during all phases of flight with performance criteria appropriate for the operation performed. The operator also monitors for vehicle non-conformance or on-board equipment failures or degradation (e.g., lost link, engine failure). These monitoring functions can be incorporated into the UAS (vehicle and ground control equipment) such that the operator is alerted quickly and can take necessary corrective action. For situations where corrections cannot be made, operators are responsible for notifying affected airspace users (FAA 2018).

### **3.3.3. Enabling technologies**

Considering the UTM operational framework, novel solutions should be investigated to:

- Allow the requesting UAS operators to meet established performance levels in the airspace in which they intend to operate, in order to obtain the performance authorization by the authorization entity;
- Assess a broad range of mission-level conditions, identifying a suitable UAS/payload configuration, by considering the mission requirements, flight regulations and operational environment. This simplifies the authentication process, helping operators to demonstrate compliance with performance and capability requirements;
- Assess UAS operation plan feasibility. Operators are expected to submit operation plans in four-dimensions, as a sequence of 4D waypoints (three spatial, one temporal) (SESAR 2012b). This is a topic investigated by many researchers (Amaro Carmona *et al.* 2015; Gardi *et al.* 2015; Mutuel *et al.* 2013). Given weather prediction, vehicle performance data, and 4D waypoint data, it is necessary to assess operation plan feasibility in a timely manner, by determining if at each waypoint arrival time a simulated trajectory is within a prescribed distance from the waypoint (Ishihara *et al.* 2016);
- Allow to perform rigorous safety analyses of UAS operations in low-altitude airspace (Tyagi *et al.* 2017), aiding operators to identify unexpected operational conditions or flight hazards that may affect their operations. This will improve the shared situational awareness in the UTM system;
- Aid UAS operators to maintain separation from other aircraft, airspace, weather, terrain, and hazards, and avoiding unsafe conditions throughout their operations.

### **3.4. Technology limitations for safe integration of UAS**

While UAS hold much promise, allowing routine and safe access of UAS to civil airspace involves several issues that touch on nearly every aspect of the aviation technical, operational, and legal system. Presented in (Degarmo 2004) is a framing of those issues organized into five major groupings: safety, security, air traffic, regulatory, and socio-economic.

This research focuses on technical and operational issues, considered among the principal inhibitors to the integration and wide-spread acceptance of UAS (Degarmo 2004). Chief among these are:

- GNSS errors, i.e. sources of uncertainty and intentional hacking and signal jamming;
- Need of collision avoidance, for air traffic and people and property on the ground;
- Need of standards addressing UAS systems and operations.

### **3.4.1. GNSS errors**

A noted obstacle in reaching the navigation robustness necessary for the integration of UAS operations is the heavy reliance on GNSS (Wheeler 2016). A robust navigation solution cannot only depend on GNSS measurements due to varied sources of uncertainty (NovAtel 2018; Ochieng *et al.* 2003), extensively described in Section 3.4.1.1. Further, GNSS measurements may be unavailable when shadowed by buildings or foliage, and simply cannot be applied indoor. The most difficult situations will likely involve operations in urban canyons, where GNSS measurements are intermittent or unavailable (Francis 2016). Additionally, GNSS signals could potentially be intentionally jammed or hacked resulting in a loss or hostile takeover of control (Elias 2012).

#### ***3.4.1.1. Sources of uncertainty***

##### **A. Satellite clock errors.**

Although GNSS satellites use the most precise atomic clocks featuring nanosecond accuracy, the clock drift phenomena may cause minute inaccuracies, which can produce errors that affect positioning. The clock on the satellite is monitored by the GNSS ground control system and compared to the even more accurate clock used in the ground control system. In the downlink data, the satellite provides the user with an estimate of its clock offset.

To obtain a more accurate position, the GNSS receiver needs to compensate for the clock error. One way of compensating for clock error is to download precise satellite clock information from a Space Based Augmentation System (SBAS) or Precise Point Positioning (PPP) service provider. The precise satellite clock information contains

corrections for the clock errors that were calculated by the SBAS or PPP system. Another way of compensating for clock error is to use a Differential GNSS or Real Time Kinematic (RTK) receiver configuration.

#### B. Orbit errors.

GNSS satellites travel in very precise, well known orbits. However, like the satellite clock, the orbits do vary a small amount and a small variation in the orbit results in a significant error in the position calculated. The GNSS ground control system continually monitors the satellite orbit. When the satellite orbit changes, the ground control system sends a correction to the satellites and the satellite ephemeris is updated. However, even with the corrections from the GNSS ground control system, there are still small errors in the orbit that can result in up to  $\pm 2.5$  metres of position error.

One way of compensating for satellite orbit errors is to download precise ephemeris information from an SBAS system or PPP service provider. Another way of compensating for satellite orbit errors is to use a Differential GNSS or RTK receiver configuration.

#### C. Number of satellites.

Few visible satellites increases sensitivity to timing errors.

#### D. Dilution of precision (DOP).

DOP error may be caused by the relative positions in three-dimensional space of the satellites used to calculate a position. In other words, visible satellites are poorly spaced.

#### E. Ionospheric delay.

The ionosphere is the layer of atmosphere between 80 km and 600 km above the Earth. This layer contains electrically charged particles called ions. These ions delay the satellite signals and can cause a significant amount of satellite position error (Typically  $\pm 5$  metres, but can be more during periods of high ionospheric activity). Ionospheric delay varies with solar activity, time of year, season, time of day and location. This makes it very difficult to predict how much ionospheric delay is affecting the calculated position. It also varies based on the radio frequency of the signal passing through the ionosphere.

GNSS receivers that can receive more than one GNSS signal, L1 and L2 for example, can use this to their advantage. By comparing the measurements for L1 to the measurements for L2, the receiver can determine the amount of ionospheric delay and remove this error from the calculated position. For receivers that can only track a single GNSS frequency, ionospheric models are used to reduce ionospheric delay errors. Due to the varying nature of ionospheric delay, models are not as effective as using multiple frequencies at removing ionospheric delay. Ionospheric conditions are very similar within a local area, so the base station and rover receivers experience very similar delay. This allows Differential GNSS and RTK systems to compensate for ionospheric delay.

#### F. Tropospheric delay.

The troposphere is the layer of atmosphere closest to the surface of the Earth. Variations in tropospheric delay are caused by the changing humidity, temperature and atmospheric pressure in the troposphere. Since tropospheric conditions are very similar within a local area, the base station and rover receivers experience very similar tropospheric delay. This allows Differential GNSS and RTK systems to compensate for tropospheric delay. GNSS receivers can also use tropospheric models to estimate the amount of error caused by tropospheric delay.

#### G. Multipath.

Multipath interference can occur where the user equipment receives reflected signals from a given satellite in addition to the direct signals. For land applications, signals are generally reflected off the ground, buildings, or trees, while for aircraft and ships, reflections off the host-vehicle body are more common. Interference can also occur from diffracted signals. The reflected and diffracted signals are always delayed with respect to the direct signals and have a lower amplitude unless the direct signals are attenuated (e.g., by a building or foliage). Low-elevation-angle signals are usually subject to the greatest multipath interference.

The simplest way to reduce multipath errors is to place the GNSS antenna in a location that is away from the reflective surface. When this is not feasible, the GNSS receiver and antenna must deal with the multipath signals. Long delay multipath errors are typically handled by the GNSS receiver, while short delay multipath errors are handled by the GNSS

antenna. Due to the additional technology required to deal with multipath signals, high-end GNSS receivers and antennas tend to be better at rejecting multipath errors.

#### **3.4.1.2. *Intentional hacking and signal jamming***

In addition to safety risks, the operation of civilian unmanned aircraft raises potential security risks, including the possibility that terrorists could use a drone to carry out an attack against a ground target. It is also possible that UAS themselves could be targeted by terrorists or cybercriminals seeking to tap into sensor data transmissions or could potentially be intentionally jammed or hacked resulting in a loss or hostile takeover of control (Elias 2012).

A remote hijacking of an unmanned aircraft by GNSS guidance signals has been demonstrated in (Humphreys 2012). It warned that advances in software-defined radio and the availability of GNSS signal simulators may provide average hackers with the capability to interfere with unmanned aircraft operations and recommended that non-recreational civilian unmanned aircraft weighing more than 18 pounds be required to have spoof-resistant navigation systems. It concluded that the issue could be mitigated by using additional navigation systems that do not rely on GNSS, and/or by encrypting communications and telemetry signals.

### **3.4.2. Collision avoidance**

UAS operators do not have the capability to see the environment around the vehicle when flying Beyond Visual Line of Sight. Therefore, software architectures addressed to UAS should replace human perception and reaction, detecting not only air traffic, but also obstacles, terrain elevation and weather conditions (Melega *et al.* 2011)(Cuadrado *et al.* 2013).

#### **3.4.2.1. *Air traffic***

The risk of collision between traditional airspace users and unmanned aircraft must be adequately mitigated before UAS can routinely utilize the national airspace system (Elias 2012). Small UAS pose a particular challenge, because they operate at low altitudes. Many other aircraft operating at these altitudes do not use electronic transponders to broadcast their position and altitude, and in any case, many small UAS lack the ability to receive

transponder signals. The needed equipment is simply too large and heavy to install on many small UAS (U.S. Government Accountability Office 2012). Currently, these limitations substantially restrict small UAS operations to line-of-sight scenarios, where operators on the ground can provide the necessary capabilities to detect and avoid other air traffic (Elias 2012).

Part of the challenge is that existing technologies do not assure avoidance capabilities under all operational conditions, including autonomous UAS operations or in situations when UAS lose their command guidance links with ground control facilities. Standardized procedures for responding when UAS guidance has been lost are currently lacking, but will be needed to ensure that air traffic controllers and airspace managers can redirect nearby traffic and mitigate collision risks. In conclusion, no single technology is likely to address the complex sense and avoid requirements that are critical for unmanned aircraft integration (Elias 2012).

#### ***3.4.2.2. Risks to people and property on the ground***

Differently from larger UAS that must share the controlled airspace with manned aircraft, smaller UAS are pioneering access to a new region of airspace largely unfamiliar to both pilots and regulators. This low-altitude, obstacle rich environment, below approximately 150 m AGL, presents a variety of challenges to remote operations. These includes people, personal property along UAS routes and other hazards, including nearby trees, buildings, and other obstacles. Consequently, the increased risk of personal and material damage due to small UAS crashes, environmental impacts, annoyance, and loss of personal and property rights should also be evaluated and considered (Atkins & Di Donato 2016).

Thus far, unmanned aircraft testing and operational use have been conducted largely over sparsely populated areas. In the future, however, law enforcement and commercial users are expected to undertake flights over densely populated areas, a prospect which raises specific concerns over safety procedures (Elias 2012). The risk posed to people and property on the ground is a function of both crash likelihood and the potential consequences in terms of loss of life, injury, or property damage. A system safety analysis is performed in (Weibel & Hansman 2005) according to FAA system safety guidelines. While smaller UAS may be expected to crash more frequently, the potential for catastrophic consequences is less given

that these vehicles do not weigh enough or carry enough fuel to cause major damage on the ground. On the other hand, larger UAS, like the MQ-9 Reaper or the RQ-4 Global Hawk, can potentially cause as much damage as a mid- to large-sized corporate jet.

### **3.4.3. Standards addressing UAS systems and operations**

The wide variation in flight environments, missions, and UAS systems, the continuous development of new technologies and the evolution of regulations make the standardization of UAS/payload configurations and operational procedures a challenge (Degarmo 2004). Indeed, since the amount of available UAS platforms (especially small UAS), payload configurations and requested missions is growing rapidly, misleading UAS/payload solutions can be derived without proper standard indications. This will slow down the flight authorization process. Therefore, standards are intended to 1) ensure that the UAS systems and their operations achieve an acceptable level of safety for people and property in other aircraft and on the surface; 2) speed up the authorization process.

There are currently no published standards specific to UAS systems and operations. Standards are a vital element in today's high tech world and often form the basis for government regulation. Many countries have begun moving toward the development of consensus standards as a basis for regulation as well as to facilitate market growth through the development of interchangeable formats and to ensure international harmonization. Furthermore, the inclusion of standards in regulations, if properly developed, has the benefit of allowing changes to be made without having to engage in the lengthy and costly process of creating a rule change. As a result, standards can be changed and regulations made consistent with the change without having to modify regulatory wording (Degarmo 2004).

# Chapter 4

---

## Solutions for Autonomous Navigation

### 4.1. Overview on MEMS-based IMUs for UAS navigation

#### 4.1.1. Introduction

The main features of UAS are the need to exploit compact configurations for the onboard equipment and the capability to perform autonomous operations for a large part of a mission (Broggi *et al.* 2013). Figure 14 illustrates an example of UAS avionics architecture (RAMA UAV Control System 2009). It consists of the Airborne Part (AP) and the Ground Station (GS), comprised of a laptop computer and a Radio Control (RC) transmitter. The airborne part of the system consists of several functional blocks, interconnected via the vehicle bus. Those blocks are the Navigation Unit (NU), Main Control Computer (MCC), Wireless Data Communication Unit (WDCU), two Wireless Control Units (WCU) (for redundancy) and the Servo Control Unit (SCU). The core member of the system is the MCC, where the control and communication algorithms run. The Navigation Unit includes the Inertial Measurement Unit (IMU), Three-Axis Magnetometer (TAM), Global Positioning System Receiver (GPS) and the Data Acquisition Module (DAM). All sensors

are connected to the DAM, the purpose of which is to synchronously sample all the data, pre-process it (filtering, unit conversion, etc.) and send it to other control system nodes.

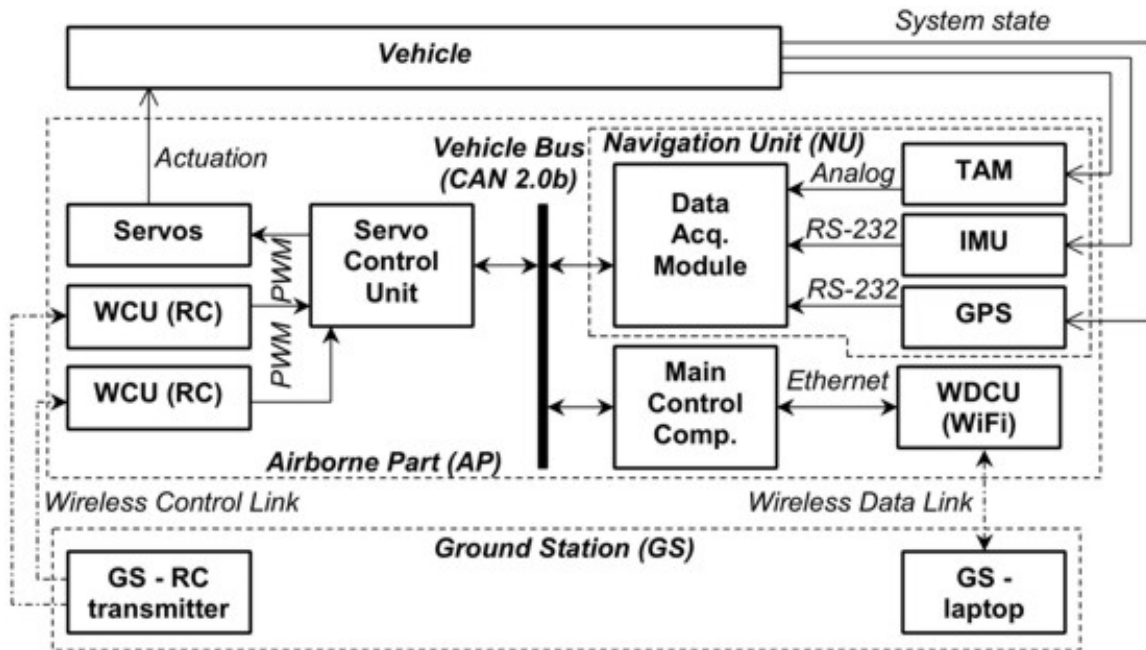


Figure 14. Example of UAS avionics architecture (RAMA UAV Control System 2009).

The IMU, composed by triaxial sets of gyros and accelerometers, is a reference enabling technology for motion sensing that allows the above reported systems to attain the desired performance in terms of compactness and autonomy. The IMU has the advantage to perform localization, velocity, and attitude determination independently on the measurement of external force fields, e.g. magnetic and aerodynamic, and without any need of radio link or radar signal input. Therefore, it is the most robust and reliable source of reference for navigation. This condition is determined by their capability of estimating the first integral terms of rigid body motion, such as acceleration and attitude rate. Therefore, the processing scheme is derived from basic laws of Dynamics, which are more effective than the ones related to field of forces (Titterton & Weston 2004).

Standing the above reported considerations, the requirements for IMUs to be installed onboard UAS are quite different from the ones peculiar to traditional systems. First, compactness is very important. It is related to the volume occupied by the units, but also to their mass and inertia. Moreover, power consumption is another important issue, since most systems are powered by batteries. Finally, the required economic resources to acquire and

maintain the units has to be limited in order to justify their installation onboard low-cost transportation platforms (Schmidt 2010).

A typical solution to meet the aforementioned requirements is to use IMUs manufactured by exploiting Micro Electro-Mechanical Systems or MEMS inertial sensors (Barbour *et al.* 2011). The use of IMUs based on MEMS technology improves cost and size performance of more than one order of magnitude with respect to those achievable through Fiber Optic Gyros or FOG. This is the reason why significant effort has been lavished on developing MEMS-based IMUs that can be installed on last-generation transport platforms (Schmidt 2015). The advantage in adopting MEMS-based IMUs can be so relevant in some applications that they are used to retrofit traditional inertial units in already deployed transport systems (Ryan & Miller 2010; Schmidt 2010).

#### **4.1.2. MEMS gyroscopes**

##### ***4.1.2.1 Introduction***

MEMS gyros are a micro-machined version of Coriolis Vibratory Gyros since they exploit Coriolis force effect to estimate inertial attitude rates (Titterton & Weston 2004). MEMS gyros can be quartz or silicon based in construction (KVH 2014) and they are manufactured by using the same technology of micro-chips. This peculiarity allows them to be more suitable than traditional sensors to meet compactness and low-power consumption requirements. Also, the specific manufacturing process can assure a valuable cost reduction in large scale applications (Sheng & Zhang 2015).

They can be classified into a wide category of systems with different performance in terms of error characteristics, integrity, robustness to environmental solicitations, and reliability. For instance, among MEMS gyros there are large differences in terms of bias instability, random noise levels and scale factor error (KVH 2014). Therefore, the applications of interest can be also very different.

##### ***4.1.2.2 Principle of operation***

MEMS gyroscopes use a vibrating mechanical element as a sensing element for detecting the angular rate. Their operation is based on the transfer of energy between two vibration modes caused by the acceleration of Coriolis (Passaro *et al.* 2017). It is worth

noting that they do not have rotating parts that require bearings and this allows an easy miniaturization.

To better understand the concept, the structure of a  $z$ -axis MEMS gyroscope is shown in Figure 15. It has two perpendicular vibration directions,  $x$ -axis and  $y$ -axis, which correspond to drive mode and sense mode respectively. When the gyroscope is powered on, the mass block will vibrate harmonically in the  $x$ -axis direction due to the periodic electrostatic force. Given the angular velocity  $\Omega$  along the  $z$ -axis, the mass will sense the Coriolis force in the  $y$ -axis direction. Therefore, the  $y$ -axis vibration (sense mode) is caused by the Coriolis force and the angular velocity  $\Omega$  can be calculated through the mass displacement in the  $y$ -axis direction (Tang *et al.* 2014).

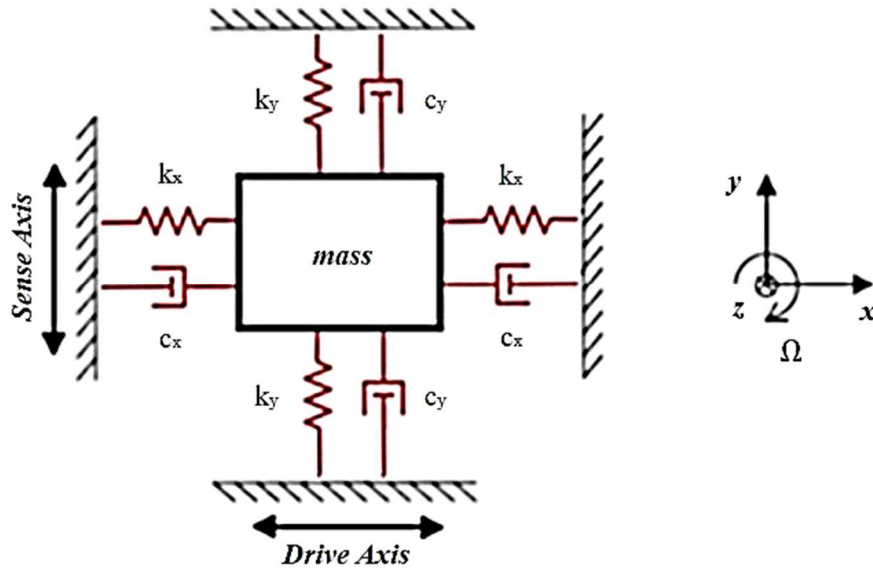


Figure 15. Schematics of a  $z$ -axis MEMS gyroscope.

According to the Newton's second law of motion, the following equations describe the gyro's vibration in the  $x$ -axis and  $y$ -axis directions:

$$\begin{aligned} m \ddot{x} &= -k_x x - c_x \dot{x} + f_d \\ m \ddot{y} &= -k_y y - c_y \dot{y} + F_{Cy} \end{aligned} \quad (1)$$

where  $m$  is the mass,  $c_i$  is the damping coefficient,  $k_i$  is the stiffness of the elastic beams all in  $i$ -axis direction ( $i = x$  or  $y$ ),  $f_d$  is the electrostatic driving force and  $F_{Cy}$  is the Coriolis force. The drive mode is excited along  $x$  by applying a force  $f_d$ , while the sense mode is excited

along  $y$  by the Coriolis force  $F_{Cy}$ . It is worth noting that the displacement along the sense axis is proportional only to the angular velocity  $\Omega$ . Being  $Q_x$  and  $Q_y$  the quality factors and  $\omega_x$  and  $\omega_y$  the resonance frequencies of the driving and sensing mode respectively, the displacement of the mass  $m$  along the sense axis  $y$  assumes the following expression (Passaro *et al.* 2017), (Maenaka *et al.* 1996):

$$\Delta y = 2\Omega \frac{F_{Cy} Q_x}{m \omega_x} \frac{1}{\sqrt{(\omega_x^2 + \omega_y^2)^2 + \left(\frac{\omega_x \omega_y}{Q_y}\right)^2}} \quad (2)$$

#### 4.1.2.3 Performance grades

From the perspective of the navigation systems designer, the key performance parameters to define the gyro accuracy (or the error sources) are the following (Faruqi 2016):

- Bias, which is any non-zero sensor (rate) output when the input rate is zero;
- Scale factor error that is due to manufacturing tolerances or ageing;
- Nonlinearity between input and output;
- Asymmetry of the scale factor that is generally a result of the electronics component mismatch;
- Thermal and other spurious noise including “random walk” noise effects;
- Scale factor dead-zone due to mechanical friction or lock-in for laser gyro;
- Quantization error that is present in all devices with digital output.

The largest errors are usually bias stability (measured in deg/hr or rad/hr), and scale-factor stability (which is usually measured in parts per million (ppm) of the sensed inertial quantity). Figure 16 compares the bias and scale factor stability performance for traditional gyro technologies, such as mechanical, FOG, RLG and DTG, and MEMS gyros (revised version of the figure in (Schmidt 2010)).

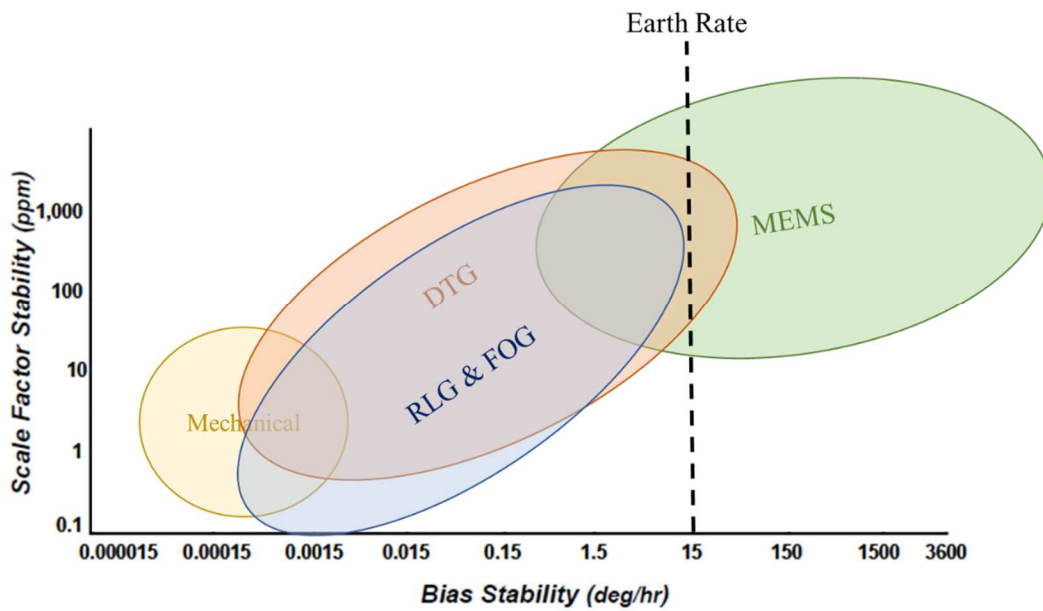


Figure 16. Bias and scale factor stability performance for traditional gyro technologies, such as mechanical, FOG, RLG and DTG, and MEMS gyros (revised version of the figure in (Schmidt 2010)).

Gyros accuracy can be divided into performance grades according to bias stability specifications, with the lowest grade being used for consumer products, and the highest performing grades being used for strategic applications (Table 2). The bias stability measurement indicates how stable the bias of a gyro is over a certain specified period. In general, a reduced bias stability means reduced error when integrating the gyro output over time. A gyro with reduced bias stability will lead to reduced errors in position estimates for an INS. As might be expected, the performance grade of a gyro or IMU also determines its comparative cost (KVH 2014).

MEMS gyros have shown themselves to be an extreme enabling technology for new applications. Their small size, extreme ruggedness, and potential for very low-cost and weight means that numerous new applications have been, and will be, able to utilize inertial guidance systems. This was unthinkable before MEMS technology. MEMS gyros are expected to replace many of the current systems using traditional sensors (KVH 2014). However, MEMS are typically used in consumer to industrial grade applications (KVH 2014). As shown in Figure 16, the low and medium performance range is dominated by MEMS gyros (Schmidt 2010). MEMS technology has struggled to reach tactical grade quality (Barbour 2010), and is only now reaching that performance.

Table 2. Gyro Grades Based on Bias Stability (KVH 2014).

<b>Performance Grade</b>	<b>Bias Stability</b>
Consumer	30-1000°/hr
Industrial	1-30°/hr
Tactical	0.1-30°/hr
High-end Tactical	0.1-1°/hr
Navigation	0.01-0.1°/hr
Strategic	0.0001-0.01°/hr

### 4.1.3. MEMS accelerometers

The basic principle of operation behind the MEMS accelerometer is the displacement of a small proof mass etched into the silicon surface of the integrated circuit and suspended by small beams. Consistent with Newton's second law of motion, as an acceleration is applied to the device, a force develops which displaces the mass. The support beams act as a spring, and the fluid trapped inside acts as a damper, resulting in a second order lumped physical system. This is the source of the limited operational bandwidth and non-uniform frequency response of accelerometers (Elwenspoek & Wiegerink 2012).

MEMS accelerometers may be divided into two distinct classes, reflecting the manner in which acceleration applied to the case of the device is sensed (Titterton & Weston 2004):

- The displacement of a proof mass supported by a hinge or flexure in the presence of an applied acceleration, that is, a mechanical sensor using silicon components. Sensors belonging to this class can provide acceleration measurements to an accuracy compatible with inertial (25 micro-g) or sub-inertial quality (1 milli-g).
- The change in frequency of a vibrating element caused by the change in tension in the element as a result of the mechanical loading that occurs when the element is subjected to acceleration. Sensors belonging to this class tend to have a potentially higher accuracy capability approaching 1 micro-g.

The current state of development is that the entire sensor may be constructed entirely from silicon, with the exception of the hermetically sealed case, which still tends to be metallic.

#### **4.1.4. UAS navigation**

UAS navigation is typically based on the integration of low-cost MEMS-based IMUs with GNSS and magnetic sensors. Indeed, IMUs generate the output measurement, i.e. position, velocity, and attitude estimates by integrating accelerations and attitude rates. Therefore, they have two main limitations, i.e. they are not capable of estimating autonomous initial conditions of motion and they suffer from measurement error drift with time. For this reason, IMUs are always supported by aiding systems that are used to overcome the above mentioned limitations through the application of a proper data fusion framework (Groves 2013).

##### ***4.1.4.1. Magnetometer/INS integration***

Heading determination is one of the most important aspects of navigation solutions (Wahdan *et al.* 2014). Magnetometer is a low-cost sensor that does not suffer from mathematical integration errors and can provide an absolute heading from magnetic north by sensing the Earth's magnetic field (Titterton & Weston 2004).

As may be seen in Figure 17, the axis of the Earth's magnetic field can be modelled as a simple bar magnet. This magnetic dipole has its field lines originating at a point near the south pole and terminating at a point near the north pole, but the field is skewed from true geodetic north by ~11.5 degrees. The Earth's field lines enter the Earth at a considerable angle to the local horizontal plane, and this angle is called the magnetic angle of inclination (magnetic dip). In the United States and Europe this angle is around 70 degrees (Moir *et al.* 2013).

The components of the Earth's magnetic field in the local horizontal plane are used to determine the compass heading with reference to the north magnetic pole. However, allowance must be made for the fact that the magnetic and geodetic poles do not coincide, and also for the fact that there are considerable variations in the Earth's magnetic characteristics across the globe. These factors are measured and mapped across the globe such that the necessary corrections may be applied. The correction term is called angle of

declination (magnetic variation) and is a corrective angle to be added to/subtracted from the magnetic heading to give a true (geodetic) compass heading. Positive angular declinations represent easterly corrections, while negative angles represent westerly corrections. These corrections are measured, charted, and periodically updated (Moir *et al.* 2013).

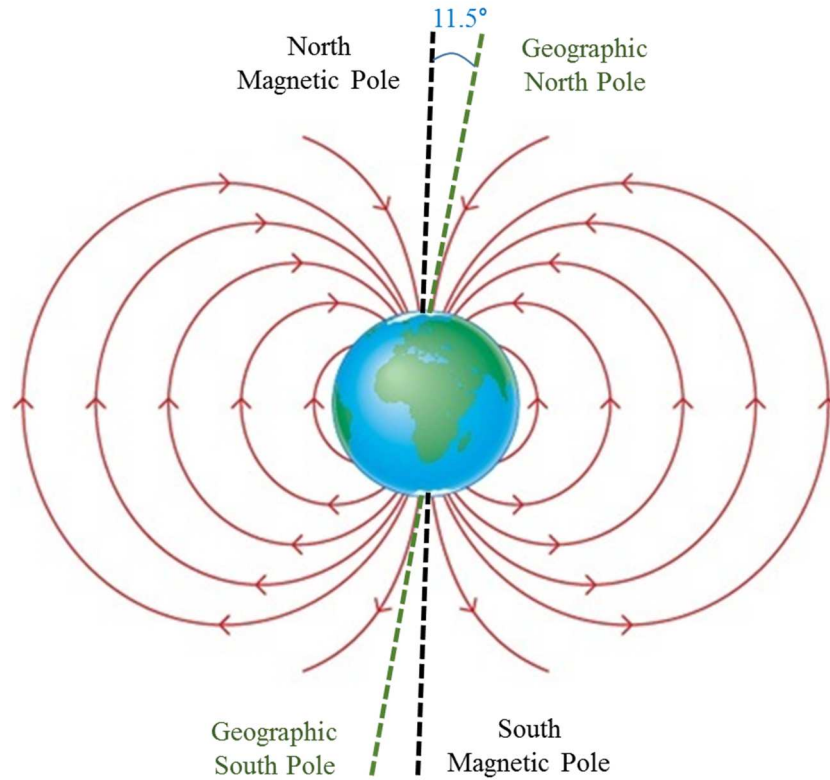


Figure 17. Earth's magnetic field (revised version of the figure in (Moir *et al.* 2013)).

The Earth's magnetic field,  $H$ , is the vector sum of components  $h_x$ ,  $h_y$ ,  $h_z$  measured in the orthogonal axis set shown in Figure 18, where the angles of inclination and declination are shown. The Heading  $\psi$  can be obtained from the two levelled horizontal magnetometer signals as (Wahdan *et al.* 2014):

$$\psi = \arctan\left(\frac{h_y}{h_x}\right) \pm D \quad (3)$$

where  $h_x$  and  $h_y$  are the two levelled measurements of the Earth's magnetic field vector in the reference frame of the magnetometer (or the device comprising the magnetometer) and  $D$  is the declination angle that is function of latitude and altitude.

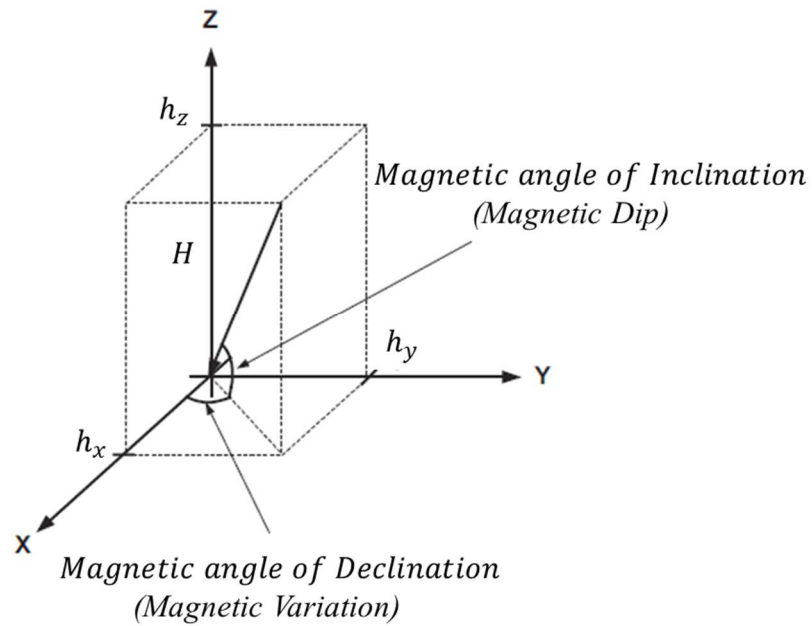


Figure 18. Earth's magnetic field components (revised version of the figure in (Moir *et al.* 2013)).

However, magnetic heading measurements are subject to errors induced by accelerations and local magnetic anomalies. A more stable heading can be obtained by the integration INS/magnetometer. In this integration, the inertial sensors smooth out magnetometer noise, while the magnetometer calibrates the inertial sensors drift. The integration is usually performed by using the Kalman Filter (Groves 2013).

#### **4.1.4.2. GNSS/INS integration**

The need for accurate and reliable navigation, for long-range flights as well as for precision approach and landing systems has focused attention on the use of coupled or integrated GNSS/INS systems. This is particularly significant for MEMS inertial sensors, which, compared to higher-grade systems, can experience large errors over short time intervals. This is mainly due to large uncertainties in the sensor output. INSs built on these sensors are vulnerable to nonlinear error behaviour, especially when the attitude errors become very large (Titterton & Weston 2004).

The aviation community has long recognized that GNSS and INS provide complementary benefits. GNSS provides accurate positioning that does not degrade over time. INS provides autonomous, high frequency, low noise positioning that is not susceptible to interference or jamming (Manfred & Ryno 2008). An integrated GNSS/INS navigation system exploits the best characteristics of both systems. This integration allows

the estimation and correction of errors caused by the INS and assists navigation in cases of GNSS outages, data degradation, and jamming (Lee & O’Laughlin 2000; Niu *et al.* 2007).

The integration provides the following advantages over the individual systems (Bhatti *et al.* 2007):

- The integrated system is more accurate than the individual systems;
- More trust can be placed on its output because of the redundancy provided by an additional navigation system;
- The integrated output is provided at a higher rate than GNSS because of the higher data rate of INS;
- The integrated system will be available even during GNSS outage. The time of availability of accurate navigation solution is limited by the quality of the INS.

An extensive review of techniques based on the integration of low cost INSs and GNSS can be found in (Hasan *et al.* 2009). There are three basic types of GNSS/INS integration, loosely coupled, tightly coupled and or ultra-tightly coupled or deeply integrated.

With a loosely coupled integration, a navigation processor inside the receiver calculates position and velocity using GNSS observables only. Subsequently, the GNSS output (position and velocity) are used to update the output of an INS utilizing a data fusion technique. In a loosely coupled system, shown in Figure 19, the receiver can be treated as a "black box". A disadvantage of this integration is that the data fusion heavily depends upon the GNSS solution. Hence, if the GNSS solution is not available (e.g., when less than four satellites are available) the integrated solution is no longer possible. In such a case, the performance of the integrated system is limited to its inertial coasting capability. The time for which a system can coast depends primarily on the quality of inertial sensors (Lee & Ericson 2004).

The tightly coupled filter, instead, benefits from GNSS measurement updates even if there are less than four satellites available for a complete navigation solution. In this approach, raw output from the GNSS (pseudo-range, pseudo-range rate) are used in conjunction with the INS error model to estimate the navigation errors and the corrected states (i.e. position, velocity, acceleration, attitude, etc.) of the UAS. A disadvantage of this filter is that it responds more slowly to INS errors than the loosely coupled system (Gautier 2003). Figure 20 shows a tightly coupled integration.

In the ultra-tight approach, integration occurs at the GNSS tracking loops which are controlled by the blended navigation filter (Pany & Eissfeller 2006). The GNSS receiver in this case is no longer an independent navigator since its operation is also partly dependent on INS information. The potential benefits of the deep integration are achieved at the expense of a significant increase in complexity, computational load, and tight time synchronization (Kim *et al.* 2003). Figure 21 shows an ultra-tightly coupled or deeply integrated GNSS/INS system.

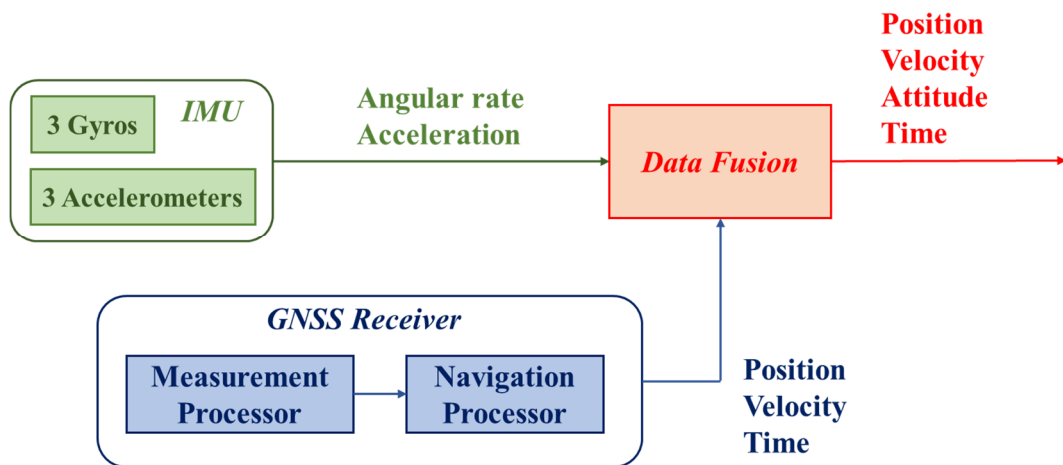


Figure 19. Loosely coupled GNSS/INS integration.

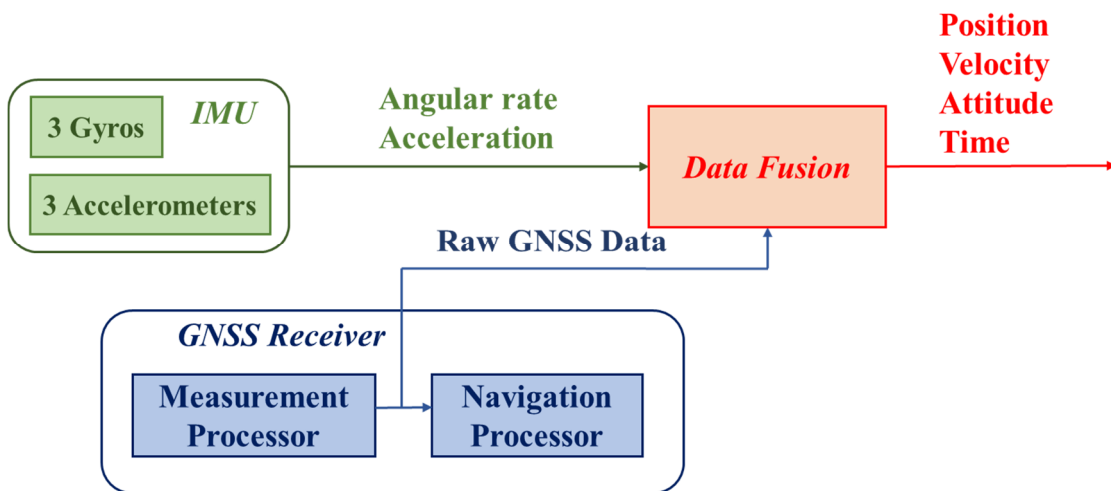


Figure 20. Tightly coupled GNSS/INS integration.

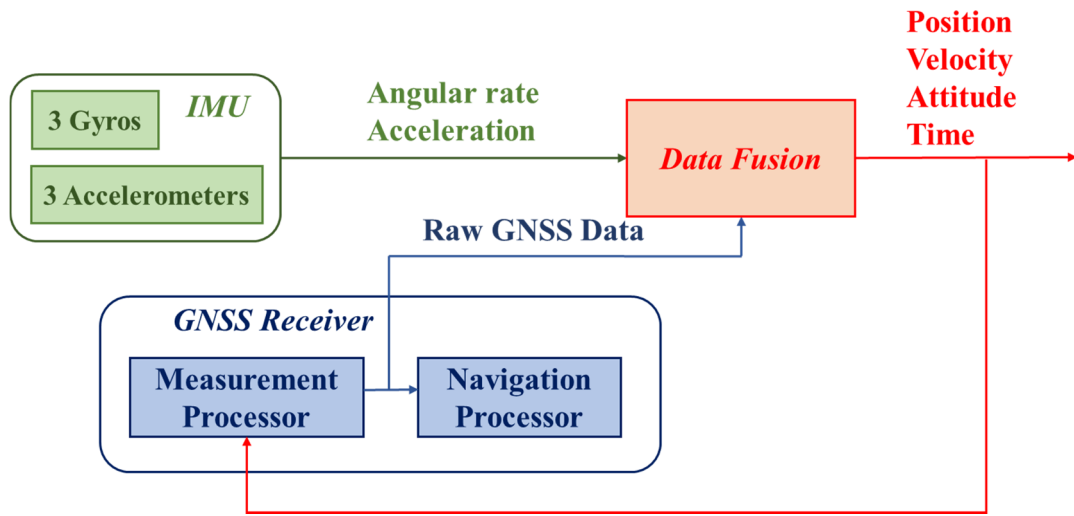


Figure 21. Ultra-tightly coupled or deeply integrated GNSS/INS system.

#### 4.1.4.3. Data fusion techniques

A description of the different data fusion techniques is presented in (Fasano *et al.* 2011, 2016a; Gross *et al.* 2010a; Jarrell *et al.* 2008). A comparative analysis of sensor fusion algorithms for UAS applications is presented in (Gross *et al.* 2012). Since the state of a system must be estimated from noisy sensor information, state estimator should be employed to fuse together data from different sensors to produce an accurate estimate of the true system state. When the system dynamics and observation models are linear, the state estimates may be computed using the Kalman Filter, extensively described in (Groves 2013).

The Kalman Filter is essentially based on two groups of equations: the “Time Update Equations” and “Measurement Update equations”, as reported in Figure 22 in discrete time form. The time update equations can be thought of as “predictor” equations, while the measurement update equations can be thought of as “corrector” equations (Jarrell *et al.* 2008; Tirri 2014). In Figure 22,  $\hat{x}_k$  is the state vector estimate,  $\Phi_{k-1}$  is the transition matrix,  $P_k$  is the error covariance matrix,  $H_k$  is the measurement matrix,  $Q_k$  is the system noise covariance matrix,  $R_k$  is the measurement noise covariance matrix,  $K_k$  is the Kalman gain matrix,  $z_k$  is the measurement vector. The subscript  $k$  is commonly used to denote the iteration, whereas the symbols – and + respectively indicate the propagation stage and the correction stage.

It is, in general, based on a few assumptions: the system state evolves according to a known linear equation driven by a known input and an additive process noise, which is zero-mean white (uncorrelated in time) with known covariance matrix  $Q_k$ . Moreover, measurements are a known function of the state with an additive measurement noise, which is again zero-mean white with known covariance  $R_k$ . Required initial parameters are the initial state with its uncertainty (that is, its covariance). System and measurement noise are assumed to be uncorrelated. However, in most applications of interest the system dynamics and observation equations are nonlinear and suitable extensions to the Kalman filter have been sought (Ristic *et al.* 2004).

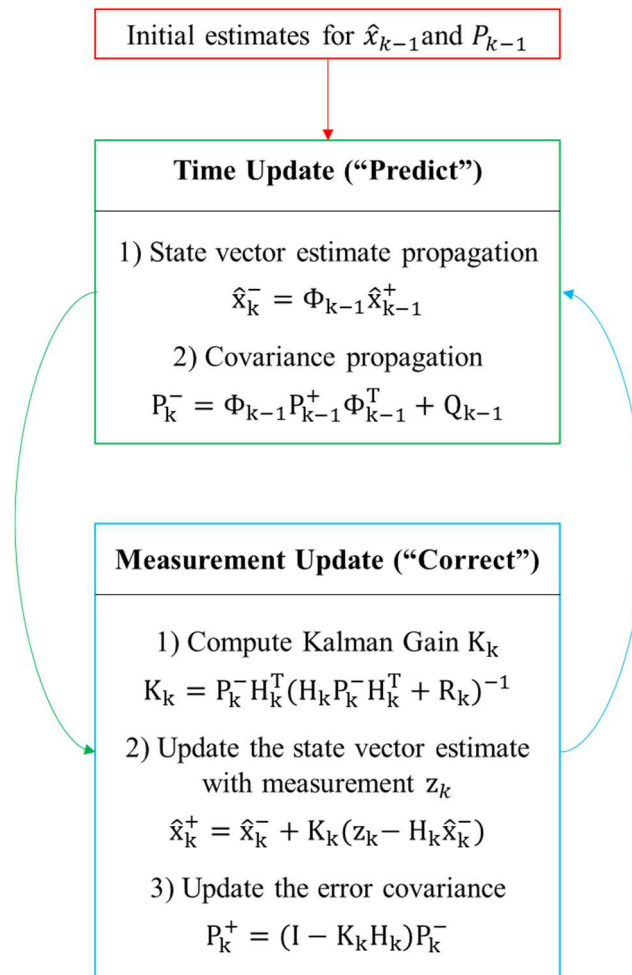


Figure 22. Kalman filter scheme.

In the core of navigation system development lies the problem of estimating the states of a non-linear dynamic system. When it comes to state estimation for nonlinear systems,

however, there is no single solution available that clearly outperforms all other strategies. The three main approaches are (Hasan *et al.* 2009):

- The Linearized Kalman Filter (LKF) or the Extended Kalman Filter (EKF). The LKF can be applied if all sources of information are conveniently modelled by linear dynamical and measurement equations and the noise is modelled as Gaussian white noise. It can be demonstrated (Gelb 1974) that under the Gaussian assumption, the Kalman Filter is the minimum mean-square error state estimator. The EKF, instead, is a suboptimal technique that can be applied if some sources of information have a nonlinear dynamical model, but their behaviour can be adequately modelled through the linear term of Taylor series of process and measurement equations in the vicinity of a known solution. The noise must be modelled as Gaussian white noise.
- Sampling-based filters, such as the Unscented Kalman Filter (UKF) and Monte Carlo Sequential Sampling. The UKF is also suboptimal and is used when the sole linear term in the Taylor series is not enough accurate to model process propagation. Monte Carlo Sequential Sampling techniques exploit Monte Carlo integration by removing any type of hypothesis on process model, measurement model, and the type of noise. The most common method is represented by Particle Filters (Tirri 2014). In this case, a large set of samples of the Probability Density Function (PDF), i.e. the particles, are propagated by nonlinear update function.
- Artificial Intelligence (AI)-based methods, such as Artificial Neural Networks (ANN) or Adaptive Neural Fuzzy Information System (ANFIS). In past few decades, neural network and fuzzy control have been widely used in many applications such as control, navigation systems and so on. It is known that the neural network has learning ability and is a good choice for modelling dynamic and complex process. On the other hand, the fuzzy control has an important feature where it is a very effective and practical approach to the modelling of nonlinear, time varying and complex systems by using a set of linguistic rules, which may come from a control engineer or an experienced operator for a particular system.

#### **4.1.4.4. Integrity monitoring**

Navigation applications require that the highest level of safety and other performance standards are satisfied. These standards are known as the Required Navigation Performance (RNP) parameters: accuracy, integrity, continuity, and availability, with integrity being the parameter directly linked to safety. Integrity is a measure of the trust that can be placed in the correctness of the information provided by a navigation system (Panagiotakopoulos *et al.* 2013). A navigation system is required to deliver an alert or a warning of any malfunction because of a set alert limit being exceeded, to users within a specified time-to-alert. Integrity risk is defined as the probability that the positioning error exceeds the alert limit and that the event is undetected (Panagiotakopoulos *et al.* 2013).

The integrity monitoring of the GNSS/INS integrated system follows in the footsteps of the integrity monitoring of GNSS (Bhatti *et al.* 2007), extensively described in (Feng *et al.* 2006; Ochieng *et al.* 2003; Sabatini *et al.* 2013a, 2013b, 2015). Integrity monitoring in the horizontal domain requires an alert to be raised whenever the horizontal position error is larger than the horizontal alert limit. Therefore, detection performance involves three basic parameters: test statistic, decision threshold, and Horizontal Protection Level (HPL). These parameters are described below (Feng *et al.* 2012; Lee & O’Laughlin 2000; Panagiotakopoulos *et al.* 2013):

- **Test Statistic vs. Decision Threshold.** For a decision of whether to raise a flag or not to declare presence of a failure requires two quantities: a test statistic that is an observed quantity and decision threshold to compare the test statistic against. A test statistic is a value calculated from a sample of data. It is used to decide whether or not the null hypothesis should be rejected in a hypothesis test. A test statistic must be chosen such that it will summarize the information in the sample that is relevant to the hypothesis. The construction of a test statistic depends on the probability model (distribution) and the hypotheses under question. The decision threshold should be chosen on the basis of statistical characteristics of the test statistic so that a false integrity alert (alert that occurs in a fault-free condition) occurs no more than at some specified rate, which is typically 10<sup>-5</sup>/hr.
- **Horizontal Protection Level.** The HPL is an upper bound that a horizontal position error shall not exceed without being detected. If it is exceeded, it shall be detected

with a 0.999 probability. In other words, a given integrity method must guarantee that a user position error, which is not a directly observable quantity, will be within the bound unless an integrity alert is raised. HPL is an important parameter that determines the availability of integrity function. That is, if HPL is less than the Horizontal Alert Limit (HAL) for a given phase of flight, integrity function is available, and vice versa.

As described in the previous section, the loosely coupled system provides benefits in terms of the navigation performance over the individual systems. However, the integrity performance of the loosely coupled system is restrictive in nature due to the fact that GNSS measurements are not accessible. Hence, healthy GNSS measurements are not of any use in the situation when the navigation solution is corrupted by a faulty measurement. Therefore, to get real benefits in integrity monitoring, measurement domain coupling methods are recommended (Bhatti *et al.* 2007).

Integrity monitoring methods for the tightly coupled system are based upon variations in the selection of test statistics, decision thresholds and horizontal protection limits. There are two main approaches normally employed to determine the test statistic (Bhatti *et al.* 2007):

- The use of the innovation of the Kalman filter (Diesel & King 1995; Nikiforov 1995);
- The use of the difference between the main filter solution and the sub-filter solution (Brenner 1995).

The decision threshold against which the test statistic is compared is determined in one of two ways (Bhatti *et al.* 2007):

- The threshold is a function of the standard deviation of the separation between the full solution and the sub-solutions, multiplied by a constant determined statistically. It is assumed that the test statistic is Gaussian in nature and hence the constant is calculated so that the given probability of false alert is not exceeded (Brenner 1995);
- When the test statistic is a function of innovation that has multiple Gaussian distributed components, the threshold is chosen using the chi-square distribution.

The probability of false alert is used to arrive at the value of the threshold (Diesel & King 1995).

The HPL can be determined either by using separation statistics between the full filter and sub-filters (Brenner 1995) or by fusing multiple terms. There are three major current integrity monitoring algorithms for integrated systems: 1) Multiple solution separation (MSS) method; 2) Autonomous integrity monitoring by extrapolation method (AIME); 3) Optimal fault detection. They are described in (Bhatti *et al.* 2007).

An integrity monitoring method suggested for ultra-tightly coupled systems is the GNSS Inertial - RAIM (GI-RAIM) method (Gold & Brown 2004). It is based on the Bounded Probability of Missed Detection concept. Based on a pre-filter, it is anticipated that a certain satellite is faulty. By excluding this satellite, a position solution is computed. From the comparison of this solution with the full solution, the contribution of the faulty satellite to the radial position error is estimated with a high probability. The algorithm ensures that this fault characterization minimizes the missed detection risk. However, the condition is that a sufficient number of satellites is available in a good geometrical configuration. It is claimed that Horizontal and Vertical Alert Limit values close to 1 m can be achieved with this algorithm. But it should be noted here that this accuracy is achieved by using the GNSS carrier phase observable. The availability of the carrier phase solution is limited by the resolution of integer ambiguity, which is not always guaranteed. In the GI-RAIM integrity monitoring, a pre-filter is used to flag the faulty GNSS signal. In this way, corrupt GNSS data are prevented from propagating back into the main navigation filter (Bhatti *et al.* 2007).

## **4.2. Improving thermal compensation of MEMS gyro bias**

The IMU is the primary source of reference about attitude. Furthermore, its integration with a GNSS receiver-chip provides a navigation system that has several advantages over each individual system (Groves 2013). However, good bias correction performance is requested for gyros to have a robust output even in case of temporary non nominal operation of measurement systems in the Kalman Filter, such as GNSS, air data and magnetometers.

MEMS gyros have significant limitations in terms of sensitivity to environmental conditions. Their output average value, i.e., sensor bias, drifts with temperature, with a

strongly non-linear trend. Consequently, bias estimation and thermal compensation are critical operations that must be well accomplished to achieve the best navigation performance while using inertial units with MEMS gyros (Niu *et al.* 2013; Zhuang & El-Sheimy 2016).

#### 4.2.1. MEMS gyro bias temperature dependence model

The effect of environmental temperature is one of the most critical error sources in MEMS gyroscopes (Niu *et al.* 2013). MEMS architecture is fabricated with silicon, which is a thermo-sensitive material. The modulus of elasticity has an approximate linear relationship with temperature (Tang *et al.* 2014).

$$E = E_0 - C_E E_0 (T - T_0) \quad (4)$$

where  $E$  and  $E_0$  are the elasticity modulus at temperature  $T$  and  $T_0 = 300$  K and  $C_E$  is the temperature coefficient of the silicon elasticity modulus. Since the MEMS gyros' stiffness is proportional to the elasticity modulus, also the gyros' stiffness has an approximate linear relationship with temperature:

$$k = k_0 - C_E k_0 (T - T_0) \quad (5)$$

where  $k$  and  $k_0$  are the gyro's stiffness at temperature  $T$  and  $T_0$ . Therefore, temperature variation leads to the change of MEMS gyros' stiffness, which causes the change of the resonance frequencies  $\omega_x = \sqrt{k_x/m}$  and  $\omega_y = \sqrt{k_y/m}$ . Since the relationship between the resonance frequencies  $\omega_x$  and  $\omega_y$  and temperature is strongly non-linear and the main reason for gyroscope zero bias is the offset of its natural frequency (Tang *et al.* 2014), bias has a non-linear dependence on temperature. Furthermore, a finite element model of MEMS gyroscope is presented in (Wang *et al.* 2014) to illustrate the mechanism of resonant frequency shift due to temperature change. It shows that drive resonant frequency descends more rapidly than the sense resonant frequency, which also presents fluctuations. This particular trend is also evident in (Xia *et al.* 2009). It is caused by the large thermal stress in the regions of drive spring beams while almost no thermal stress in the regions of sense spring beams (Wang *et al.* 2014). Therefore, temperature variation does not affect both modes the same amount. This determines a change of the frequency mistuning.

An additional part of the error observed is due to the sensitivity of the gyro's control electronics to temperature. MEMS gyroscopes are based on the Coriolis coupling effect, which transfers the energy from the drive mode to sense mode by inducing the Coriolis force in the sense direction (Cui *et al.* 2009). Since the Coriolis force is proportional to the external angular rate only on the premise of a non-varied velocity along the drive axis, it is fundamental for the gyro control circuits to maintain a constant amplitude of the drive vibration. A commonly used approach is utilizing Automatic Gain Control (AGC) (Cui *et al.* 2009). Experimental results presented in (Xia *et al.* 2009) and (Shcheglov *et al.* 2000) show a dependence of the AGC voltage on temperature, which induces drift in the drive amplitude.

Finally, the influence of temperature on the package of MEMS devices is described in (Joo & Choa 2007). It generally consists of various materials that have different coefficients of thermal expansion. Therefore, temperature change will induce thermo-mechanical stress that could cause deformation of the MEMS structure, resulting in frequency change or breakage of the structure.

#### **4.2.2. Traditional bias estimation and compensation process**

Because of the above reported discussion, thermal calibration is a critical activity that allows estimating three terms (Fontanella *et al.* 2018b):

1. Bias thermal drift;
2. Scale factor thermal drift;
3. Thermal variation of random noise standard deviation.

The most critical error component to be compensated in order to let MEMS gyros reach their best level of performance is the bias thermal drift. In case no information about sensor's temperature is provided, bias drift can be modelled as a random term, which refers to the rate at which the error in an inertial sensor accumulates with time. However, knowing the sensor's temperature, thermal drifts can be regarded as deterministic errors. The effect of thermal calibration on scale factor is less significant, according to typical sensor's performance sheets. Regarding noise, estimating the standard deviation does not allow for immediate correction due to its intrinsic nondeterministic nature. However, the assessment of random noise standard deviation is an important information for estimating the process

covariance matrix of Extended Kalman Filters that are used to perform integrated navigation with aiding systems (Fontanella *et al.* 2016, 2018b).

The traditional approach (IEEE Standards Board 2004) consists in performing thermal tests in a climatic chamber over the requested temperature intervals, in order to derive the calibration function that allows the correction of bias thermal drift. The chamber, indeed, allows for performing controlled thermal solicitations on the unit by assigning proper temperature profiles. Then, the calibration function is developed by adopting the polynomial fitting and, during the real-time operation of the unit, it is applied to correct the sensor output before any other processing step (Wang *et al.* 2010). A further reduction of bias can be realized by estimating its residual amount within a data fusion framework, such as an augmented state Kalman filter, in which bias is included as a state in addition to errors on attitude, position, and velocity (Savage 1998). In summary, the traditional approach to estimate gyro bias is a cascading of calibration and Kalman filtering (Groves 2013). However, it has two main limitations:

1. The typical MEMS gyro bias trend model is strongly non-linear with added hysteresis (Xia *et al.* 2009), (Gulmammadov 2009). However, polynomials are not efficient to model these local changes of trend since they have fixed shapes as a function of their order;
2. The overall process is time consuming and expensive. Indeed, it is a cascading of two algorithms, thermal calibration and Kalman filtering. This aspect also reduces system accuracy, reliability, and maintainability.

#### ***4.2.2.1. Thermal compensation through polynomial fitting***

The classical strategy adopted to develop the thermal model of MEMS gyro bias is the polynomial fitting. Once the order of the polynomial is selected, its coefficients can be derived by the Least Mean Squares (LMS) curve fitting, since it is simple and easy for constituting the temperature model of the sensor's bias. Using a polynomial of order  $m$  to describe the approximate function (regression equation) between the experimental data, the following expression can be obtained (Xia *et al.* 2009):

$$V_i = B_i - \sum_{j=0}^m a_j T_i^j \quad (6)$$

$T_i$  denotes the temperature,  $B_i$  denotes the corresponding gyro output and  $V_i$  denotes the error between the gyro output and the value calculated by the regression equation ( $i = 1, 2, \dots, n$ , where  $n$  is the number of samples of static AHRS data). According to the LMS theory, the square of  $V_i$  should be set to the minimum to obtain the optimum value for the coefficients  $a_j$  (Xia *et al.* 2009):

$$\varphi(a_0, a_1, \dots, a_m) = \sum_{i=1}^n V_i^2 \rightarrow \min \quad (7)$$

Even if this technique is a good compromise, non-negligible residuals can be determined for specific temperatures, because of the typical oscillatory shape of a polynomial curve. These residuals can determine large attitude errors when gyro measurements are integrated to perform navigation.

#### **4.2.2.2. ZUPT filter**

Zero Velocity Update or ZUPT filter is a filter used to remove residual errors on navigation state terms and bias at startup for an IMU. It requires that the unit is held fixed with respect to the locally level frame for some minutes, since the assumption that the unit is stationary is the aiding information used by the Kalman filter, i.e., the filter measurement model. In stationary condition, any form of linear and angular rate, except the Earth rate, is considered as an error.

The ZUPT filter is used to get accurate initial attitude and inertial sensor bias when tactical grade gyros are available, i.e., gyros that have a bias instability that is less than 1 degree per hour (Titterton & Weston 2004). In the case non tactical grade gyros are installed in the IMU, the ZUPT filter is used to estimate just the bias. Indeed, gyro bias cannot be estimated just by averaging sensor output, since the size of averaging time window could not be coherent with thermal variations that induce bias drift. Since thermal variations depend on environmental conditions, nothing is known about their characteristic time. Moreover, when the unit is turned on in stationary condition, no information is provided about how long it is going to stay motionless. For this reason, the ZUPT filter has a

significant practical interest also for IMUs equipped with standard grade gyros, such as the Attitude and Heading Reference Systems or AHRS installed on aircraft (Sheng & Zhang 2015) or the Land Navigators installed on ground vehicles (Wang *et al.* 2015).

#### 4.2.2.2.1. General description

The standard ZUPT filter is accurately described in (Groves 2013). After a brief coarse alignment phase, the INS attitude and the Position, Velocity, Time (PVT) initial solution are “frozen”. Then the inertial navigation equations are numerically integrated. However, the upgraded attitude and PVT solution are different from their initial values. Since the host vehicle is at rest and non-rotating, these changes can be only due to uncompensated accelerometers and gyroscopes errors. Measurements of the difference between the INS output and the reference are input to a Kalman filter, which restores the initial conditions and estimates the accelerometer and gyro biases. Since ZUPT filter can be only applied when the host vehicle is stationary and non-rotating, it must last only few minutes. Figure 23 shows the block diagram model.

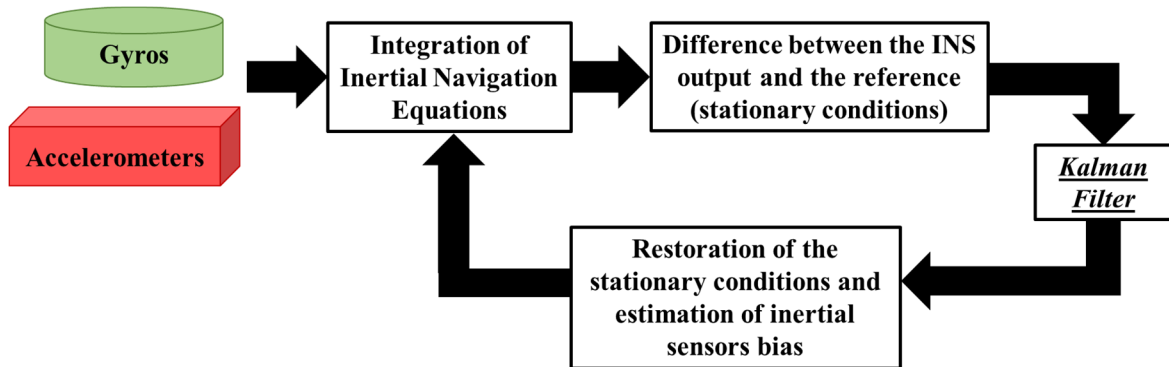


Figure 23. ZUPT filter block diagram model.

The full 15-dimension augmented state error vector for the ZUPT filter is:

$$\delta x(t) = [\delta \vec{r}, \delta \vec{V}, \vec{\varepsilon}, \delta \vec{f}, \delta \vec{\omega}]^T \quad (8)$$

where:

- $\delta \vec{r}$  is the position error;
- $\delta \vec{V}$  is the velocity error;
- $\vec{\varepsilon}$  is the attitude error;
- $\delta \vec{f}$  is the acceleration error;

- $\delta\vec{\omega}$  is the angular rate error

The accelerometers error  $\delta\vec{f}$  is:

$$\delta\vec{f} = \vec{b}_a + \vec{\eta}_a \quad (9)$$

where  $\vec{\eta}_a$  is the accelerometer measurement noise, which is modeled as a zero-mean Gaussian noise, and  $\vec{b}_a = [b_{ax}, b_{ay}, b_{az}]$  is the accelerometer bias. In the standard ZUPT filter, the time model for the accelerometer bias is assumed as:

$$\dot{\vec{b}}_a(t) = \vec{\eta}_{ba}(t) \quad (10)$$

where  $\vec{\eta}_{ba}(t)$  is a zero-mean Gaussian noise.

The gyroscopes error  $\delta\vec{\omega}$  is:

$$\delta\vec{\omega} = \vec{b}_g + \vec{\eta}_g \quad (11)$$

where  $\vec{\eta}_g$  is the gyro measurement noise, which is modeled as a zero-mean Gaussian noise, and  $\vec{b}_g = [b_{gx}, b_{gy}, b_{gz}]$  is the gyro bias. In the standard ZUPT, the time model for the gyro bias is assumed as:

$$\dot{\vec{b}}_g(t) = \vec{\eta}_{bg}(t) \quad (12)$$

where  $\vec{\eta}_{bg}(t)$  is a zero-mean Gaussian noise.

With the above definitions, the following time-continuous error model is derived:

$$\delta\dot{x}(t) = F(t)\delta x(t) + G(t)\eta(t) \quad (13)$$

where  $\eta(t)$  is the process noise vector:

$$\eta(t) = [\vec{\eta}_a(t), \vec{\eta}_g(t), \vec{\eta}_{ba}(t), \vec{\eta}_{bg}(t)]^T \quad (14)$$

$F(t)$  is the time-dependent process transition matrix and  $G(t)$  is the process noise matrix, defined in (Groves 2013). The state space model for the error dynamic is non-linear since  $F(t)$  and  $G(t)$  contain time-variable component. Consequently, a linearized process is needed to apply the principle of Kalman filter without truly linear dynamics or sensors (Ducatan *et al.* 2011). Linearization is based on the small perturbations hypothesis.

The standard ZUPT works as follows. First of all, the inertial navigation equations are numerically integrated. To initialize:

- the position vector is provided by an external reference device, like a GNSS receiver;
- the velocity components are set to zero (the host vehicle is at rest);
- roll and pitch angles are computed through a coarse levelling based on accelerometers output and the heading angle is provided by an external input;
- inertial sensors bias are set to zero (because they are unknown).

Then, in the prediction step, the state error vector and the covariance matrix  $P_k$  are propagated (Eq. (15) and (16)):

$$\delta x_k^- = \Phi_k \delta x_{k-1} + \eta_k \quad (15)$$

with:

$$\Phi_k \approx I + F(kT_s)T_s \quad (16)$$

where  $I$  is the 15x15 identity matrix,  $T_s$  is the sample period,  $\eta_k$  is the discrete-time process noise.

$$P_k^- = \Phi_k P_{k-1} \Phi_k^T + \Gamma_k \quad (17)$$

with:

$$\Gamma_k = (G_k Q_k G_k^T) T_s \quad (18)$$

where  $T_s$  is the sample period,  $G_k$  is the process noise discretized matrix and  $Q_k$  is the 12x12 covariance matrix of the process noise, whose elements will be defined in the next section. Subsequently, the Kalman gain matrix can be evaluated:

$$K_k = P_k^- H_k^T (H_k P_k^- H_k^T + R_k)^{-1} \quad (19)$$

where  $H_k$  is the 9x9 identity matrix and  $R_k$  is the measurement noise matrix.  $R_k$  is a 9x9 diagonal matrix, whose elements reflects the uncertainty in the initial state vector evaluation. Hence the error covariance matrix can be updated according to:

$$P_k = (I - K_k H_k) P_k^- \quad (20)$$

and the state error vector can be updated as:

$$\delta x_k = K_k v_k \quad (21)$$

where  $v_k$  is the measurement innovation computed as the difference between the initial state vector and the current estimated state vector. Due to uncompensated inertial sensors bias, the updated system state is different from the previous one. Hence, every second a state correction is executed. The final step of the ZUPT is to update the state vector and estimate the inertial sensors bias.

It is worth noting that the standard ZUPT filter needs calibrated gyro data as input. This is particularly important for MEMS gyros, which are characterized by high levels of noise and poor bias stability characteristics (Tang *et al.* 2014; Xia *et al.* 2009). The block diagram model is presented in Figure 24. In the ZUPT algorithm, the filtering step is preceded by thermal calibration of raw gyro data.

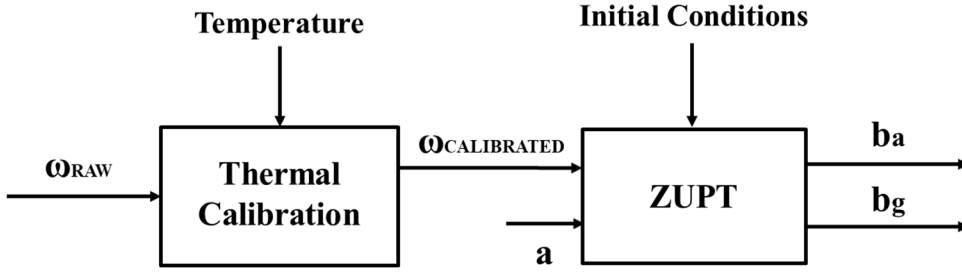


Figure 24. Standard ZUPT filter:  $a$  is the accelerometer output,  $\omega_{RAW}$  is the raw gyro data,  $\omega_{CALIBRATED}$  is the calibrated gyro data and  $b_a$  and  $b_g$  are respectively the accelerometer and gyro bias.

#### 4.2.2.2.2. Determination of process noise terms

To realize an accurate filter, it is necessary to correctly define the elements of the covariance matrix of the process noise  $Q_k$ , which are defined as follows (Groves 2013):

- $Q_k(1,1), Q_k(2,2), Q_k(3,3)$  are related to the accelerometer measurement noise  $\eta_a$ .

$$Q_k(1,1) = Q_k(2,2) = Q_k(3,3) = \sigma_{VRW}^2 \quad (22)$$

where  $\sigma_{VRW}$  is the velocity random walk of the accelerometer measurement.

- $Q_k(4,4), Q_k(5,5), Q_k(6,6)$  are related to the gyro measurement noise  $\eta_g$ .

$$Q_k(4,4) = Q_k(5,5) = Q_k(6,6) = \sigma_{ARW}^2 \quad (23)$$

where  $\sigma_{ARW}$  is the angular random walk of the gyro measurement.

- $Q_k(7,7), Q_k(8,8), Q_k(9,9)$  are related to the accelerometer bias  $\eta_{ba}$ .

$$Q_k(7,7) = Q_k(8,8) = Q_k(9,9) = \sigma_{ABI}^2 \quad (24)$$

where  $\sigma_{ABI}$  is the bias instability of the accelerometer measurement.

- $Q_k(10,10), Q_k(11,11), Q_k(12,12)$  are related to the gyro bias  $\eta_{bg}$ .

$$Q_k(10,10) = Q_k(11,11) = Q_k(12,12) = \sigma_{GBI}^2 \quad (25)$$

where  $\sigma_{GBI}$  is the bias instability of the gyro measurement.

Since  $Q_k$  is a diagonal matrix, the off-diagonal elements are zero. The diagonal elements of  $Q_k$  have been evaluated through the Allan Variance analysis (Gross *et al.* 2011). The Allan Variance is a simple and efficient method to characterize different stochastic processes and their coefficients, allowing estimation of the accidental component of errors that affect the signal (El-Diasty *et al.* 2007; Zhang *et al.* 2008). The characteristic Allan Variance curve can be obtained through some simple operations on the sensor output and further used to determine the type and magnitude of errors affecting the sensor data (IEEE Standards Coordinating Committee 27 on Time and Frequency 2009). If  $N$  is the number of samples from an inertial sensor with a sample time  $\tau_0$ , a group of  $\nu$  data points can be created (with  $\nu < N/2$ ); each group member is called a cluster  $\tau$  with size  $\nu\tau_0$ . If  $\Omega(t)$  is the instantaneous output of the sensor, its integration (e.g., for the gyro output) is the angle  $\theta(t)$  (de Pasquale & Somà 2010):

$$\theta(t) = \int \Omega(t) dt \quad (26)$$

The angle is measured at discrete times given by  $t = k\tau_0$  (for  $k = 1, 2, 3, \dots, N$ ). By using the notation  $\theta(t) = \theta(k\tau_0) = \theta_k$ , the average angle between the times  $k\tau_0$  and  $(k\tau_0 + \tau)$  is given by (de Pasquale & Somà 2010):

$$\bar{\theta}_k(\tau) = \frac{1}{\tau} \int_{k\tau_0}^{k\tau_0 + \tau} \Omega(t) dt, \quad \tau = \nu\tau_0 \quad (27)$$

The Allan Variance, estimated from a finite number of samples, is defined as follows (de Pasquale & Somà 2010):

$$\sigma^2(\tau) = \frac{1}{2\tau^2(N-2\nu)} \sum_{\nu=1}^{N-2\nu} (\theta_{k+2\nu} - 2\theta_{k+\nu} + \theta_k)^2 \quad (28)$$

The most attractive feature of this method is the ability to define various error components by the slope of the root Allan Variance (i.e., the Allan deviation) plot. Typical errors affecting inertial sensors, which are detectable through the Allan Variance, are the quantization noise, angle random walk, correlated noise, sinusoidal noise, bias instability, rate random walk, and rate ramp. Correlated and sinusoidal noises have minor contributions to the total noise, and they appear only at long-time clusters. All the other errors are believed to have the most impact on MEMS sensors (Fong *et al.* 2008).

### 4.2.3. Contribution of this thesis

This thesis proposes two innovative solutions to overcome the limitations of the traditional bias estimation and calibration approach. The first solution, proposed in Section 4.2.3.1, consists in adopting Back-Propagation Neural Networks (BPNNs) to overcome the limitations of the traditional polynomial fitting in mapping the non-linear MEMS gyro bias trend with temperature (Fontanella *et al.* 2018b). Indeed, BPNNs guarantee better performance than the traditional fitting method (Fontanella *et al.* 2016, 2017a), since they are self-adaptive in constructing a mathematical model after several repetitive learning and testing phases. To compare the effectiveness of BPNNs and polynomial fitting, the effects of these two calibration methods on the determination of flight attitude will be considered in Section 4.2.5.

The second solution is the innovative Thermal Compensated ZUPT (TCZUPT) filter that unifies the two steps of thermal compensation and filtering (Fontanella *et al.* 2018a). It is presented in Section 4.2.3.2. The calibration transfer function is exploited within the Kalman filter, with the aim of embedding the compensation of thermal effect on bias in the filter itself. Therefore, no calibration pre-processing stage is required. This allows the reduction of the computational burden of the IMU processing software and improves its accuracy, reliability, and maintainability. An important advantage over the traditional approach can be appreciated when the gyro bias is affected by hysteresis. As the traditional approach adopts the transfer function as a fixed reference, the presence of hysteresis causes an additive bias. On the contrary, the proposed approach exploits the derivative of the

calibration transfer function with temperature. This term tends to be constant on the different branches that form the hysteresis loop (Gulmammadov 2009). The comparative performance analysis of the ZUPT filter and the TCZUPT filter is presented in Section 4.2.6.

#### **4.2.3.1. Bias drift modelling through Back-Propagation Neural Networks**

BPNNs are composed by multi-layers in the one-way transmission (Xia *et al.* 2009). Each layer consists of processing units, called neurons, which receive their input from units of the previous layer and send their output to units in the successive layer. BPNNs are composed by an input layer, that simply accepts the individual components of the input vector and distributes them, without modification, to all of the units of the second layer, a certain number of hidden layers, where data processing is performed, and an output layer that produces the network's approximation of the correct output vector (Hecht-Nielsen 1992). The errors of the units in the hidden layers are determined by back-propagating the errors of the units in the output layer. For this reason, the method is called back-propagation learning rule (Zhang *et al.* 2009).

Through the application of BPNNs, it is possible to determine the corresponding relationship between the given input-output sample pairs, which is memorized as connecting weight values in the network. After being weighted and transformed by a transfer function, data are passed to units in the successive layer, if a threshold value is exceeded. The Sigmoid activation functions (tan-Sigmoid, log-Sigmoid and linear-Sigmoid) are usually adopted as transfer functions for hidden layers to introduce non-linearity in the model, whereas the linear function is regularly used as the transfer function for the output layer (Xia *et al.* 2009). BPNNs have several advantages (Fontanella *et al.* 2018b):

- The local residuals can be reduced by properly increasing the number of neurons;
- They have well defined training strategies that can be easily adapted to the bias thermal drift behaviour of all types of MEMS gyros;
- They have the advantages of non-linear fitting, regardless of the mathematical model of the sensor and various non-linear factors (Xia *et al.* 2009);
- The computational load of BPNN is fully compatible with the high rate processing of gyro output, if a limited number of neurons is adopted.

The proposed tool has been developed by using the MATLAB<sup>TM</sup> Neural Network toolbox. The tool helps to assess the best Neural Network structure that can model the bias

evolution versus temperature for each specific gyro. In fact, each gyro has its own bias drift with temperature, which is different from other gyros.

Several algorithms can be used to train the network, but the Levenberg-Marquardt algorithm is the fastest (Wilamowski & Yu 2010). It is an iterative three-step process including training, validating, and testing. This algorithm needs to share the dataset among three different uniformly distributed subsets. In our application, 65% of samples are used for training, 20% of samples for validating and 15% of samples for testing. Figure 25 presents the flow chart of the training process.

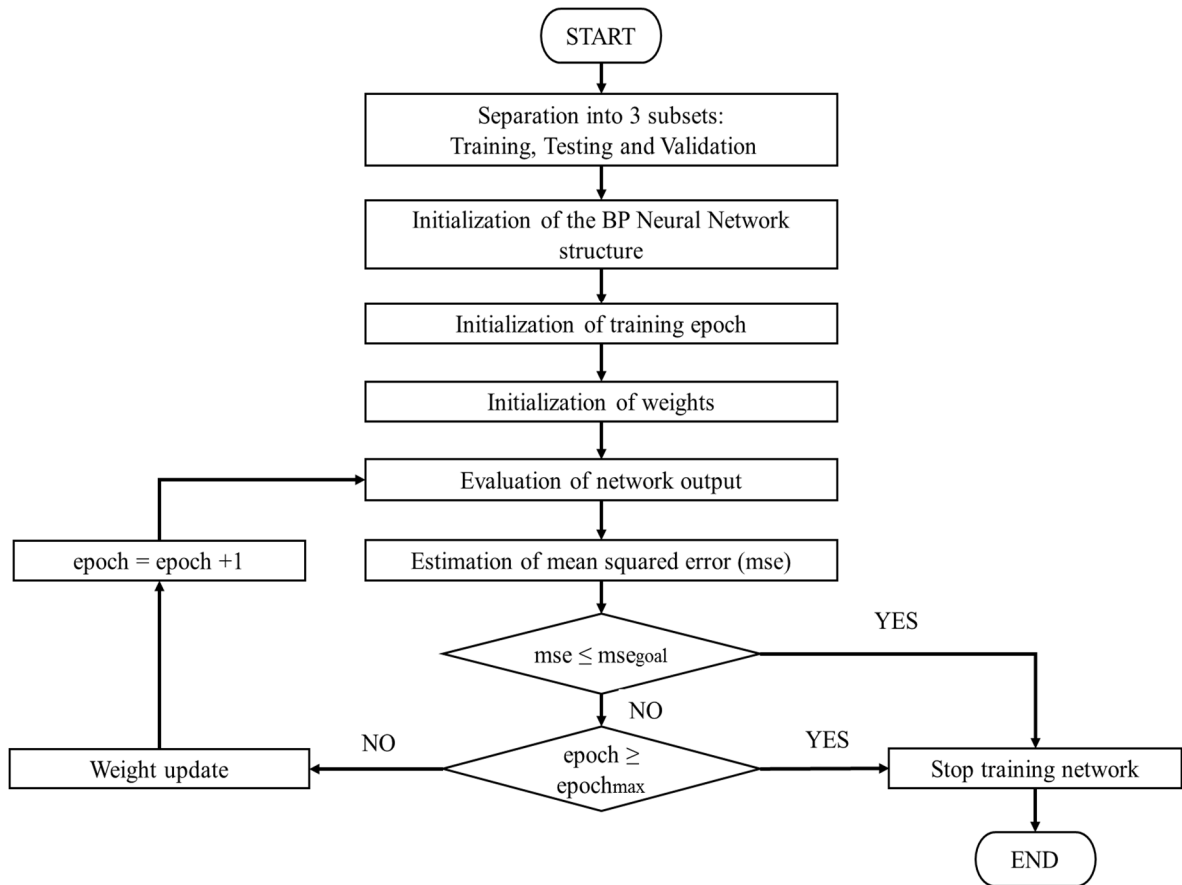


Figure 25. Flow chart of the Back Propagation Neural Network training process.

#### 4.2.3.2. *Thermal Compensated ZUPT filter*

The TCZUPT filter has been developed to overcome the limitations of the traditional ZUPT filter. It needs raw gyro data as input by unifying the two steps of thermal calibration and filtering (Figure 26).

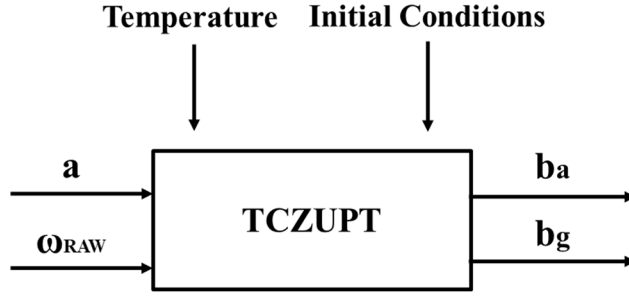


Figure 26. TCZUPT filter:  $\mathbf{a}$  is the accelerometer output,  $\omega_{\text{RAW}}$  is the raw gyro data and  $\mathbf{b}_a$  and  $\mathbf{b}_g$  are respectively the accelerometer and gyro bias.

The proposed method assumes a different bias drift model with respect to the standard ZUPT filter, in which it is modelled as a zero-mean Gaussian noise (Eq. (12)). In the TCZUPT filter, instead, it is modelled as the combination of two terms, i.e. a temperature dependent component and a stochastic component:

$$\dot{\vec{b}}_{g\text{TCZUPT}}(t) = \frac{d\vec{b}_g(T(t))}{dt} + \vec{\eta}'_{bg}(t) \quad (29)$$

where  $\vec{\eta}'_{bg}(t)$  is the stochastic component, modelled as a zero-mean Gaussian noise ( $\vec{\eta}'_{bg}(t) < \vec{\eta}_{bg}(t)$  of Eq. (12)) and  $\frac{d\vec{b}_g(T(t))}{dt}$  is the temperature dependent component, defined as follows:

$$\frac{d\vec{b}_g(T(t))}{dt} = \frac{\partial \vec{b}_g}{\partial T} \cdot \frac{dT}{dt} \quad (30)$$

where  $\frac{\partial \vec{b}_g}{\partial T}$  is the partial derivative of gyro bias with respect to temperature and  $\frac{dT}{dt}$  is the time derivative of temperature. These two terms can be obtained as follows:

- BPNNs are used to estimate the derivative of gyro bias with respect to temperature.
- The algorithm proposed in (Weiss, Neil A. 2001) is used to evaluate the time derivative of temperature data obtained by the temperature sensor inside the AHRS.

In every time-point, it takes into account the time-history of the derivative.

Therefore, in the TCZUPT filter, the gyro bias propagation in the prediction step is:

$$\mathbf{b}_{g,k}^- = (I_{3 \times 3} + F_{g,k} \cdot T_s) \cdot \mathbf{b}_{g,k-1} + \frac{db_{g,k}}{dt_k} \cdot T_s \quad (31)$$

where  $I_{3 \times 3}$  is the  $3 \times 3$  identity matrix,  $F_{g,k}$  is the  $3 \times 3$  process transition matrix for gyro bias,  $T_s$  is the sample period,  $\frac{db_{g,k}}{dt_k}$  is the discrete-time derivative of gyro bias. In conclusion, the TCZUPT filter requires a simplified configuration with respect to the standard ZUPT filter, which needs two processing phases, one for thermal calibration and the other for filtering.

#### 4.2.4. Experimental tests

The standard and innovative methods have been tested on the Attitude and Heading Reference System or AHRS Axitude AX1-[ ]<sup>TM</sup>, developed by the italian Company GMA S.r.l.<sup>TM</sup>, which is depicted in Figure 27. This device is composed by the following sensors (GMA 2018):

- Triaxial accelerometer sensor;
- Triaxial gyroscope sensor;
- Triaxial magnetometer sensor;
- Temperature sensor.

The adopted gyroscopes are the CRS05-02<sup>TM</sup> by Silicon Sensing<sup>TM</sup> (Plymouth, UK) while the adopted accelerometers are the MS8010<sup>TM</sup> by Colybris<sup>TM</sup> (Yverdon-les-Bains, Switzerland). In the standard ZUPT filter, the values in Table 3 and Table 4 have been used to define the elements of the covariance matrix of the process noise (Eq. (22)-(25)). In the TCZUPT filter, instead, a different value of the gyro bias instability  $\sigma_{GBI}$  has been used. Indeed, the TCZUPT filter receives as input raw gyro data, which have a higher bias instability than the calibrated data used in the standard ZUPT filter. The accelerometer and gyro error components for the TCZUPT filter are presented in Table 5 and Table 6. It is worth noting that the velocity random walk  $\sigma_{VRW}$  and accelerometer bias instability  $\sigma_{ABI}$  are the same of the standard ZUPT filter, as well as the gyro angular random walk  $\sigma_{ARW}$ .



Figure 27. Axitude AX1-[ ]<sup>TM</sup>.

Table 3. Angular random walk  $\sigma_{ARW}$  and gyro bias instability  $\sigma_{GBI}$  (ZUPT filter).

<b>CRS05-02™ Gyro by Silicon Sensing™</b>	
$\sigma_{ARW}$	$\sigma_{GBI}$
3.18 degree/ $\sqrt{h}$	$1.5 \times 10^{-4}$ degree/s

Table 4. Velocity random walk  $\sigma_{VRW}$  and accelerometer bias instability  $\sigma_{ABI}$  (ZUPT filter).

<b>MS8010™ Accelerometer by Colybris™</b>	
$\sigma_{VRW}$	$\sigma_{ABI}$
0.05 m/(s $\sqrt{h}$ )	2 m/(sh)

Table 5. Angular random walk  $\sigma_{ARW}$  and gyro bias instability  $\sigma_{GBI}$  (TCZUPT filter).

<b>CRS05-02™ Gyro by Silicon Sensing™</b>	
$\sigma_{ARW}$	$\sigma_{GBI}$
3.18 degree/ $\sqrt{h}$	$5 \times 10^{-4}$ degree/s

Table 6. Velocity random walk  $\sigma_{VRW}$  and accelerometer bias instability  $\sigma_{ABI}$  (TCZUPT filter).

<b>MS8010™ Accelerometer by Colybris™</b>	
$\sigma_{VRW}$	$\sigma_{ABI}$
0.05 m/(s $\sqrt{h}$ )	2 m/(sh)

Two thermal tests have been performed to determine MEMS gyro bias under different temperature points. These tests have been carried out in the laboratory of the GMA S.r.l.™, located in Giugliano in Campania (Italy). Figure 28 presents the setup equipment used to perform thermal tests:

- A climatic chamber Heraus-HT7057, which has a nominal temperature range of -70°C/+180°C;
- A power supply for the AHRS (24-28 V);

- A personal computer with a RS-232 interface connected to the AHRS and the climatic chamber;
- A software data logger that communicates with the AHRS through the serial interface 232, using a Baud Rate of 115200 bps;
- Two external temperature sensors, one attached to the device, the other attached to the inner wall of the climatic chamber. These supplementary sensors are used to control temperature variations during the tests;
- A data acquisition/switch unit connected to another PC to acquire measurements from the two supplementary sensors.

The inertial unit is installed inside the climatic chamber in stationary conditions. This chamber allows for performing controlled thermal solicitations on the unit by assigning proper temperature profiles. Two thermal tests have been performed:

- The first is a soak test, where gyro temperature varies from  $-20.53^{\circ}\text{C}$  to  $37.30^{\circ}\text{C}$ , with steps of  $5^{\circ}\text{C}$ . In this test, the gyro temperature is continuously stabilized at certain temperature points (Niu *et al.* 2013). Figure 29 shows the output trend with temperature.
- The second is a ramp test, where gyro temperature varies from  $27.28^{\circ}\text{C}$  to  $34.08^{\circ}\text{C}$ . In this test, the temperature of the thermal chamber is continuously linearly increased or decreased, without stabilizing the gyro temperature at certain temperature points (Niu *et al.* 2013). The ramp rate is  $2^{\circ}\text{C}$  per minute. These are typical operating conditions for the AHRS Axitude Ax1-[], which is generally used for aeronautical applications. Figure 30 shows the output trend with temperature, for the ramp test.

The AHRS sensor data are transmitted as packages of data on a fixed binary format over a RS232 serial communication interface (GMA 2018). In this process, temperature is the reference environmental term considered. Temperature and static gyro output are measured in real-time to observe the bias drift phenomenon when temperature variations are commanded. It is worth noting that both data sets have been filtered by using the low-pass filter usually adopted in avionic certified AHRS versions to remove out of band noise. It is a second order linear filter with cutoff frequency of 30 Hz. Data obtained from the soak test (presented in Figure 29) are used to build MEMS gyro's bias thermal model over a large

temperature range. Instead, data obtained from the ramp test (presented in Figure 30) are used to test the calibration algorithms in typical operating conditions.

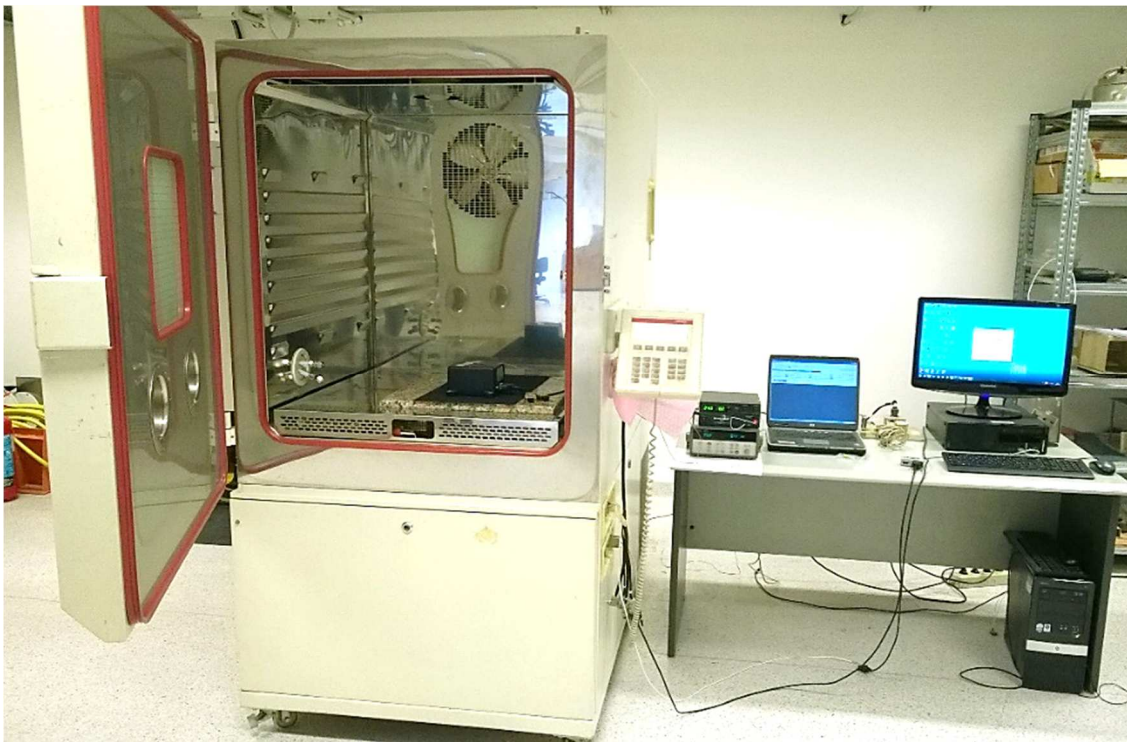


Figure 28. Setup equipment.

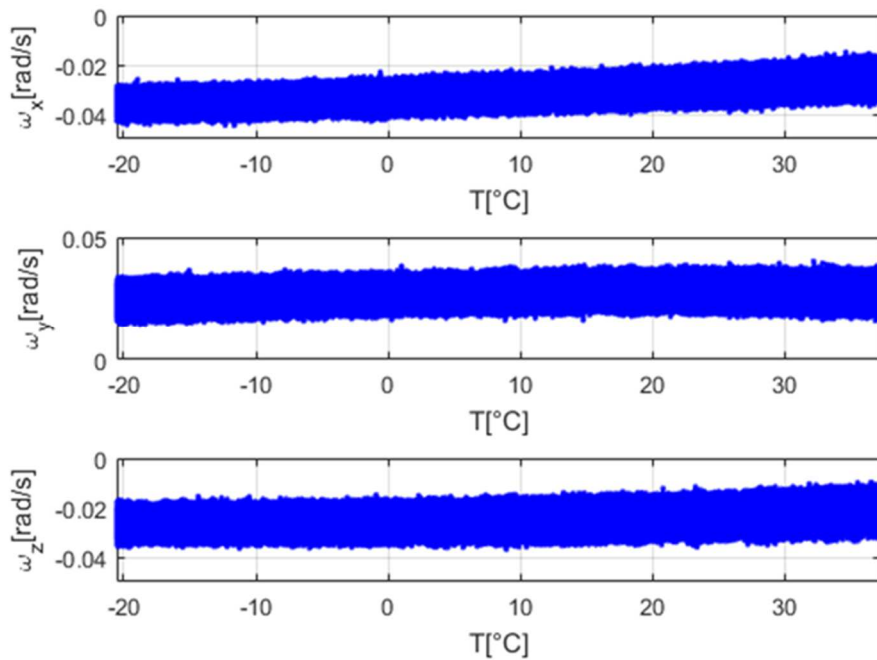


Figure 29. Gyro output ( $\omega_x$ ,  $\omega_y$ ,  $\omega_z$ ) vs. temperature for the soak test.

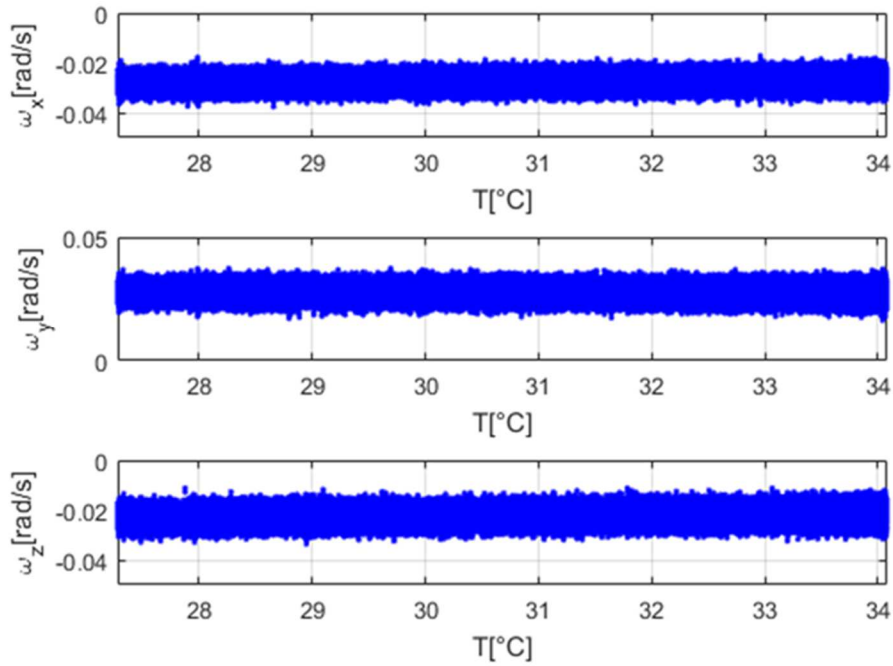


Figure 30. Gyro output ( $\omega_x$ ,  $\omega_y$ ,  $\omega_z$ ) vs. temperature for the ramp test.

## 4.2.5. Comparison of polynomial and BPNNs thermal calibration

### 4.2.5.1. Polynomial order selection

Polynomials of different degrees can be used to develop the bias drift model. However, it is necessary to perform a trade-off between processing loads and effects of residual errors in the system. Indeed, as the order of the polynomial increases, the accuracy of the estimation builds up. However, also the processing load will increase (Günhan & Ünsal 2014).

In our application, the polynomial order for which the performance parameter  $Sr_{PF}$ , defined in Eq. (32), reaches a minimum or when there is no significant decrease in its value with the increase of the polynomial order has been selected (Fontanella *et al.* 2017a).

$$Sr_{PF}(m) = \sqrt{res(m)_1^2 + res(m)_2^2 + res(m)_3^2} \quad (32)$$

where  $res(m)_1$ ,  $res(m)_2$  and  $res(m)_3$  are the residuals for the triaxial gyroscope sensor, for the generic  $m^{th}$  polynomial order. The result of this analysis is presented in Figure 31. A 2<sup>nd</sup> order polynomial can provide a satisfactory convergence effect while simultaneously speeding up the training procedure.

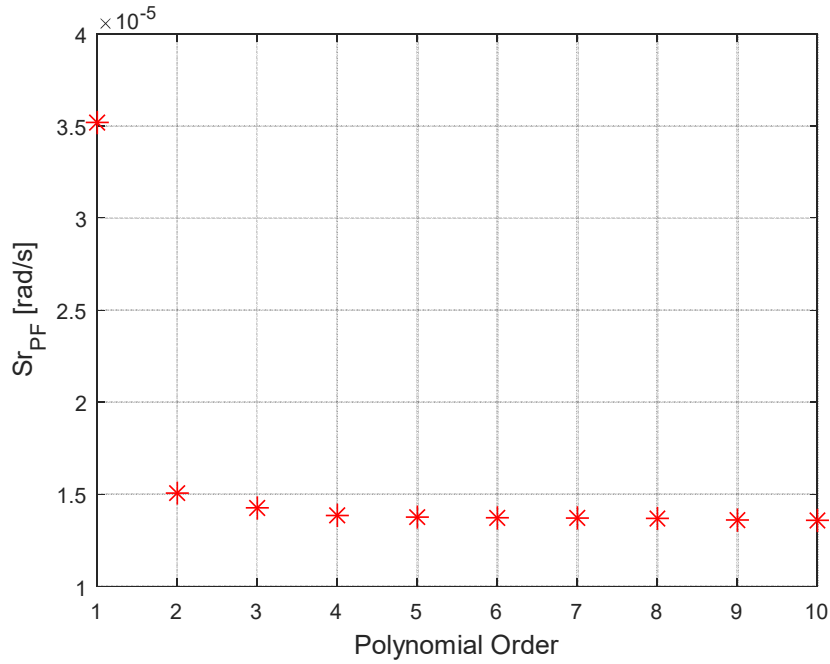


Figure 31. Polynomial fitting performance parameter  $Sr_{PF}$  vs. polynomial order.

#### 4.2.5.2. BPNNs structure selection

To select the most suitable Neural Network structure, it is necessary to consider the Kolmogorov theorem and the relevant discussion presented in (Hecht-Nielsen 1992). According to this theorem, any  $L_2$  function from  $[0, 1]^n$  to  $\mathbb{R}^m$ , where  $[0, 1]^n$  is the closed unit cube in a  $n$ -dimensional Euclidean space and  $\mathbb{R}^m$  is the  $m$ -dimensional Euclidean space, can be implemented to any desired degree of accuracy with a three layers BPNN. However, at least a four layers BPNN is needed in practical applications. The space  $L_2$  includes every typical function that can be experienced in practical problems. For example, it includes the continuous functions and all discontinuous functions that are piecewise continuous on a finite number of subsets of  $[0, 1]^n$  (Hecht-Nielsen 1992).

In this particular application, a four layers BPNN has been adopted. The same number of processing neurons  $n$  has been selected for the hidden layers, since this is the minimum condition for proper use of the network. As for the polynomial order, the optimal number of hidden layer neurons has been chosen through considerations on the performance parameter  $Sr_{NN}$ , defined as:

$$Sr_{NN}(n) = \sqrt{res(n)_1^2 + res(n)_2^2 + res(n)_3^2} \quad (33)$$

$res(n)_1, res(n)_2$  and  $res(n)_3$  are the residuals for the triaxial gyroscope sensor, for a generic BPNN composed by two  $n$ -neurons hidden layers. Also in this case, the optimal number of neurons per hidden layer is that associated with the minimum value of  $Sr_{NN}$  or when no significant reduction is experienced for higher number of neurons (Fontanella *et al.* 2017a). The evolution of the performance parameter  $Sr_{NN}$  versus the number of the hidden layers neurons is shown in Figure 32. In our application, two hidden layers with two neurons each have been chosen, which can provide a satisfactory convergence effect while simultaneously speeding up the training procedure.

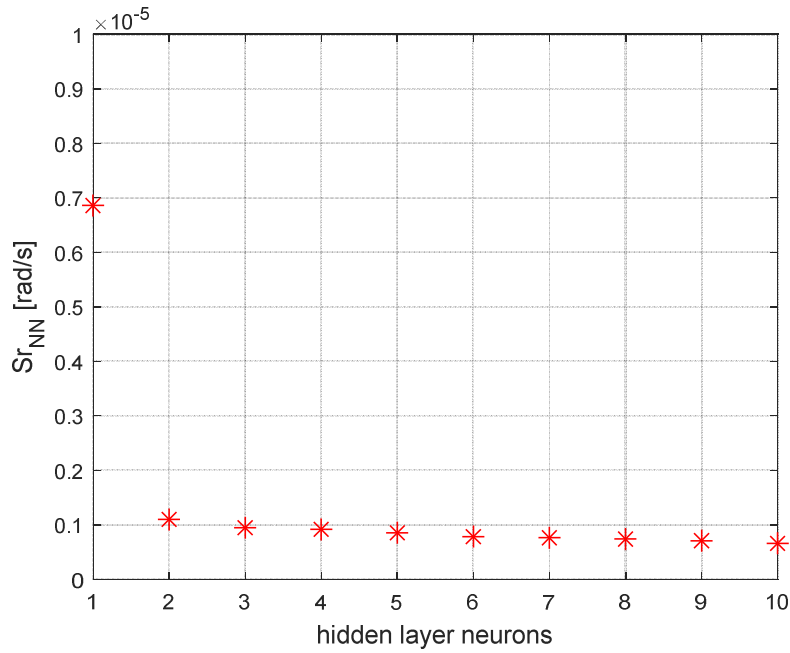


Figure 32. Neural Network performance parameter  $Sr_{NN}$  vs. number of hidden layers neurons.

The resulting configuration is shown in Figure 33 where  $W_i$  ( $i = 1, 2$ ) are the weight values connecting the input layer and the first hidden layer,  $W'_{ij}$  ( $i, j = 1, 2$ ) are the weight values connecting the first hidden layer and the second hidden layer,  $V_i$  ( $i = 1, 2$ ) are the weight values connecting the second hidden layer and the output layer,  $b_{i,j}$  ( $i = 1, 2; j = 1, 2$ ) are the threshold values of the  $j^{th}$  neuron of the  $i^{th}$  hidden layer,  $f$  is the transfer function tan-Sigmoid and  $F$  is the transfer function linear-Sigmoid.

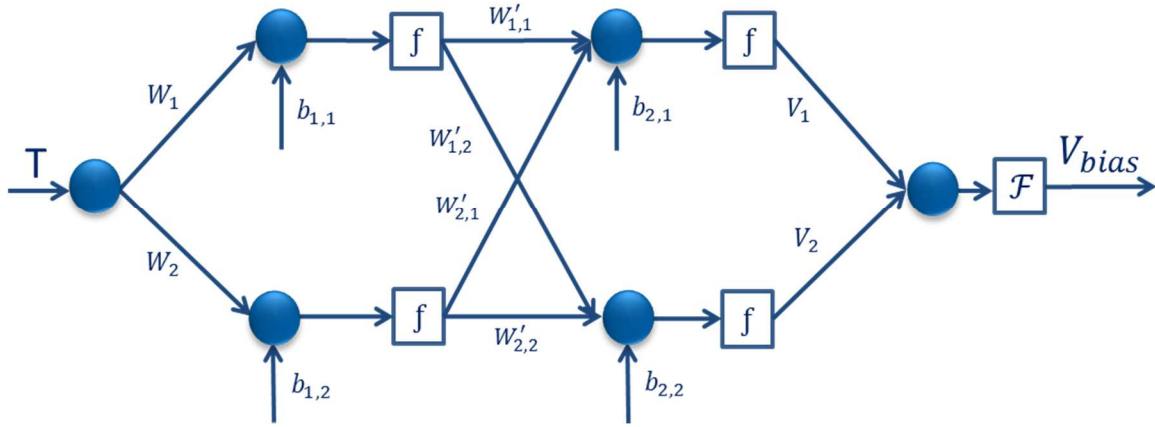


Figure 33. Structure of the BPNN adopted for bias drift modelling.

#### 4.2.5.3. Effect of polynomial and BPNNs calibration on flight attitude

The effect of thermal calibration performed by using polynomial fitting and BPNNs on the determination of flight attitude has been investigated. Results have been compared in correspondence with the temperature points where the difference between the bias drift models developed by using the polynomial fitting and BPNN is maximum and where it reaches its Root Mean Square (RMS) value. In the other cases, the two methods have similar performance. To identify these temperature points, the maximum and RMS values of the parameter  $\Delta\omega$  (Eq. (34)) have been considered.

$$\Delta\omega = \sum_{i=1}^n \sqrt{|Wx_{NN}(i) - Wx_{PF}(i)|^2 + |Wy_{NN}(i) - Wy_{PF}(i)|^2 + |Wz_{NN}(i) - Wz_{PF}(i)|^2} \quad (34)$$

where  $\omega_{xNN}$ ,  $\omega_{yNN}$  and  $\omega_{zNN}$  are the bias drift models developed by using BPNNs, for each axis,  $\omega_{xPF}$ ,  $\omega_{yPF}$  and  $\omega_{zPF}$  are the bias drift models developed by using the polynomial fitting, for each axis, and  $n$  is the number of temperature samples. Figure 34 presents the trend of  $\Delta\omega$  with temperature. Only temperature values from 27.28°C to 34.08°C (i.e., the range of testing data set) have been taken into account. From Figure 34, it is possible to notice that the  $\Delta\omega$  parameter reaches the maximum value ( $\Delta\omega_{MAX} = 1.83 \times 10^{-4}$  rad/s) in correspondence with  $T = 27.78^\circ\text{C}$  and the RMS value ( $\Delta\omega_{RMS} = 1.07 \times 10^{-4}$  rad/s) in correspondence with  $T = 32.60^\circ\text{C}$ .

The aim of this comparison is to evaluate if the calibration based on BPNN determines an advantage in case the INS needs to integrate free-inertial equations when GNSS data is missing, and no aiding information can be provided. To this scope, the quaternion approach has been used; because of its simplicity, mathematical elegance, and lack of singularities, the quaternion representation is a very popular representation for encoding the attitude of a rigid body (Diebel 2006). It is based on Euler's rotational theorem, which states that the relative orientation of two coordinate systems can be described by only one rotation about a fixed axis (Wertz 1978). Therefore, the quaternion is defined by a rotational axis and a rotation angle (Wertz 1978).

$$q = [q_s \ q_x \ q_y \ q_z]^T = \begin{bmatrix} \cos\left(\frac{\theta}{2}\right) \\ \|\vec{e}\| \cdot \sin\left(\frac{\theta}{2}\right) \end{bmatrix} \quad (35)$$

where  $\|\vec{e}\|$  is the normalized rotational axis and  $\theta$  is the rotation angle. Figure 35 and Figure 36 show the trend of the rotation angle  $\theta$  with temperature, whereas Table 7 and Table 8 present the time in which the flight attitude accuracy meets the requirements imposed by (FAA 2012). Being  $t_{NN}$  the time taken by using the BPNNs calibration and  $t_{PF}$  the time taken by using the polynomial fitting calibration,  $\Delta t\%$  is computed according to Eq. (36).

$$\Delta t\% = \frac{t_{NN} - t_{PF}}{t_{PF}} * 100 \quad (36)$$

It is possible to notice that the application of BPNNs allows MEMS gyroscopes to increase the time in which the flight attitude accuracy meets the requirements imposed by (FAA 2012). In conclusion, the application of the BPNNs allows MEMS gyroscopes to obtain an effective improvement in terms of stand-alone attitude determination accuracy to support longer GNSS signal outages.

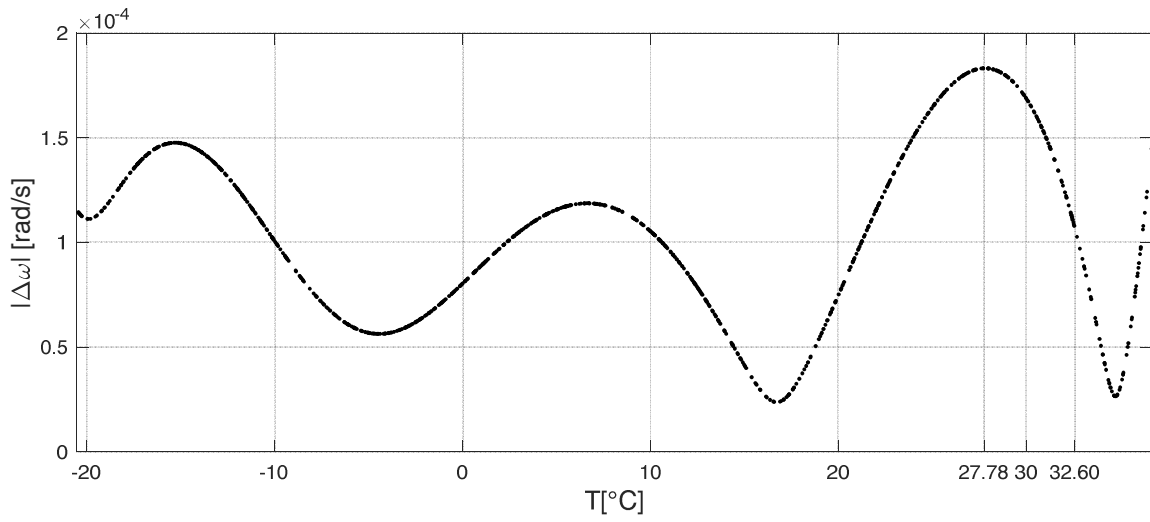


Figure 34. Evolution of  $\Delta\omega$  parameter versus temperature.

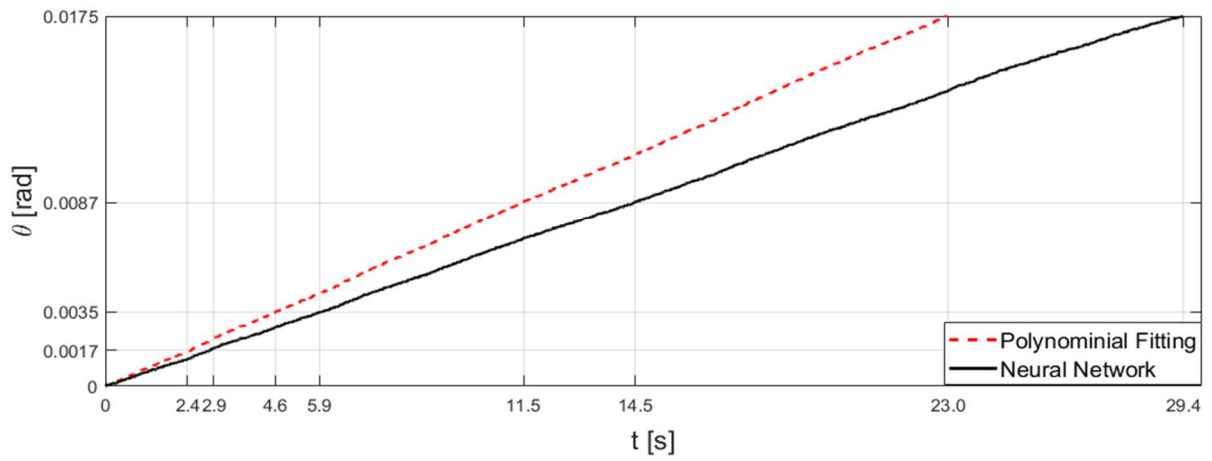


Figure 35. Trend of the rotation angle  $\theta$  with temperature ( $\Delta\omega_{MAX}$ ).

Table 7. Time in which the flight attitude accuracy meets the imposed requirements ( $\Delta\omega_{MAX}$ ).

$\theta$ [rad]	$t_{NN}$ [s]	$t_{PF}$ [s]	$\Delta t\%$
$1.70 \times 10^{-3}$	2.9	2.4	21.8
$3.50 \times 10^{-3}$	5.9	4.6	25.80
$8.70 \times 10^{-3}$	14.5	11.5	26.10
$1.75 \times 10^{-2}$	29.4	23.0	27.38

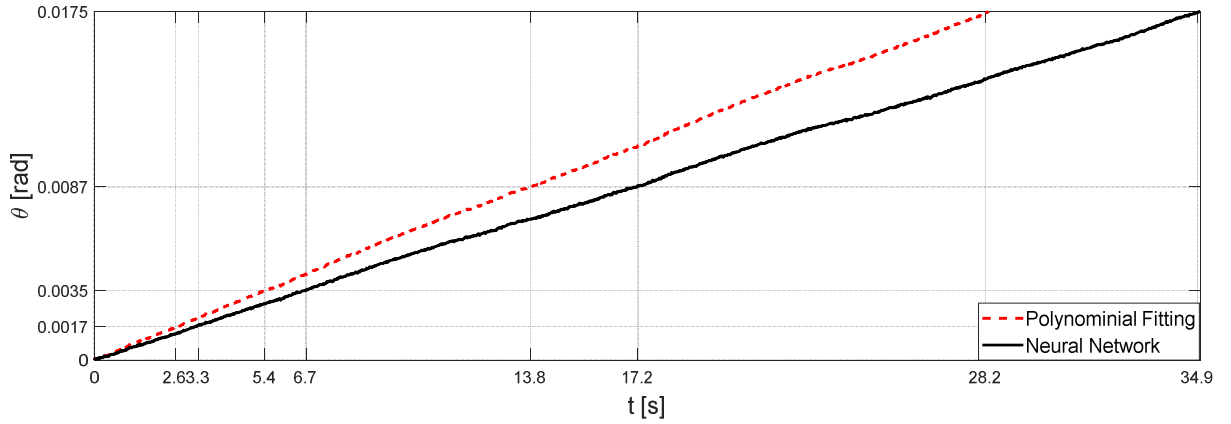


Figure 36. Trend of the rotation angle  $\theta$  with temperature ( $\Delta\omega_{RMS}$ ).

Table 8. Time in which the flight attitude accuracy meets the imposed requirements ( $\Delta\omega_{RMS}$ ).

$\theta$ [rad]	$t_{NN}$ [s]	$t_{PF}$ [s]	$\Delta t\%$
$1.70 \times 10^{-3}$	3.3	2.7	19.27
$3.50 \times 10^{-3}$	6.7	5.4	22.02
$8.70 \times 10^{-3}$	17.2	13.8	25.00
$1.75 \times 10^{-2}$	34.9	28.2	23.76

## 4.2.6. TCZUPT filter implementation and testing

### 4.2.6.1. Derivation of thermal correction function

In the TCZUPT filter, thermal calibration and filtering are simultaneously performed. Therefore, it needs raw gyro data as input. During the execution of the filtering process, BPNNs trained on the derivative of the training data set presented in Figure 29 is used to estimate the derivative with respect to temperature of the testing data set presented in Figure 30. The performance parameter  $Sr_{TCZUPT}$  defined in Eq. (37) has been evaluated in order to select the most suitable number of hidden layer neurons.

$$Sr_{TCZUPT}(dn) = \sqrt{res(dn)_1^2 + res(dn)_2^2 + res(dn)_3^2} \quad (37)$$

In Eq. (37)  $res(dn)_1, res(dn)_2$  and  $res(dn)_3$  are the residuals for the triaxial gyroscope sensor, for a generic BPNN composed by two  $n$ -neurons hidden layers. Also in this case, the optimal number of neurons per hidden layer is that associated with the

minimum value of  $Sr_{TCZUPT}$  or when no significant reduction is experienced for higher number of neurons (Fontanella *et al.* 2017a). The evolution of the performance parameter  $Sr_{TCZUPT}$  versus the number of the hidden layers neurons is shown in Figure 37. Also for the TCZUPT algorithm, two hidden layers with two neurons each have been chosen, which can provide a satisfactory convergence effect while simultaneously speeding up the training procedure. However, it is worth noting that the order of magnitude of  $Sr_{TCZUPT}$  is  $10^{-7}$  rad/s°C, whereas it is  $10^{-5}$  rad/s for  $Sr_{NN}$  defined in Eq. (33).

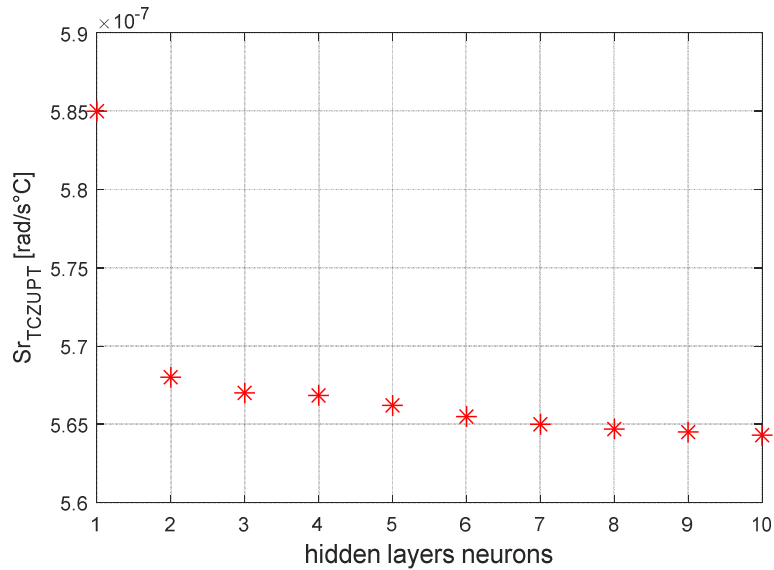


Figure 37. Performance parameter  $Sr_{TCZUPT}$  vs. number of hidden layers neurons (TCZUPT filter).

#### 4.2.6.2. ZUPT & TCZUPT: comparative performance analysis

The input data of the standard ZUPT and TCZUPT filters are respectively shown in Figure 38 and Figure 39. To highlight the different trends of the two data sets, a second order low-pass filter with cutoff frequency of 1 Hz has been used to remove out of band noise in representing data. However, it is worth noting that the standard and innovative filter have been tested on data filtered by using the second order low-pass filter with cutoff frequency of 30 Hz, which is usually adopted in avionic certified AHRS versions. In both cases, before applying the filtering, the initial zeroing procedure has been performed in a time-frame of 60 seconds.

In this application, the benchmark used to compare the standard ZUPT and TCZUPT filters performance is the moving average of raw and calibrated gyro data. This processing step returns an array of local mean values, where each mean is calculated over a sliding

window of 30 seconds across neighbouring elements of the input vector. Table 9 presents the mean of residuals of the moving averages, which can be considered an estimator of the true bias of the system, with an accuracy given by the corresponding residual. The level of residuals is adequate to justify their use as a reference benchmark for the filter.

The standard ZUPT and TCZUPT filters have been tested on the two conditions listed below. Table 10 presents the RMS error of both methods in both the considered testing conditions.

- Nominal condition. Figure 40, Figure 41 and Figure 42 present the comparison of the true bias of the system, computed by the moving averages and the bias estimated by the ZUPT and TCZUPT filters.
- Residual bias after rough initial alignment of 15 degrees/h (Earth's rotation rate). Since the considered gyro is not tactical grade, this residual error is compatible with its performance. Figure 43, Figure 44 and Figure 45 present the comparison of the true bias of the system, estimated by the moving averages and the bias computed by the ZUPT and TCZUPT filters.

Table 9. Mean value of residuals of the moving average.

	Calibrated Gyro Data	Non-Calibrated Gyro Data
<b>x</b>	$1.68 \times 10^{-06}$ rad/s	$9.53 \times 10^{-06}$ rad/s
<b>y</b>	$2.98 \times 10^{-06}$ rad/s	$6.80 \times 10^{-06}$ rad/s
<b>z</b>	$3.43 \times 10^{-06}$ rad/s	$1.03 \times 10^{-05}$ rad/s

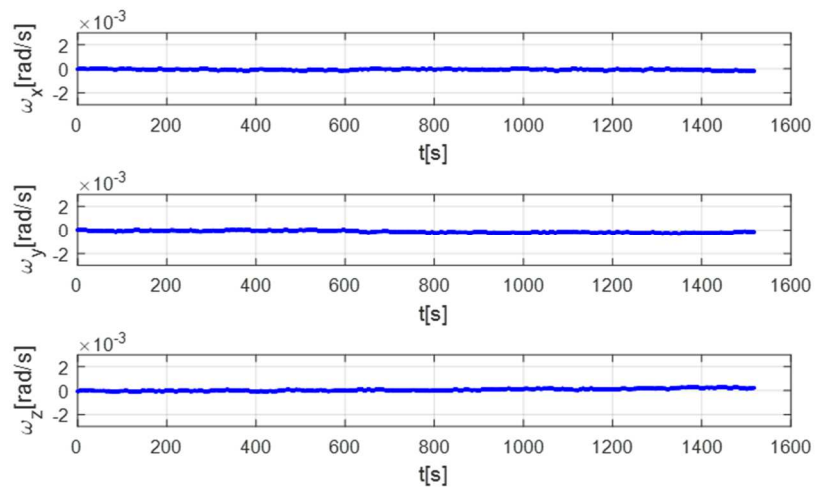


Figure 38. Input data of the standard ZUPT filter.

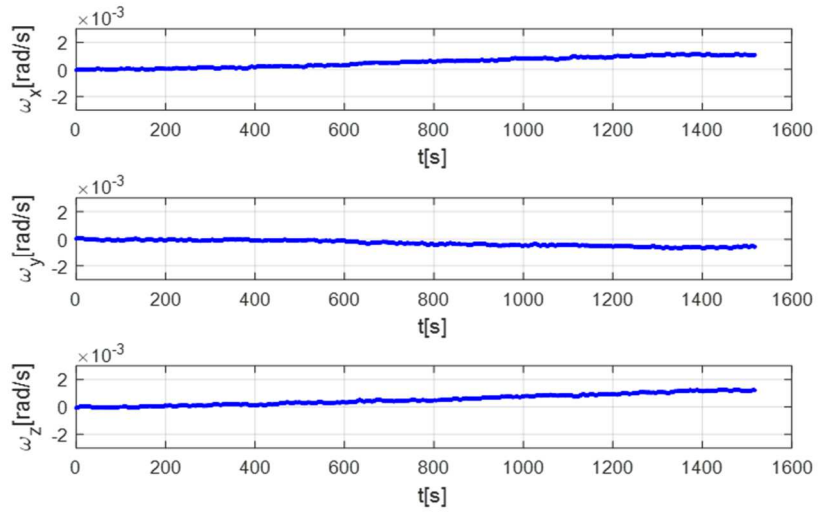


Figure 39. Input data of the TCZUPT filter.

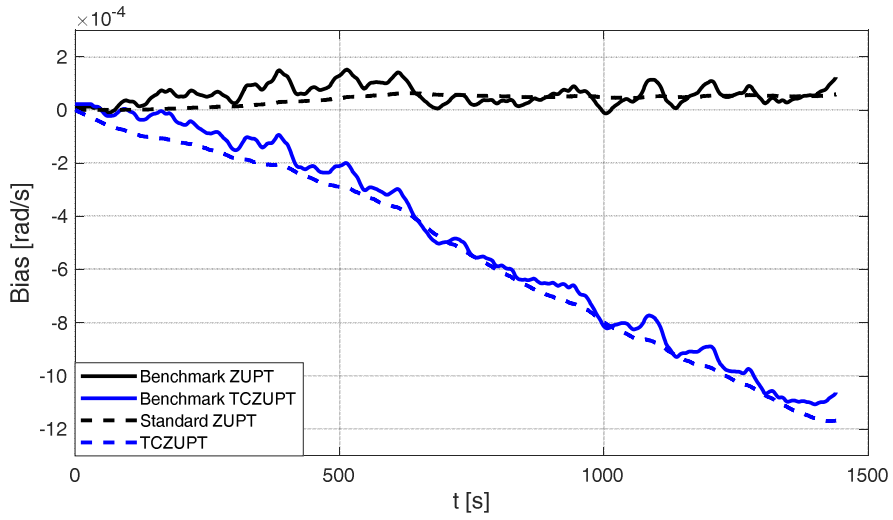


Figure 40. Gyro bias (nominal condition, x-axis).

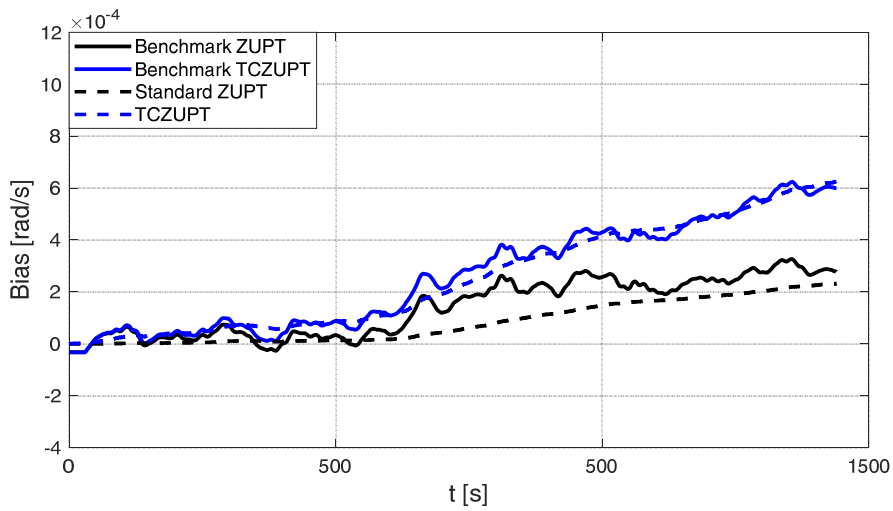


Figure 41. Gyro bias (nominal condition, y-axis).

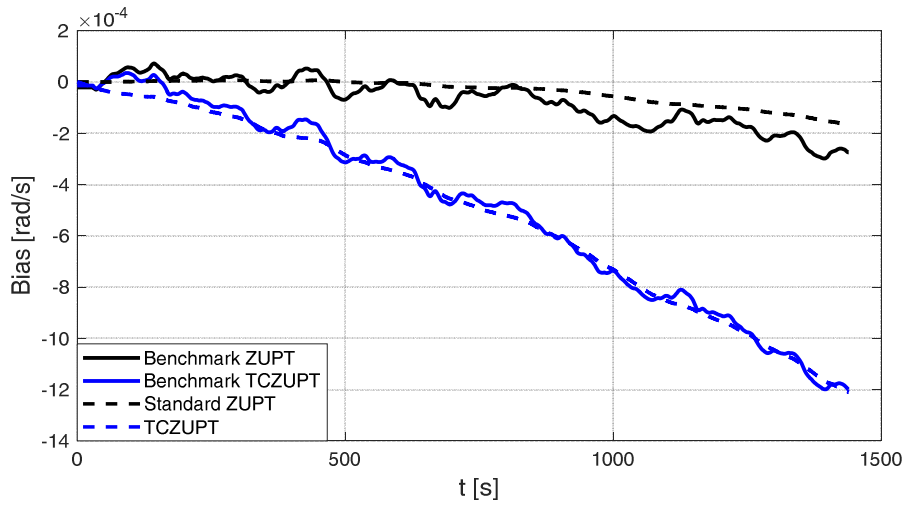


Figure 42. Gyro bias (nominal condition, z-axis).

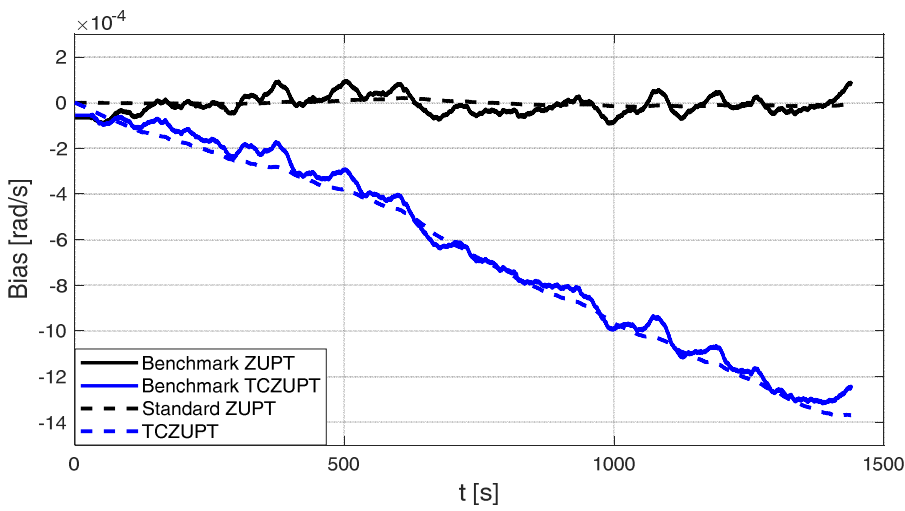


Figure 43. Gyro bias (residual error of 15 degrees/h, x-axis).

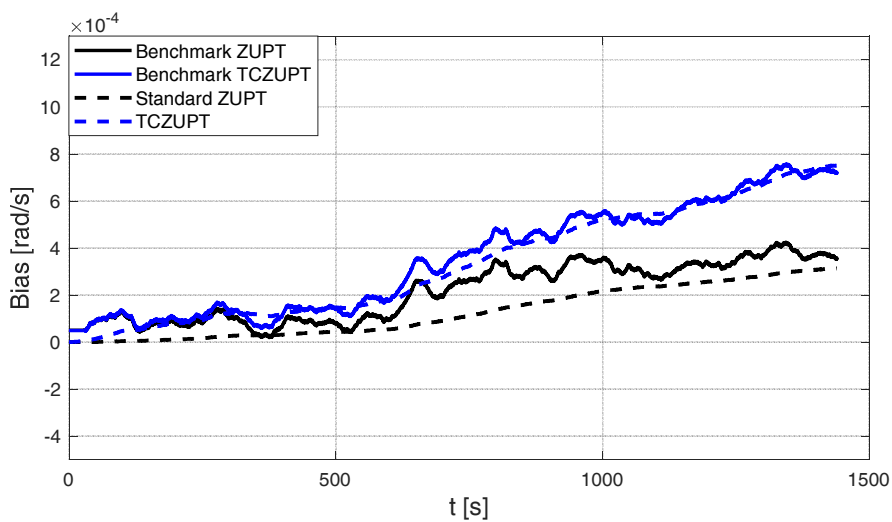


Figure 44. Gyro bias (residual error of 15 degrees/h, y-axis).

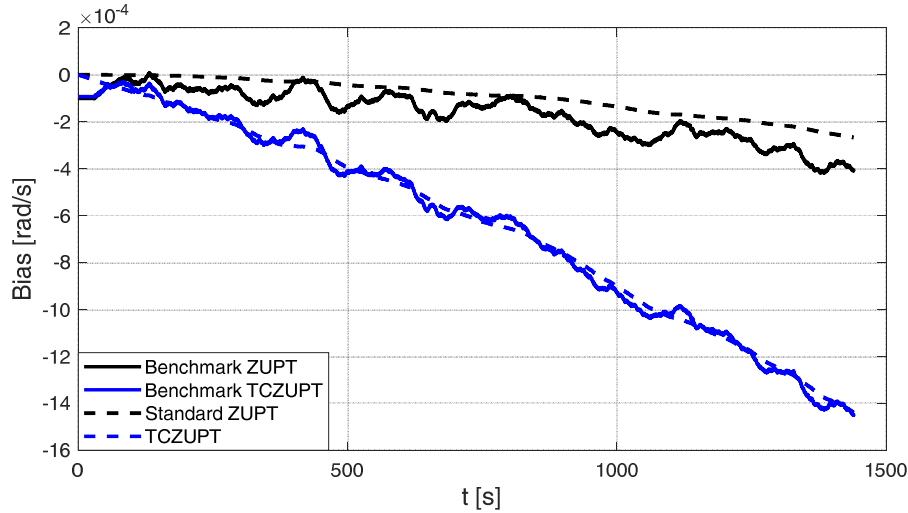


Figure 45. Gyro bias (residual error of 15 degrees/h, z-axis).

It is possible to notice that both in nominal conditions and in the case of a residual initial alignment error of 15 degrees/h the standard ZUPT and TCZUPT filters converge to the true bias of the system. The bias estimated by the standard ZUPT and TCZUPT filters respectively converge to the bias of calibrated gyro output and non-calibrated gyro output. However, in the case of a residual initial alignment error, the TCZUPT filter is faster (Figure 40-Figure 45). Indeed, the TCZUPT filter is not based on direct correction of thermal bias (as the standard ZUPT filter), but on the estimation of the derivative of bias as a function of temperature. Therefore, it is faster in mapping significant bias variations. Table 11 presents the convergence time of the standard ZUPT and TCZUPT filters in case of residual error of 15 degrees/h. A threshold of  $1.00 \times 10^{-05}$  rad/s has been considered in defining the convergence time.

This is an important result for many applications that require a very fast ZUPT process, like missile systems. The TCZUPT filter also presents better performance in the overall interval. This result can be useful in the case of stationary condition for long timeframe, e.g., the aircraft in parking stall for a time longer than the usual in a sunny day. An important advantage of the proposed procedure is that only a single software component is needed to estimate the bias during real-time operation of the unit, i.e., the TCZUPT algorithm. This aspect will reduce the computational burden and improve the accuracy, reliability, and maintainability of the IMU processing software with respect to the standard process that requires that two different components must operate in cascading conditions, such as pointwise calibration software and standard ZUPT filter.

Table 10. RMS error of ZUPT and TCZUPT filters.

<b>Nominal Conditions</b>		
	<b>Standard ZUPT filter</b>	<b>TCZUPT filter</b>
<b>x</b>	$4.15 \times 10^{-05}$ rad/s	$5.33 \times 10^{-05}$ rad/s
<b>y</b>	$7.48 \times 10^{-05}$ rad/s	$2.97 \times 10^{-05}$ rad/s
<b>z</b>	$6.07 \times 10^{-05}$ rad/s	$3.30 \times 10^{-05}$ rad/s
<b>Residual Error of 15 degrees/h</b>		
	<b>Standard ZUPT filter</b>	<b>TCZUPT filter</b>
<b>x</b>	$3.98 \times 10^{-05}$ rad/s	$4.13 \times 10^{-05}$ rad/s
<b>y</b>	$9.72 \times 10^{-05}$ rad/s	$3.88 \times 10^{-05}$ rad/s
<b>z</b>	$8.17 \times 10^{-05}$ rad/s	$3.01 \times 10^{-05}$ rad/s

Table 11. Convergence time of the ZUPT and TCZUPT filters in case of residual error of 15 degree/h.

	<b>Standard ZUPT Filter</b>	<b>TCZUPT Filter</b>
<b>x</b>	140s	65s
<b>y</b>	345s	127s
<b>z</b>	85s	53s

Finally, to assess the statistical significance of the variations between the results for the x, y, and z axes, the testing data set has been divided in 5 data sets corresponding to 5 min of acquisition. Then, the ZUPT and TCZUPT filters have been tested on these data sets. Table 12 shows the mean and standard deviation of the RMS error in nominal conditions, while Table 13 presents the mean and standard deviation of the RMS error in case of a residual initial alignment error of 15 degree/h. ZUPT and TCZUPT filters performance is slightly different for the three axes, since each gyro has different characteristics, even if all of the three gyros are of the same type. However, the small values of the standard deviation indicate that, for each axis, the performance of the ZUPT and TCZUPT filters is fairly stable.

Table 12. Mean and Standard Deviation of the RMS error (nominal conditions, 5 data sets).

	<b>Axis</b>	<b>Mean</b>	<b>Standard Deviation</b>
<b>Standard ZUPT Filter</b>	<i>x</i>	$3.42 \times 10^{-5}$ rad/s	$0.77 \times 10^{-5}$ rad/s
	<i>y</i>	$3.58 \times 10^{-5}$ rad/s	$0.89 \times 10^{-5}$ rad/s
	<i>z</i>	$4.36 \times 10^{-5}$ rad/s	$0.82 \times 10^{-5}$ rad/s
	<b>Axis</b>	<b>Mean</b>	<b>Standard Deviation</b>
<b>TCZUPT Filter</b>	<i>x</i>	$4.70 \times 10^{-5}$ rad/s	$0.61 \times 10^{-5}$ rad/s
	<i>y</i>	$2.63 \times 10^{-5}$ rad/s	$0.65 \times 10^{-5}$ rad/s
	<i>z</i>	$3.89 \times 10^{-5}$ rad/s	$0.70 \times 10^{-5}$ rad/s

Table 13. Mean and Standard Deviation of the RMS error (residual error of 15 degree/h, 5 data sets).

	<b>Axis</b>	<b>Mean</b>	<b>Standard Deviation</b>
<b>Standard ZUPT Filter</b>	<i>x</i>	$6.49 \times 10^{-5}$ rad/s	$0.92 \times 10^{-5}$ rad/s
	<i>y</i>	$8.88 \times 10^{-5}$ rad/s	$0.92 \times 10^{-5}$ rad/s
	<i>z</i>	$7.16 \times 10^{-5}$ rad/s	$0.79 \times 10^{-5}$ rad/s
	<b>Axis</b>	<b>Mean</b>	<b>Standard Deviation</b>
<b>TCZUPT Filter</b>	<i>x</i>	$3.81 \times 10^{-5}$ rad/s	$0.54 \times 10^{-5}$ rad/s
	<i>y</i>	$4.58 \times 10^{-5}$ rad/s	$0.84 \times 10^{-5}$ rad/s
	<i>z</i>	$3.36 \times 10^{-5}$ rad/s	$0.35 \times 10^{-5}$ rad/s

### 4.3. Improving consumer grade MEMS gyros performance by redundancy

#### 4.3.1. Introduction

Last generation consumer grade MEMS gyros have several distinctive features that make their use of interest also for professional navigation applications such as the ones related to attitude determination of advanced small UAS, such as reduced weight, compact configuration, low power consumption and easy integration with electronic boards. Conversely, the overall error is more than an order of magnitude worse than industrial grade sensors (Barbour *et al.* 2011).

However, recent advancements in electronics have reduced the weight, cost, and size of various sensors, thus allowing for multiple sensors to be integrated into many existing systems for various applications (Rhudy *et al.* 2012). By assembling a set of inertial sensors with a certain designed configuration, the redundancy of each axis in the navigation framework can be efficiently improved, as well as the accuracy of the whole IMU. Indeed, the IMU can make full use of the redundant observation data of these sensors, by averaging multiple measurements about the same axis (Cheng *et al.* 2014; Jafari 2015; Wander & Förstner 2013).

This chapter proposes a high-performance and low-cost calibration solution for consumer grade MEMS gyros. It consists in adopting a redundant sensors configuration, i.e. a defined number of sensors placed on the faces of a regular polyhedron. This configuration guarantees a partial self-calibration of typical inertial sensors biases, reducing the uncertainty in attitude determination (Fontanella *et al.* 2018c).

To test the proposed method, the world's densest sensor board, which is the SensorTile™, by ST Microelectronics™ has been adopted. SensorTile™ is a miniaturized tile-shaped development board that includes suitable sensors to remotely sense and measure motion, environmental and acoustical parameters.

### 4.3.2. Exploiting redundancy

The adoption of redundant IMU geometries allows for reducing the level of gyros bias. Indeed, if a redundant configuration composed by  $N$  sensors is realized by placing them with fixed orientation with respect to the IMU internal reference system, the standard deviation of bias in the redundant configuration  $\sigma_{b_{j,r}}$  can be derived as a function of the corresponding value for a single axis gyro  $\sigma_{b_i}$ , as follows:

$$\sigma_{b_{j,r}} = \frac{\sigma_{b_i}}{\sqrt{\sum_{i=1}^N \cos^2 \alpha_{i,j}}} \quad (38)$$

where  $\alpha_{i,j}$  is the angle between the  $i$ -th sensor axis and the  $j$ -th IMU axis. Eq. (38) assumes that angular rate measurement on each IMU axis is determined by averaging the projections of gyros measurements. Eq. (38) can be rewritten as follows:

$$\sigma_{b_j,r} = k_r \cdot \sigma_{b_i} \quad (39)$$

where the term  $k_r$  ( $0 < k_r < 1$ ) represents the fraction of improvement obtained by performing redundant measurements. This term is given as follows:

$$k_r = \frac{1}{\sqrt{\sum_{i=1}^N \cos^2 \alpha_{i,j}}} \quad (40)$$

The best solution to apply redundancy is to place the sensors on the faces of regular polyhedra, i.e. polyhedra that have all faces formed by the same regular polygon. They have the property that the directions that are orthogonal to each face are also uniformly distributed on a sphere. Thus, this configuration guarantees a three-dimensional space uniform error for any direction of IMU axis. Currently, regular polyhedra can be generated only for up to 20 faces, i.e. the icosahedron. In addition, there is the tetrahedron with four faces, the cube with six faces, the octahedron with eight faces, and the dodecahedron with twelve faces.

The simplest configuration to be realized as a prototype is the cubic one. Therefore, a cubic configuration of consumer grades MEMS inertial sensors has been realized and tested. To estimate the improvement determined by redundancy, a proper selection of IMU internal reference system must be performed. In the case of a cubic configuration, the selection is very simple, since the direction orthogonal to each couple of parallel faces can be selected.

It is worth noting that the improvement of  $k_r$  does not depend on the number of faces of the regular polyhedron, but on the total number of sensors installed. Considering the cubic configurations, the values of  $k_r$  are determined as reported in Table 14. The values of  $k_r$  are purely theoretical, since some misalignment must be accounted for. However, this can be reduced to a negligible term during calibration.

Table 14. Fraction of gyro bias standard deviation for each redundant cubic configuration.

<b>Config. no.</b>	<b>Gyros per face</b>	<b>Total number of gyros</b>	<b><math>k_r</math></b>
1	0.5 (no redundancy)	3	1
2	1.0 (two sensor per axis)	6	0.71
3	1.5 (three sensors per axis)	9	0.58
4	2.0 (four sensors per axis)	12	0.50
5	3.0 (six sensors per axis)	18	0.41

### 4.3.3. Reference hardware system

The core of the redundant configuration is the world's densest sensor board, the SensorTile™ (STMicroelectronics 2017), shown in Figure 46.a, which is an embedded platform designed, produced and sold by ST Microelectronics™. This platform has been equipped with different sensors mandated to detect and measure movement, environmental and acoustic parameters. Furthermore, a suitable development kit, the STEVAL-STLKT01V1™, is available on the market, which includes a cradle expansion board (Figure 46.b) to support both software and system architecture design and a compact cradle host for on-field testing and data acquisition.

With regard to the SensorTile™, it consists of a small board, whose dimensions are 13.5 x 13.5 mm<sup>2</sup> and, apart from a sensor that measures acoustic quantities, it includes the following components useful for navigation applications:

- A 32-bits Cortex-M4 Arm-core processor by STMicroelectronics™, namely STM32L476. The ultra-low-power microcontroller is characterized by (i) maximum operating frequency of 80 MHz, (ii) up to 1 Mbyte flash program memory, (iii) 128 Kbyte data memory, and (iv) several internal peripherals including those implementing Serial Peripheral Interface (SPI) and Inter Integrated Circuit (I<sup>2</sup>C);
- An inertial module, the LSM6DSM™ (also called iNemo™). It integrates a 3D digital accelerometer and a 3D digital gyroscope operating at 0.65 mA in high-performance mode and enabling always-on low-power. The LSM6DSM™ offers real, virtual and batch sensors with 4 Kbytes for dynamic data batching. The various sensing elements are manufactured using specialized micromachining processes, while the IC interfaces are developed using Complementary Metal Oxide Semiconductor (CMOS) technology that allows the design of a dedicated circuit which is trimmed to better match the characteristics of the sensing element. The LSM6DSM™ has a full-scale acceleration range of  $\pm 2/\pm 4/\pm 8/\pm 16$  g and an angular rate range of  $\pm 125/\pm 245/\pm 500/\pm 1000/\pm 2000$  dps, that with the 16-bit Analog-to-Digital Converter (ADC) assures resolutions as low as 0.061 mg/(Least Significant Bit, LSB) and 4.375 mdps/LSB. With regard to the error components, iNemo™

specifications list (i) an acceleration and angular rate noise density respectively equal to  $40\mu\text{g}/\sqrt{\text{Hz}}$  and  $3.8\text{mdps}/\sqrt{\text{Hz}}$  and (ii) a bias of  $\pm 40\text{mg}$  and  $\pm 3\text{ dps}$  for accelerometer and gyroscope, respectively. The LSM6DSM™ includes a dedicated configurable signal processing unit and a SPI (up to 10MHz) configurable for both gyroscope and accelerometer and is characterized by high robustness to mechanical shock;

- The LSM303AGR™ (also called eCompass™). It is an ultra-low-power high-performance system with a 3D digital linear acceleration sensor and a 3D digital magnetic sensor. The device has linear acceleration full scales of  $\pm 2\text{g}/\pm 4\text{g}/\pm 8\text{g}/\pm 16\text{g}$  and a magnetic field dynamic range of  $\pm 50$  gauss with a magnetic sensitivity equal to  $1.5\text{mgauss}/\text{LSB}$  and bias equal to  $\pm 60$  mgauss. The LSM303AGR™ includes an I<sup>2</sup>C serial bus interface that supports clock frequency from 100kHz to 3.4Mhz and an SPI serial standard operating up to 10MHz. The system can be configured to generate an interrupt signal for freefall, motion detection and magnetic field detection;
- A pressure sensor, namely LPS22HB™. It is an ultra-compact piezoresistive absolute pressure sensor that works as a digital barometer, useful for altitude measurement. The device comprises a sensing element and an IC interface, which communicates through I<sup>2</sup>C or SPI from the sensing element to the application controller. It is guaranteed to operate over a temperature range from  $-40\text{ }^{\circ}\text{C}$  to  $+85\text{ }^{\circ}\text{C}$  and has a measurement interval between 260-1260 hPa; associated with a 24-bits ADC, the sensor exhibits a sensitivity equal to 4096 LSB/hPa for pressure and 100 LSB/ $^{\circ}\text{C}$  for temperature, while its RMS noise value is equal to 0.0075Pa. The package is holed to allow external pressure to reach the sensing element;
- The BLUENRG-MS™. It is a very low power Bluetooth Low Energy (BLE) single-mode network processor, compliant with Bluetooth specification v4.2. The BLUENRG-MS™ can act as master or slave. The entire Bluetooth low energy stack runs on the embedded ARM Cortex M0 core. The maximum peak current is only 8.2 mA at 0 dBm of output power. Ultra-low-power sleep modes and very short transition times allow very low average current consumption,

resulting in longer battery life. The BLUENRG-MS™ offers the option of interfacing with external microcontrollers using SPI transport layer.

The SensorTile™ has all the electronic components on the top side and small connectors on the bottom side to plug it into the cradle expansion board.

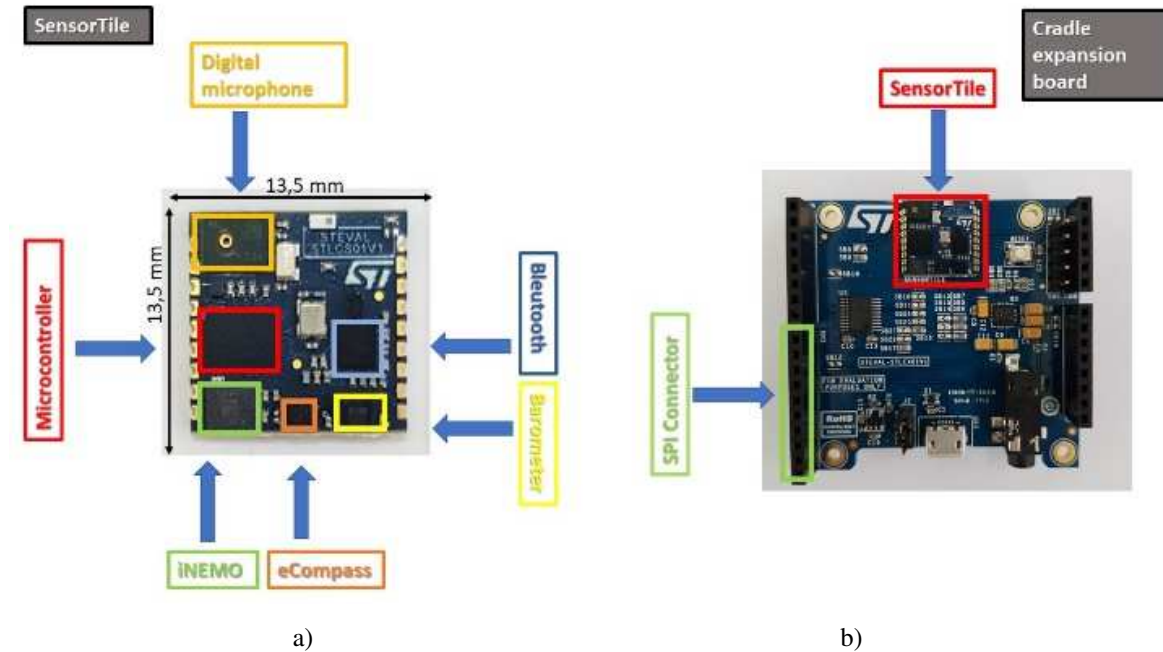


Figure 46. a) SensorTile board along with all integrated components, b) cradle expansion board.

#### 4.3.4. System integration

A redundant IMU prototype has been designed and realized by using six SensorTiles™, in order to compensate typical inertial sensors biases and consequently reduce the uncertainty in attitude determination (Figure 47). Both hardware and software solutions and configurations are described in the following with specific regard to the required acquisition constraints, i.e. raw measurements of angular velocity, acceleration and magnetic field synchronized by the six SensorTiles™ every 10 ms.

The six SensorTiles™ have been mounted on the cradle expansion board. The choice has been made for the offered opportunity of easily mounting the SensorTiles™ on the cradle board without welding. Moreover, a STM32F401RE™ board has been used as concentrator, mandated to receive the raw sensors data and send them back to the computer

by means of a USB-emulated serial port with a 926100 bit/s baud-rate for successive off-line data processing through the ZUPT filter, adopted to initialize the IMU output.

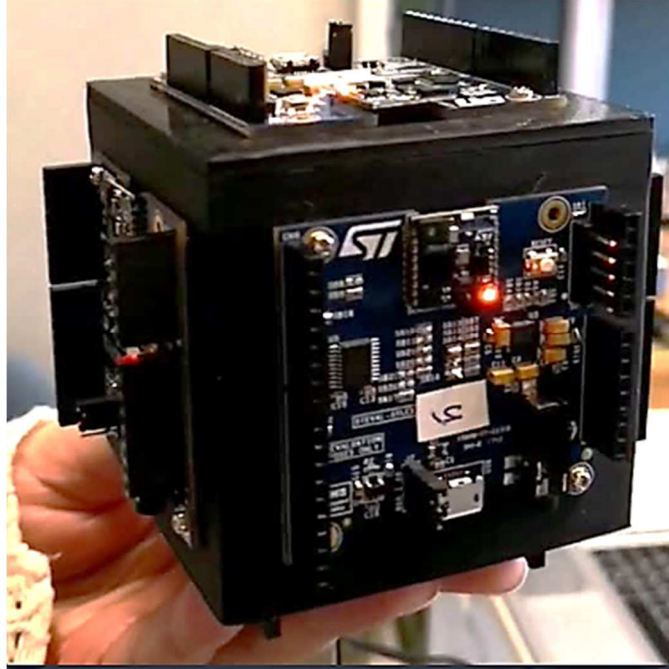


Figure 47. Redundant IMU prototype designed and realized by using six SensorTiles™.

#### **4.3.4.1. Hardware configuration**

The communication between the six SensorTiles™ and the concentrator is achieved through wired connections exploiting the SPI protocol. The power supply for all sensor cards is always provided by the concentrator via physical connections. With regard to data transmission between SensorTiles™ and concentrator, the following connection lines are required (Figure 48):

- Two lines for full-duplex data transmission Master Input/Slave Output (MISO) and Master Output/Slave Input (MOSI);
- A serial clock line from master;
- A selection line (the so-called Chip Select, CS) of the specific sensor board.

The SPI protocol allows to reach transmission speeds up to 10 MHz. In this configuration, the transmission speed has been set to 1 MHz both between the individual sensors (iNemo™ and eCompass™), on the SensorTiles™ and between the SensorTiles™

and the concentrator to acquire data every 10 ms according to specific requests of the ZUPT filter, adopted to initialize the IMU output. A wired bus has therefore been built where the signals of MISO, MOSI, SCK, supply line and ground are connected among the boards. This way, SensorTiles™ have been all powered by the 5V concentrator, thus avoiding unwanted ground interferences. Moreover, SB12, SB13, SB14 and SB15 were contacted in order to use the output pins of the cradle expansion board evidenced in Figure 48.

#### **4.3.4.2. Software implementation**

The Eclipse Integrated Development Environment for C/C++ Developers has been used to compile, program, and debug the microcontrollers of both the SensorTiles™ and the concentrator. To assure a reliable and fast data acquisition and transmission, a suitable code has been implemented. Raw data are transmitted via serial port to Matlab™ where the acquired and processed data have been made available thanks to an appropriate Graphical User Interface (GUI) (Figure 48). The measurement procedure enlists the following steps:

1. A user-friendly Matlab™ GUI sends, through the USB-emulated serial port, an acquisition start signal to the concentrator, thanks to a virtual START button;
2. To carry out data acquisition every 10 ms, a timer peripheral of the concentrator has been appropriately configured;
3. For each sampling period, the concentrator sets the value of all CS line to 0 for about 100 ms; the falling edge of CS line acts as trigger event for the SensorTiles™, which communicate with the corresponding inertial sensors (both iNemo™ and eCompass™) to retrieve the associated raw measures;
4. Once expired the acquisition time of about 100  $\mu$ s, the concentrator (acting as master for the SPI communication) selects by means of the signal of CS, active low, the microcontroller of one SensorTile™ (acting as slave);
5. The microcontroller of the SensorTile™ becomes master and communicates with the iNemo™ and eCompass™ modules via internal SPI in order to gain the raw data from the corresponding registers;
6. Received raw data are then sent from the SensorTile™ to the concentrator;
7. Steps from 4 to 6 are repeated for each SensorTile™ in the redundant configuration; all the raw data are collected in a proper array for the successive transmissions; it is

- worth noting that, to reduce the transmission time, an integer binary format (corresponding to the actual ADC output of the inertial sensors) has been adopted;
8. Finally, raw data are transmitted from the concentrator to the computer using the Matlab™ algorithm that processes them by multiplying each data by its sensitivity to achieve the measures of the quantities of interest.

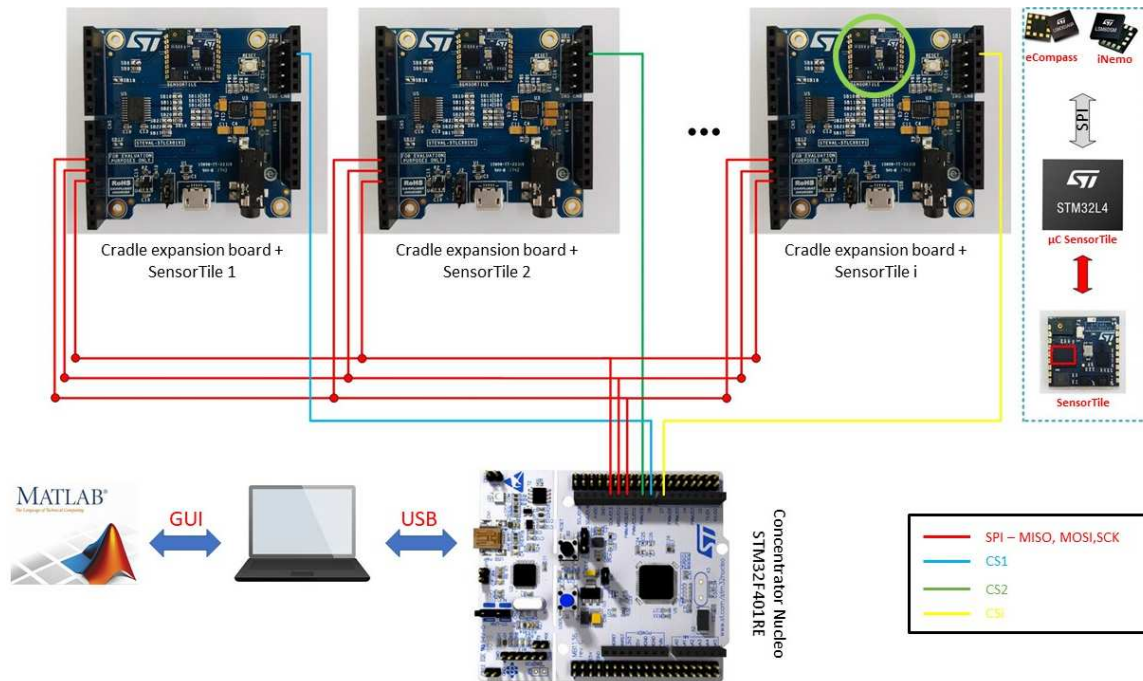


Figure 48. System integration (Hardware & Software).

#### 4.3.5. Relative alignment among MEMS gyros

The relative alignment between the six MEMS gyros can be estimated by considering the transformation matrixes  $C_n^b$  that describe the orientation of each sensor's body frame in the navigation frame North-East-Down (NED) (Groves 2013; Sotak 2010). The transformation matrixes are defined by a sequence of three rotations of the planes  $[\phi]_1, [\theta]_2, [\psi]_3$  comprising Euler angles  $\phi$  (roll),  $\theta$  (pitch),  $\psi$  (yaw or heading) (Cai *et al.* 2011).

The Euler angles are three angles introduced by Euler to describe the orientation of a rigid body. Indeed, the relative orientation between any two Cartesian frames can be described by Euler angles. In the case of the transformation from the navigation frame NED

to the body frame, the adopted Euler angles move the reference frame to the referred frame, following a Z-Y-X (or the so-called 3–2–1) rotation sequence (Cai *et al.* 2011):

1. YAW ANGLE, denoted by  $\psi$ , is the angle from the  $X_{\text{NED}}$  axis to the projected vector of the  $X_{\text{BODY}}$  axis on the  $X_{\text{NED}} - Y_{\text{NED}}$  plane. The right-handed rotation is about the  $Z_{\text{NED}}$  axis. After this rotation, denoted by  $[\psi]_3$  (Eq. (41)), the NED frame transfers to a once-rotated intermediate frame;
2. PITCH ANGLE, denoted by  $\theta$ , is the angle from the  $X'$  axis of the once-rotated intermediate frame to the  $X_{\text{BODY}}$  axis. The right-handed rotation is about the  $Y'$  axis of the once-rotated intermediate frame. After this rotation, denoted by  $[\theta]_2$  (Eq. (42)), we have a twice-rotated intermediate frame whose  $X''$  axis coincides with the  $X_{\text{BODY}}$  axis;
3. ROLL ANGLE, denoted by  $\phi$ , is the angle from the  $Y''$  axis (or  $Z''$  axis) of the twice rotated intermediate frame to that of the body frame. This right-handed rotation, denoted by  $[\phi]_1$  (Eq. (43)) is about the  $X''$  axis of the twice-rotated intermediate frame (or the  $X_{\text{BODY}}$  axis).

$$[\psi]_3 = \begin{bmatrix} \cos\psi & \sin\psi & 0 \\ -\sin\psi & \cos\psi & 0 \\ 0 & 0 & 1 \end{bmatrix} \quad (41)$$

$$[\theta]_2 = \begin{bmatrix} \cos\theta & 0 & -\sin\theta \\ 0 & 1 & 0 \\ \sin\theta & 0 & \cos\theta \end{bmatrix} \quad (42)$$

$$[\phi]_1 = \begin{bmatrix} 1 & 0 & 0 \\ 0 & \cos\phi & \sin\phi \\ 0 & -\sin\phi & \cos\phi \end{bmatrix} \quad (43)$$

For each sensor, the transformation matrix from the body frame to the navigation frame is obtained during the initialization process, by adopting the ZUPT filter. Once obtained the 6 transformation matrixes from the sensors' body frames to the navigation frame  $C_{bi}^n$  ( $i = 1, \dots, 6$ ) and chosen a reference orientation that can be one of the sensors' orientations (e.g. face 1 in Figure 49), it is possible to compute the transformation matrixes that define the relative orientation of each sensor with respect to the reference. Indeed, since the

transformation matrixes are orthogonal (Groves 2013; Sotak 2010), an inverse transformation from the navigation frame to the body frame can be calculated as follows:

$$C_n^b = [C_b^n]^T \quad (44)$$

By adopting Eq. (44):

$$C_{br}^{bi} = C_n^{bi} \cdot C_{br}^n = [C_{bi}^n]^T \cdot C_{br}^n \quad (45)$$

where  $C_{br}^n$  is the transformation matrix from the reference frame to the navigation frame,  $C_{bi}^n$  is the transformation matrix from the sensors' body frames ( $i = 2, \dots, 6$ ) to the navigation frame and  $C_{br}^{bi}$  is the transformation matrix from the reference frame to the sensors' body frames.

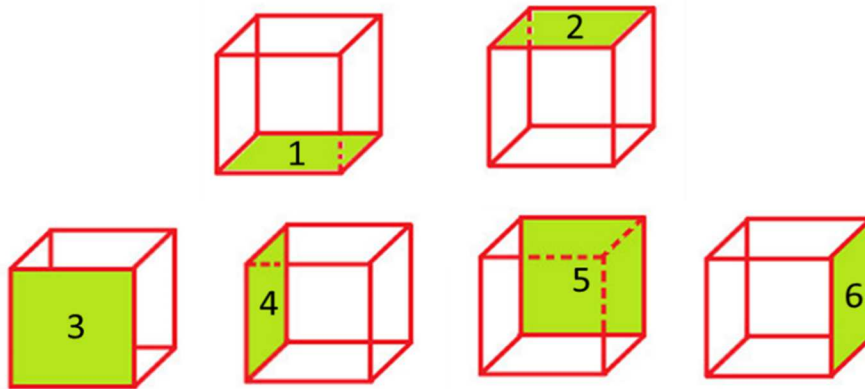


Figure 49. Faces of a cubic configuration of MEMS inertial sensors.

#### 4.3.6. Application and results

The effect of self-calibration on the determination of flight attitude has been investigated. The triaxial gyro output for a single face of the cubic configuration is shown in Figure 50. Data have been acquired at a sampling frequency of 100 Hz, for 2 minutes. The aim of this test is to determine if the self-calibration due to redundancy provides an advantage in case the unit needs to integrate free-inertial equations when GNSS data is missing, and no aiding information can be provided. To this scope, the quaternion approach has been adopted (Savage 1998). Figure 51 compares the trend with time of rotation angles  $\theta$  (see Eq. (35)), obtained 1) by integrating a single gyro output and 2) by adopting a cubic

sensors' configuration. Table 15 presents the time in which the flight attitude accuracy meets the requirements imposed by (FAA 2012). Being  $t_{red}$  the time taken by exploiting the redundant configuration and  $t$  the time taken by considering a single gyro output,  $\Delta t\%$  is computed according to Eq. (46).

$$\Delta t_{\%} = \frac{t_{red} - t}{t} * 100 \quad (46)$$

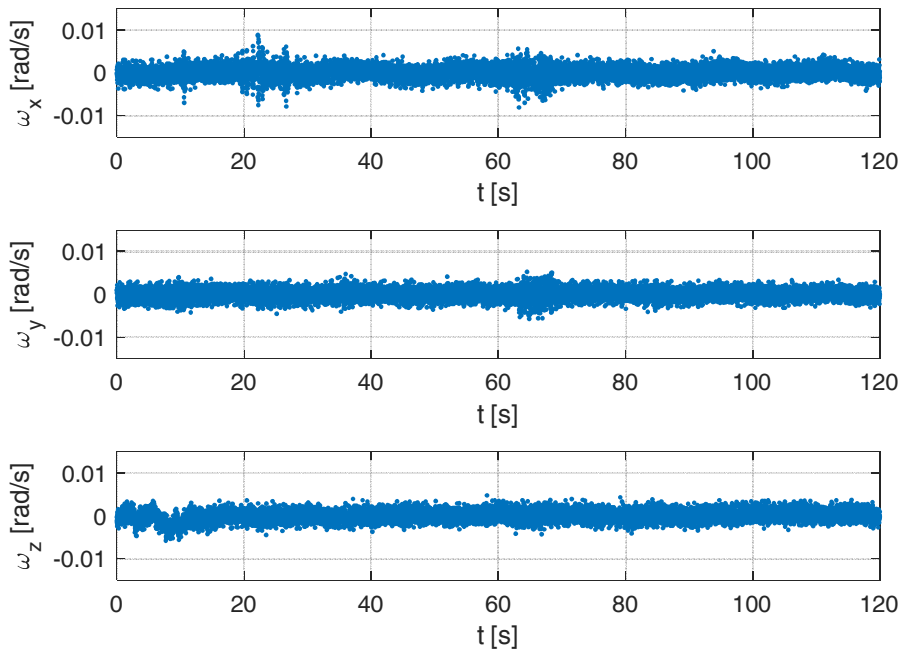


Figure 50. Triaxial MEMS gyro output.

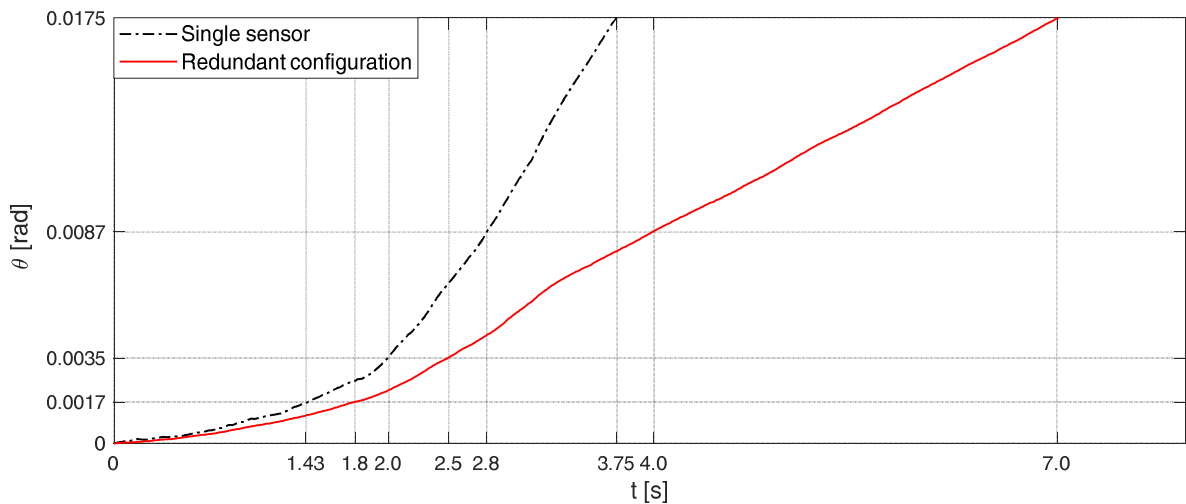


Figure 51. Trend of the rotation angle  $\theta$  with time.

Table 15. Time in which the flight attitude accuracy meets the imposed requirements.

$\theta$ [rad]	$t_{red}$ [s]	$t$ [s]	$\Delta t\%$
$1.70 \times 10^{-3}$	1.80	1.43	25.87
$3.50 \times 10^{-3}$	2.50	2.00	21.95
$8.70 \times 10^{-3}$	4.00	2.80	44.96
$1.75 \times 10^{-2}$	7.00	3.75	87.73

In the absence of GNSS, the navigation system relies on dead reckoning navigation, so that accuracy tends to degrade in direct proportion to time and distance travelled (Barbour 2010). Indeed, inertial sensors are dead-reckoning sensors (Titterton & Weston 2004), that is a measurement depends on the previous ones through integration. Therefore, measurement errors accumulate with time. However, redundancy guarantees the partial sensors' bias self-calibration. Therefore, by exploiting a redundant configuration, the time in which the flight attitude accuracy meets the requirements imposed by (FAA 2012) can be significantly increased (Table 15). Moreover, the redundant configuration is more robust and a graceful degradation can be realized in case of single-sensor failure.

# Chapter 5

---

## Solutions for Mission Management

### 5.1. UAS Trajectory Prediction

#### 5.1.1. Introduction

In a scenario of rapid growing small UAS applications, a trajectory prediction tool is needed to allow the UTM system to predict separation and collision threats within a safe time-frame. However, the diverse vehicle types, configurations, operational objectives, range, and endurance pose significant challenges to the UTM system (Ishihara *et al.* 2016). Moreover, since they are light in weight, relatively slow, and operate at low altitudes (< 400 ft. AGL), small UAS are most likely operating within the Atmospheric Boundary Layer (ABL) and are subjected to varying frequency of changes in environment within the ABL (Ren *et al.* 2017).

The requirements for a trajectory prediction tool for small UAS are listed below (Castillo-Effen *et al.* 2017) (Ren *et al.* 2017) (D'Souza 2017) (Ishihara *et al.* 2016):

- It should be generalized to accommodate multiple vehicle types and airspace environments (wind, terrain, etc.);

- Since trajectory predictions may feed real-time decision support tools, the predictions should be generated rapidly;
- As more experimental validation data become available, it should be possible to increase the accuracy of the trajectory prediction tool;
- Trajectory predictions should allow for adaptation to multiple uses. They may be used in conjunction with tools to determine potential risks, to protect other airspace users, or to take risk mitigation measures.

Several recent studies have considered the trajectory prediction problem. To address the need to develop methods that can rapidly integrate and regulate the diverse UAS trajectories entering the airspace, an algorithm utilizing a kinematic fixed-wing model is presented in (Ishihara *et al.* 2016). The algorithm was simulated with the UAS flying at constant altitude in a uniform wind field to achieve required arrival times. In (D'Souza *et al.* 2016; D'Souza 2017), a generalized six-degree-of-freedom (6DoF) multirotor trajectory model to identify vehicle performance in the presence of wind is described. Moreover, ongoing work on developing a trajectory prediction model that uses kinematic equations of motion to determine future state of the UAS is presented in (Tyagi *et al.* 2017). These equations use a pre-defined lookup table to estimate bounds on UAS performance under the given state. Finally, a framework for the development and validation of trajectory modelling and prediction methods for the diverse small UAS types under nominal environment and under a variety of realistic potential hazards, including adverse environmental conditions and vehicle and system failures, is presented in (Ren *et al.* 2017).

A trajectory prediction tool for UAS, based on the use of Learning Vector Quantization (LVQ) Neural Networks (Fontanella *et al.* 2017b) is proposed in this chapter. LVQ Neural Networks, introduced by T. Kohonen (Kohonen 1989, 1990), are composed by a first competitive layer and a second linear layer. The linear layer transforms the competitive layer's classes into target classifications defined by the user (Shen & Chen 2009). They can exploit flight data collected when the UAS executes a pre-assigned flight path to support trajectory prediction in standard traffic scenarios, by using an adaptive model learned during the network training.

### 5.1.2. UAS trajectory model

The model proposed in this thesis is based on the discretization of a generic trajectory in a certain number of elements. Figure 52 shows an example of such trajectory between an initial point A and a final point B, divided in 6 elements. Since UAS speed is approximately constant in straight elements, the trajectory has been discretized in elements with a not-null angle between two adjacent segments. This model can be used to predict the time taken by the UAS to fly through each element, which can be obtained by estimating the speed variation  $\Delta V_i$ :

$$t_i = L/(|V_{init}| + \Delta V_i) \quad (47)$$

where  $|V_{init}|$  is the initial UAS speed in the element  $i$ ,  $L$  is the length of the element and  $t_i$  is the time taken by the UAS to fly through the element  $i$ .

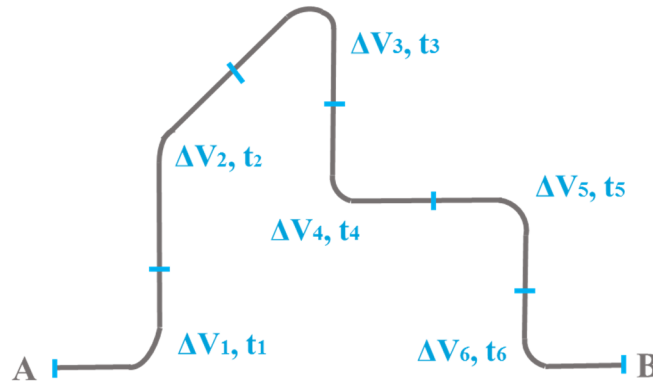


Figure 52. Example of a generic UAS trajectory between the initial point A and the final point B.

In the reported model, the two segments that compose each element have a fixed length. Thus, the shape of each element depends only on the angle between the two segments. Since trajectories are sensitive to wind, due to small UAS size and low operational altitude (Xue 2017), wind data over the course of the operation plan should be integrated into the current framework. Therefore, the representative features of UAS trajectories are:

1. The angle between the two segments that compose an element of trajectory ( $\theta$ );
2. The wind direction referred to the first segment ( $\theta_w$ );
3. The wind speed ( $|V_w|$ ).

For each feature, a certain number of classes are considered as a trade-off between the required accuracy and the processing loads. If the number of classes increases, the accuracy of the model will improve, but the computational load will increase. Since future scenarios envisage the use of UAS within intense traffic systems, it will be essential to use tools able to predict trajectories rapidly (Ishihara *et al.* 2016). Furthermore, a discretization with more classes leads to an increase of the confusion between near classes. Therefore, it is better to realize a reliable and faster tool, even though less accurate, with a limited number of classes.

It is also necessary to consider the symmetry of the problem. For example, the two conditions shown in Figure 53 have a symmetric combination of features. In the figure,  $V_{init}$  is the initial UAS velocity,  $V_w$  is the wind velocity,  $N$  and  $E$  are respectively the North and East directions. It is possible to notice a symmetry between the shape of the element (in terms of the angle between the two segments) and the wind direction. The symmetric combination of features can simplify the problem, reducing the number of classes. Therefore, the following classes have been considered:

1. Four classes for the angle between the two segments that compose each trajectory element:

$$\theta = [0,45, 90,135]degrees \quad (48)$$

2. Eight classes for the wind direction:

$$\theta_w = [0,45, 90,135,180,225,270,315]degrees \quad (49)$$

3. Four classes for the wind speed:

$$|V_w| = [2.5, 5, 7.5,10] \frac{m}{s} \quad (50)$$

The numeric values in Equations (48), (49) and (50) are the centres of the classes. It is worth noting that, for the symmetry of the problem, only four classes for the relative angle between the two segments that compose each trajectory element have been considered.

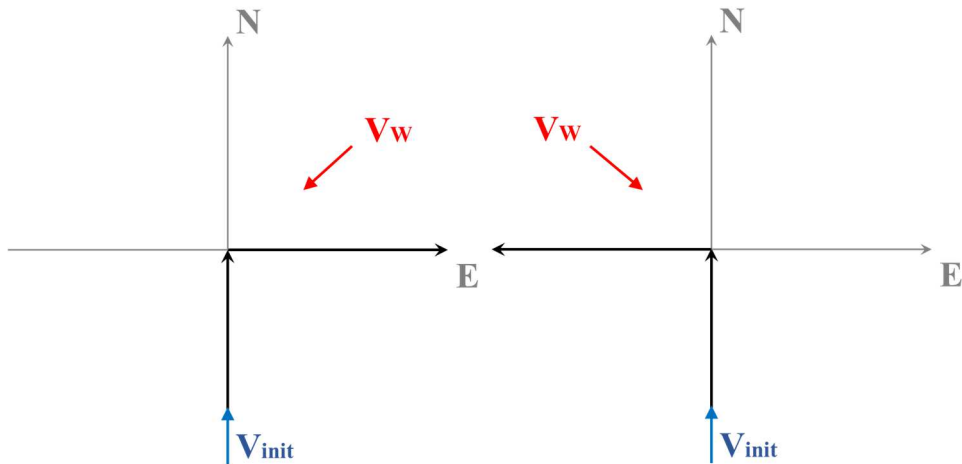


Figure 53. Symmetric combination of features.

### 5.1.3. Trajectory prediction through LVQ Neural Networks

#### 5.1.3.1. LVQ Neural Networks general description

This thesis proposes a tool that employs LVQ Neural Networks (Kohonen 1989, 1990) to predict the time taken by the UAS to fly through the elements in which the trajectory has been discretized. Learning Vector Quantization is an adaptive method for data classification (Melin *et al.* 2014) based on training data with the desired class information (Karayiannis 1997). A comprehensive review of the most relevant supervised LVQ algorithms is presented in (Nova & Estévez 2013).

The training procedure consists of two steps, a first stage of unsupervised learning for data clustering (Jang *et al.* 1997) and a second stage of supervised learning to obtain class-labelled prototypes (classifiers) (Nova & Estévez 2013). During the first stage, the centres of the clusters (or weight vectors) are identified to represent the dataset without the class information (Melin *et al.* 2014). The number of clusters can be specified a priori, or by some clustering techniques capable of adaptively adding new clusters as needed (Melin *et al.* 2014). After obtaining the clusters, their classes must be labelled by the voting method (a cluster is labelled as class  $k$  if most of the data within the cluster belonging to the class  $k$ ) (Melin *et al.* 2014). This process is based on the general assumption that the input data that are similar, usually belong to the same class (Jang *et al.* 1997). During the second stage of supervised learning, the class information is used to refine the position of the centres of the clusters and thus minimize the number of misclassified cases (Melin *et al.* 2014).

From the structure perspective, the LVQ Neural Network is composed by three layers, such as an input layer, a competitive layer and an output layer (Shen & Chen 2009). In the network, the input layer and competitive layer are fully connected, since all the units in the input layer are connected to all the neurons in the competitive layer with connection weights, whereas the competitive layer and output layer are partly connected, since the components of the resultant vector are binary values 0 and 1 (Shen & Chen 2009). The training algorithm is summarized as follows:

1. Initialize the centres of clusters (or weight vectors) (Shen & Chen 2009), (Melin *et al.* 2014);
2. Label each cluster by the voting method (Melin *et al.* 2014);
3. Select the winning neuron in the output array, for each input vector. Indeed, the output layer output only one neuron, which is called winner neuron. The winner neuron is selected as the neuron with the minimum distance between an input vector  $x$  and its connection weight vector  $w$ . The LVQ algorithm calculates directly the Euclidean distance (Melin *et al.* 2014):

$$D(w, x) = \sqrt{(w_1 - x_1)^2 + \dots + (w_n - x_n)^2} \quad (51)$$

The winner neuron is allowed to output “1” and other neurons are restrained to output “0” (Shen & Chen 2009);

4. The centres of clusters are tuned to approximate the desired result. If  $x$  and  $w$  belong to the same class,  $w$  will move toward  $x$ , otherwise  $w$  will move away from  $x$ . In other words, if  $x$  and  $w$  belong to the same class,  $w$  will be updated by:  $\Delta w = \eta(x - w)$  otherwise,  $w$  will be updated by:  $\Delta w = -\eta(x - w)$  where  $\eta$  is the learning rate, a positive constant to be decremented in each iteration (Melin *et al.* 2014).

It is worth noting that the training procedure described above should be performed only one time for each UAS. Then, the so trained LVQ Neural Network can be used to estimate the time taken by the UAS to fly any type of future trajectory by discretization in elementary parts, in several wind conditions. The main advantage of using LVQ Neural Networks is the possibility to create different models for the different UAS types, being the Neural Networks

self-adaptive in constructing a mathematical model, after several repetitive learning and testing phases.

### **5.1.3.2. LVQ Neural Networks for trajectory prediction**

LVQ Neural Networks for trajectory prediction have been built and trained by using the Matlab Neural Networks Toolbox<sup>TM</sup>. Figure 54 shows the Neural Network structure adopted in this application, whereas the training process is shown in Figure 55. The input layer has 3 neurons, which correspond to the angle between the two segments that compose each trajectory element, the wind direction and the wind speed. The output is the UAS speed variation in the elements in which the trajectory has been discretized. By knowing the speed variation, it is possible to compute the time by Eq. (47).

As explained above, the LVQ Neural Network has a first competitive layer and a second output (or linear) layer. The classes learned by the competitive layer are referred to as subclasses, whereas the classes learned by the output layer as target classes. Both the competitive and output layers have one neuron per (sub or target) class (Hagan *et al.* 1996). Thus, the competitive layer can learn up to  $S^1$  subclasses, where  $S^1$  is the number of competitive neurons. These, in turn, are combined by the output layer to form  $S^2$  target classes, where  $S^2$  is the number of output neurons.  $S^1$  should be always larger than  $S^2$  (Hagan *et al.* 1996).

In this application, the number of classes in which the input parameters must be classified is the number of all the combinations between the input parameters that is  $4 \times 8 \times 4 = 128$ . Consequently, the output layer is composed by 128 neurons, whereas the competitive layer is composed by a multiple of the number of neurons in the output layer. In the reported model, a competitive layer composed by  $128 \times 2 = 256$  neurons is used, as a trade-off between the computational burden and the prediction accuracy. Indeed, the larger the competitive layer, the more clusters the network can learn, and the more complex mapping of input to target classes can be made. However, the computational burden will increase (Hagan *et al.* 1996).

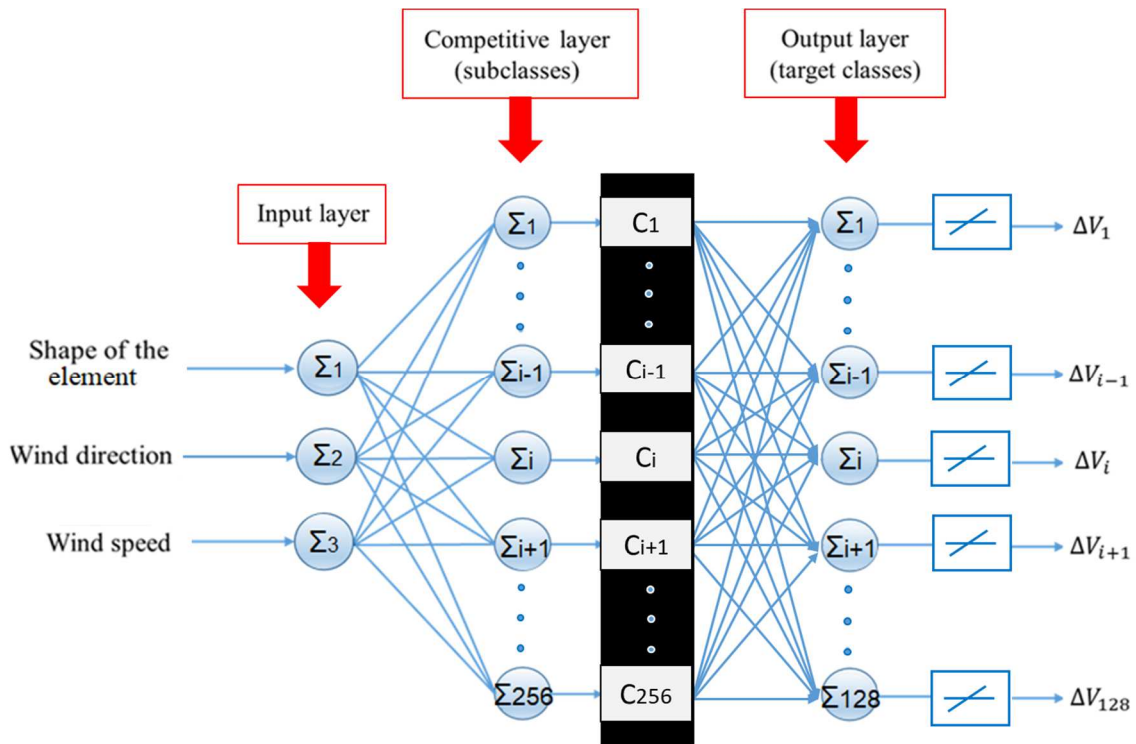


Figure 54. LVQ Neural Network structure adopted for trajectory prediction.

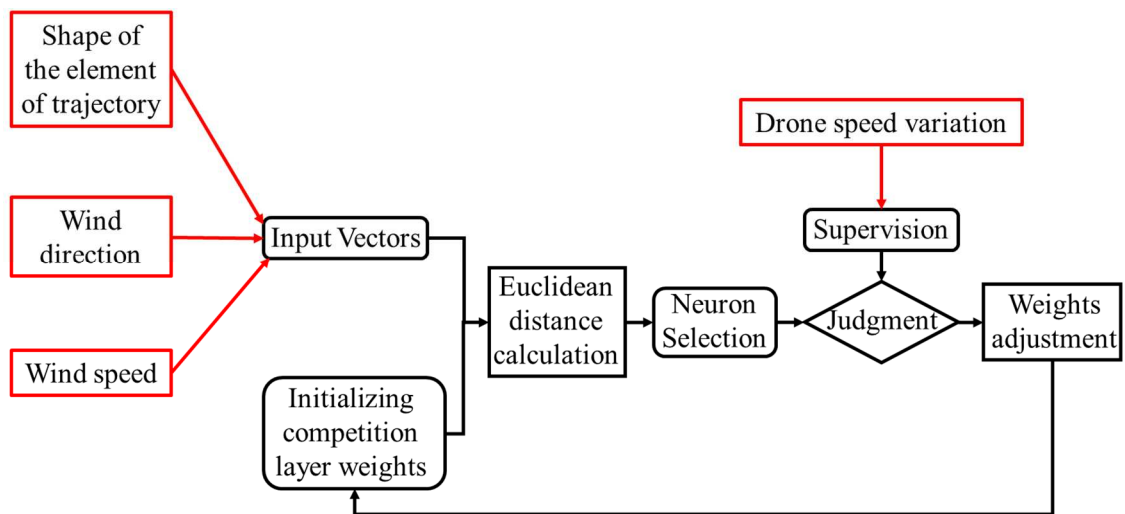


Figure 55. LVQ Neural Network training process.

## 5.1.4. Experimental tests

### 5.1.4.1. Tests description

The trajectory prediction tool has been tested on DJI Phantom 4<sup>TM</sup> flight data. The Phantom 4<sup>TM</sup> is shown in Figure 56, whereas Table 16 presents its characteristics (DJI 2018). Several experimental tests have been performed by flying the Phantom 4<sup>TM</sup> in

waypoint mode. Waypoint navigation is defined as the process of automatically following a predetermined path defined by a set of geodetic coordinates (Bruch *et al.* 2002). In other words, once selected the waypoints, the speed and the altitude, the UAS flies automatically, covering all waypoints. The selected waypoints are shown in Figure 57, where  $V_w$  is the wind velocity during the experimental tests and  $N$  and  $E$  are the North and East directions.



Figure 56. DJI Phantom 4™.

Table 16. DJI Phantom 4™ specifications.

Weight (Battery & Propellers Included)	1380 g
Diagonal Size (Propellers Excluded)	350 mm
Max Ascent Speed	S-mode: 6 m/s
Max Descent Speed	S-mode: 4 m/s
Max Speed	S-mode: 20 m/s
Max Tilt Angle	S-mode: 42°
	A-mode: 35°
	P-mode: 15°
Max Angular Speed	S-mode: 200°/s
	A-mode: 150°/s
Max Service Ceiling Above Sea Level	6000 m
Max Wind Speed Resistance	10 m/s
Max Flight Time	Approx. 28 minutes
Operating Temperature Range	0° to 40°C
Satellite Positioning Systems	GPS/GLONASS
Hover Accuracy Range	Vertical:
	±0.1 m (with Vision Positioning)
	±0.5 m (with GPS Positioning)
	Horizontal:
	±0.3 m (with Vision Positioning)
	±1.5 m (with GPS Positioning)

The experimental tests have been performed by using the software UgCS™ of SPH Engineering™ to guarantee a central management of the flight. First of all, missions have

been planned by using the UgCS™ Mission Editor (SPH Engineering 2018). The Mission Editor has also been used to flight and control missions in real-time. Finally, telemetry data acquired in real-time have been used to train and test the LVQ Neural Network in Figure 54. As shown in Figure 57, two trajectories have been designed to test the proposed tool. They can be discretized in elements characterized by a different shape and wind direction. The UAS has flown both trajectories for 10 times. Flight data of the first 7 times have been used to train the Neural Network, whereas flight data of the last 3 times have been used to test the Neural Network.

The UAS speed and altitude, selected by the remote controller, are respectively 3.33 m/s and 12.00 m. However, the speed is not constant during flight tests. It changes due to different factors, among which the most relevant, identified in this thesis, are: the shape of the considered trajectory element, the wind direction and the wind speed. During the experimental tests, the wind velocity was 2.78 m/s in the North-North East direction.

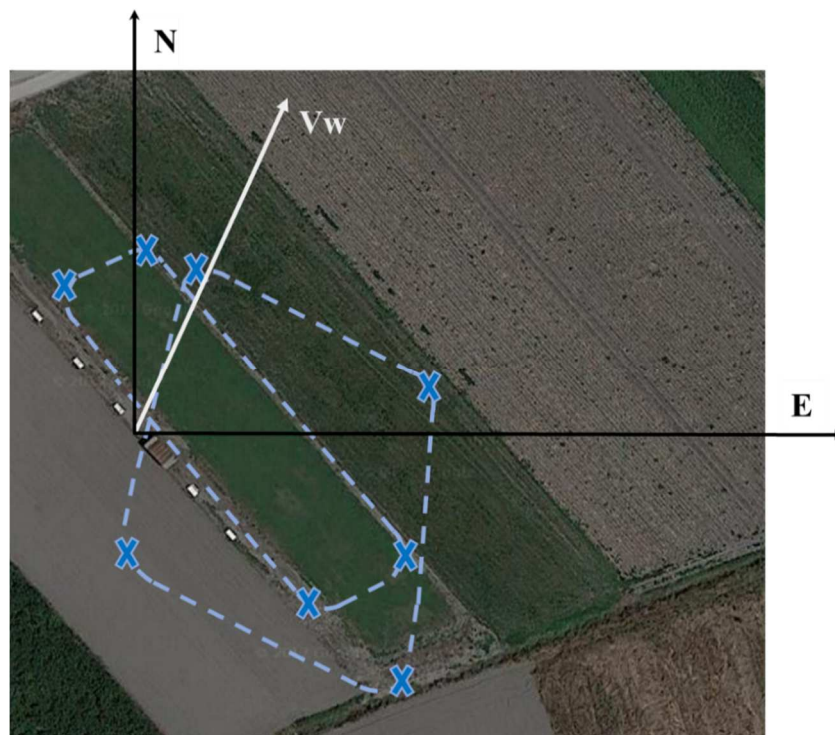


Figure 57. Selected waypoints.

#### **5.1.4.2. LVQ Neural Networks training data**

The LVQ Neural Network has been trained on the four elements highlighted in Figure 58, represented in the local projected coordinate system in Figure 59, Figure 60, Figure 61 and Figure 62. In order to make the dimensions clearer, the difference with respect to the

minimum coordinate is represented in both directions. The elements are composed by two segments of a fixed length of 10 m, in order to simplify the Neural Network structure. Indeed, it is possible to use a variable length, but it must be considered as another input in the LVQ Neural Network structure.

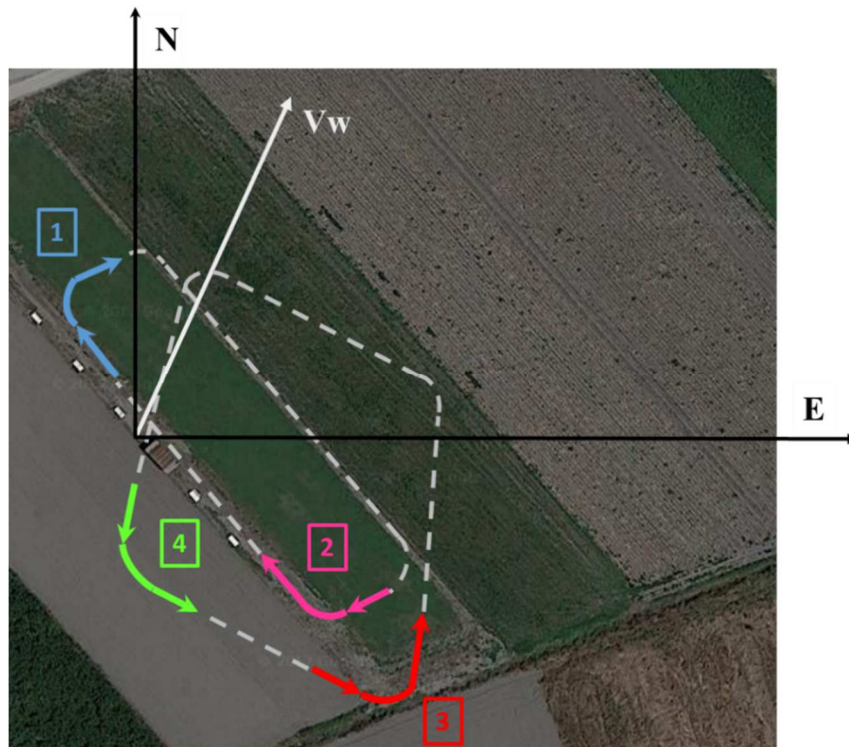


Figure 58. Trajectory elements used to train the LVQ Neural Network.

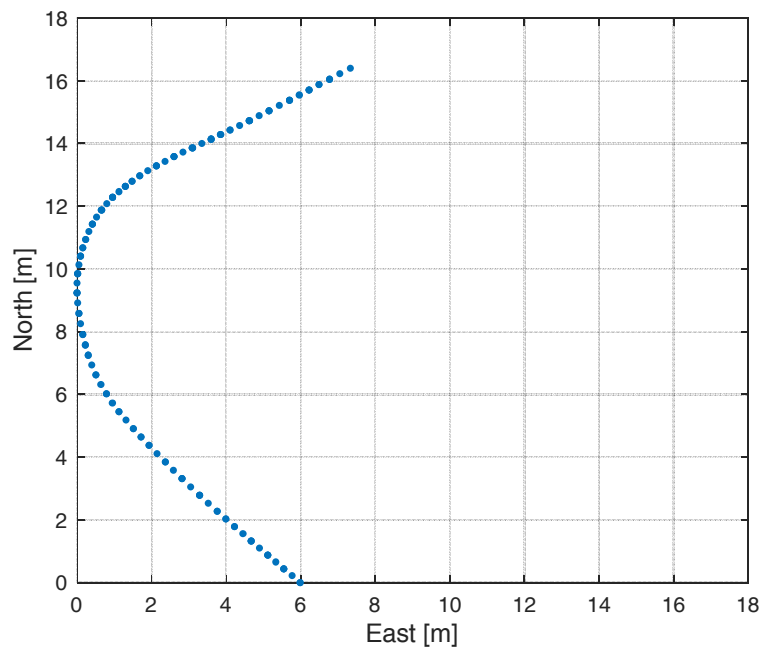


Figure 59. 1<sup>st</sup> training element in the local projected coordinate system.

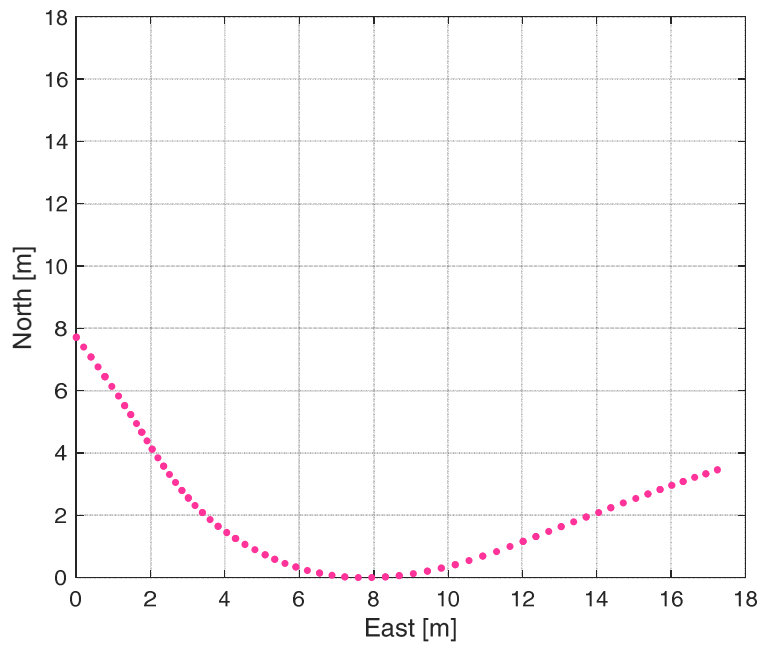


Figure 60. 2<sup>nd</sup> training element in the local projected coordinate system.

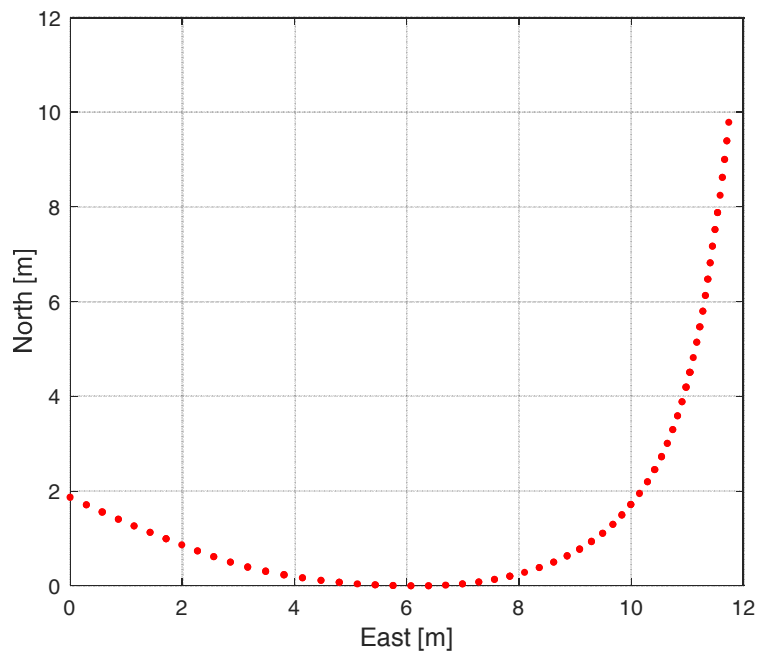


Figure 61. 3<sup>rd</sup> training element in the local projected coordinate system.

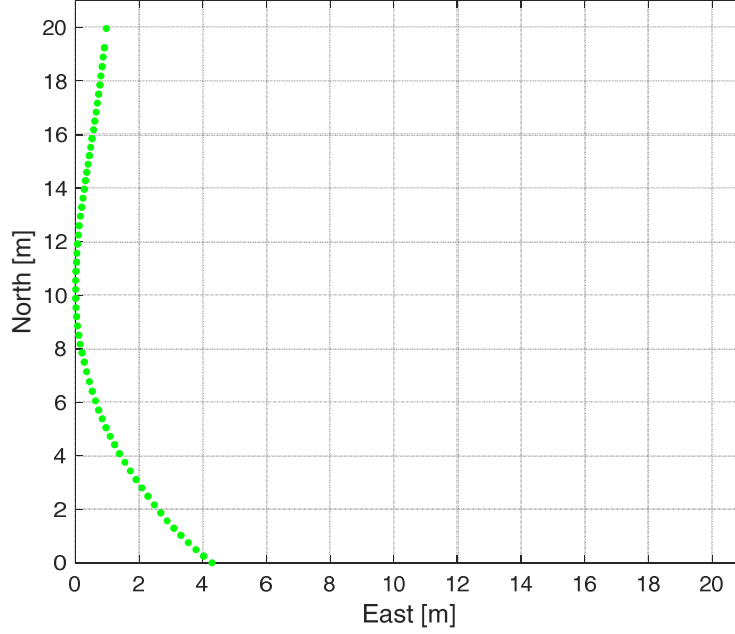


Figure 62. 4<sup>th</sup> training element in the local projected coordinate system.

The angle  $\theta$  between the two segments that compose each trajectory element can be computed in Eq. (52).

$$\cos \theta = \frac{V_1 \cdot V_2}{|V_1| \cdot |V_2|} \quad (52)$$

The scalar product  $V_1 \cdot V_2$  is computed as follows:

$$V_1 \cdot V_2 = V_{1N} \cdot V_{2N} + V_{1E} \cdot V_{2E} \quad (53)$$

In Eq. (52) and (53),  $V_1$  and  $V_2$  are the UAS velocity respectively in the first and second segment,  $V_{1N}$ ,  $V_{1E}$  and  $V_{2N}$ ,  $V_{2E}$  are the components of  $V_1$  and  $V_2$  respectively in the North and East direction,  $|V_1|$  and  $|V_2|$  are the magnitudes of  $V_1$  and  $V_2$  (Equation (54) and (55)).

$$|V_1| = \sqrt{V_{1N}^2 + V_{1E}^2} \quad (54)$$

$$|V_2| = \sqrt{V_{2N}^2 + V_{2E}^2} \quad (55)$$

In the same way, the angle  $\theta_w$ , which is the wind direction referred to the first segment, can be computed by Eq. (56).

$$\cos \theta_w = \frac{V_1 \cdot V_W}{|V_1| \cdot |V_W|} \quad (56)$$

The scalar product  $V_1 \cdot V_W$  is computed as follows:

$$V_1 \cdot V_W = V_{1N} \cdot V_{WN} + V_{1E} \cdot V_{WE} \quad (57)$$

In Eq. (56) and (57),  $V_1$  is the UAS velocity in the first segment of the considered trajectory element,  $V_W$  is the wind velocity,  $V_{1N}$ ,  $V_{1E}$  and  $V_{WN}$ ,  $V_{WE}$  are the components in the North and East directions of  $V_1$  and  $V_W$ ,  $|V_1|$  and  $|V_W|$  are the magnitudes of  $V_1$  and  $V_W$  (Eq. (54) and (58)).

$$|V_W| = \sqrt{V_{WN}^2 + V_{WE}^2} \quad (58)$$

The 1<sup>st</sup> training element (Figure 59) is characterized by:

- $\theta = 72^\circ$ ;
- $\theta_w = 64^\circ$ ;
- $\Delta V = 0.25$  m/s.

The 2<sup>nd</sup> training element (Figure 60) is characterized by:

- $\theta = 105^\circ$ ;
- $\theta_w = 140^\circ$ ;
- $\Delta V = 0.35$  m/s.

The 3<sup>rd</sup> training element (Figure 61) is characterized by:

- $\theta = 80^\circ$ ;
- $\theta_w = 90^\circ$ ;
- $\Delta V = 0.35$  m/s.

The 4<sup>th</sup> training element (Figure 62) is characterized by:

- $\theta = 130^\circ$ ;
- $\theta_w = 170^\circ$ ;
- $\Delta V = 0.40$  m/s.

The speed variation  $\Delta V$  is computed by using telemetry data of the experimental tests.

### 5.1.5. Tool application and results

The LVQ Neural Network trained on the experimental data described above is used to predict the time taken by the UAS to fly through the elements highlighted in Figure 63. These two elements are represented in the local projected coordinate system in Figure 64 and Figure 65. As explained above, the UAS has flown both trajectories shown in Figure 57 for 10 times. Data of the first 7 flights have been used to train the Neural Network (by considering the elements highlighted in Figure 58), whereas data of the last 3 flights have been used to test the Neural Network (by considering the elements highlighted in Figure 63).

Table 17 shows the performance of the trajectory prediction tool, where:

- $t_{NN}$  is the time predicted by the LVQ Neural Network;
- $t_{Real}$  is the real time taken by the UAS, computed by using telemetry data of the experimental tests;
- $e_{\%}$  is the percentage error, calculated as follows:

$$e_{\%} = \frac{|t_{NN} - t_{Real}|}{t_{Real}} \cdot 100 \quad (59)$$

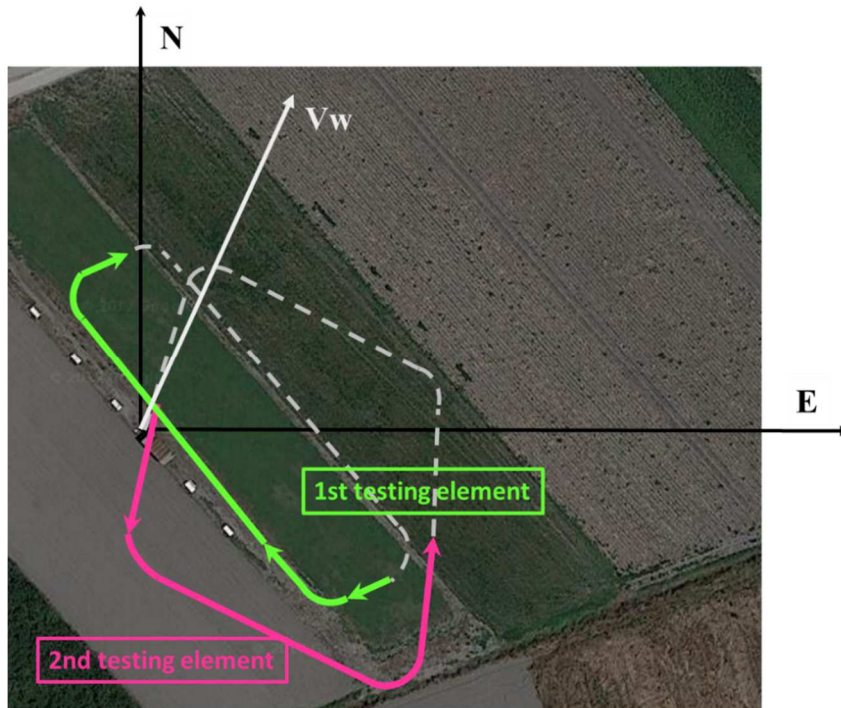


Figure 63. Trajectory elements used to test the LVQ Neural Network.

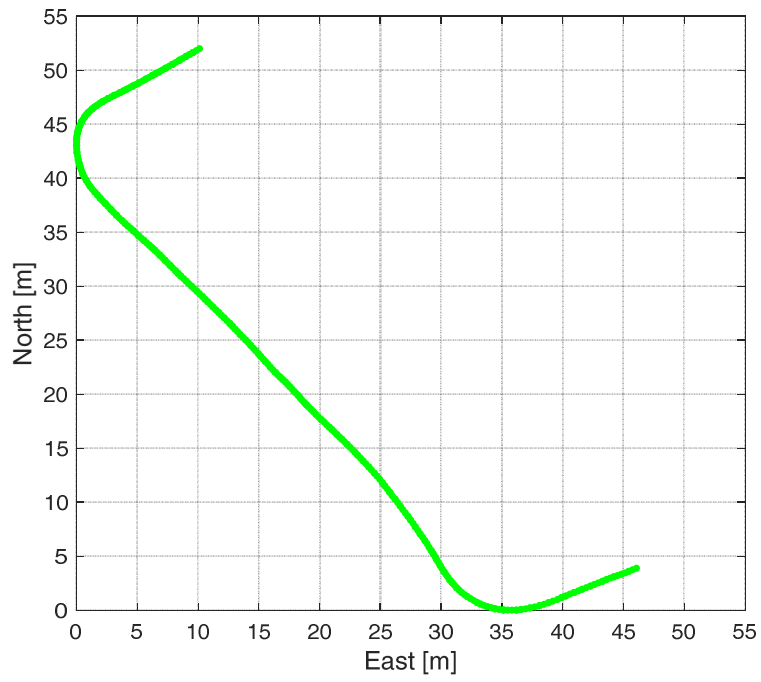


Figure 64. 1<sup>st</sup> testing element in the local projected coordinate system.

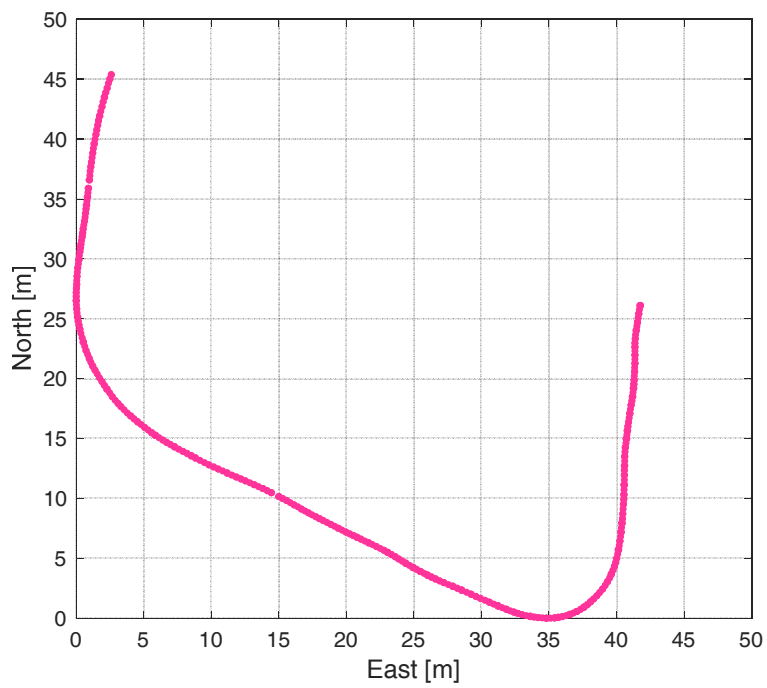


Figure 65. 2<sup>nd</sup> testing element in the local projected coordinate system.

Table 17. Trajectory prediction tool performance.

	$t_{NN}$	$t_{Real}$	$e_{\%}$
		26.15 s	4.28 %
<b>1<sup>st</sup> element</b>	27.27 s	26.28 s	3.77 %
		28.18 s	3.23 %
		25.67 s	2.10 %
<b>2<sup>nd</sup> element</b>	25.13 s	24.50 s	2.57 %
		26.00 s	3.35 %

The time taken by the UAS to fly the same trajectory elements can be slightly different during the experimental tests, due to multiple environmental factors. However, the application of LVQ Neural Networks guarantees a prediction performance fully compatible with the intended applications of assessing UAS trajectory feasibility in a timely manner and aiding autonomous decision-making systems for UAS. It is also worth noting that the proposed tool allows creating different models for the myriad of different UAS types in several wind conditions, being the ANNs self-adaptive in constructing a mathematical model after several training and testing steps.

## 5.2. Standardized Procedures for Decision-Making

### 5.2.1. Introduction

Due to the rapid growth in small UAS operations at low-altitude, the UTM system will have to manage numerous operations in real-time. However, the diverse small UAS types, configurations, operational objectives, range, and endurance pose significant challenges for the UTM system that expects a certain type of behaviour. This diversity is primarily driven by the low-cost and rapid development cycle to conceptualize, test, and deploy a new system for a given application or market need (Ishihara *et al.* 2016; Paulson *et al.* 2017). Furthermore, UAS can be equipped with different types of payload, among them cameras and microphones are the most often used (Vergouw *et al.* 2016). This scenario is

characterized by the continuous development of new technologies (Doukhi *et al.* 2017; Kelner & Ziólkowski 2017).

Technological advances in UAS research are fundamentally based on the need of satisfying the user's requirements and the flight regulations. Consequently, taking into account the large spectrum of potential applications and the relative user's requirements, it is worthwhile to try to develop a standardized approach for decision-making process to select optimal UAS / payload configurations that cover the maximum number of missions and the current and future flight regulations (ICAO 2013).

This aim can be achieved by a software tool able to adapt to the UAS ever-changing scenario, characterized by a high tendency to automation, the continuous development of new technologies and the evolution of regulations (Fontanella *et al.* 2017d, 2017c). The proposed tool can improve both the efficiency and the safety in UAS operations, speed up the flight authorization process by the UTM system, and support the increasing level of autonomy in UAS operations.

## **5.2.2. Methodology**

### **5.2.2.1. Tool description**

The tool is developed in JAVA in order to be compatible with all operating systems. It is linked to an external eXtensible Markup Language (XML) database composed by several UAS and payload types. The great advantage of the XML database is the possibility to organize large amount of data in a dataset easily usable by the tool. The XML database can be stored on a different server and updated online, considering all new technologies that will be developed with time. The tool processing logic, presented in Figure 66, can be synthesized by the following steps:

1. The user can set the mission requirements and the weather conditions in the user-input interface;
2. The typical features for each considered mission are identified, through the missions vs. features compliance matrix presented in Section 5.2.2.2;
3. Then, the equipment that should be required, or might be required for the features identified in the previous step, in terms of navigation systems, data links and systems

to ensure the situational awareness, is defined through the features vs. equipment compliance matrix presented in Section 5.2.2.3;

4. Finally, the equipment that should be required, or might be required for each selected mission, in terms of navigation systems, data links and systems to ensure the situational awareness, is defined through the missions vs. equipment compliance matrix, obtained by the two previous steps and presented in Section 5.2.2.4;
5. Once the above process is completed, the tool will suggest off-the-shelf solutions to realize the customer needs, in terms of hardware (e.g. UAS frame-structure and payload characteristics) and prescriptions (e.g. weight and cost), taking into account the current regulations. This function can be realized since the tool is linked to the XML database of existing subsystems. A requirements database is also included in the tool and can be updated by considering the evolution of regulations;
6. In case multiple solutions are identified, a strategy to measure the level of suitability of each solution to the considered mission is included in the tool. By using a scoring system defined by the user in the input interface, the tool classifies the available UAS / payload configurations, selecting the most advantageous.

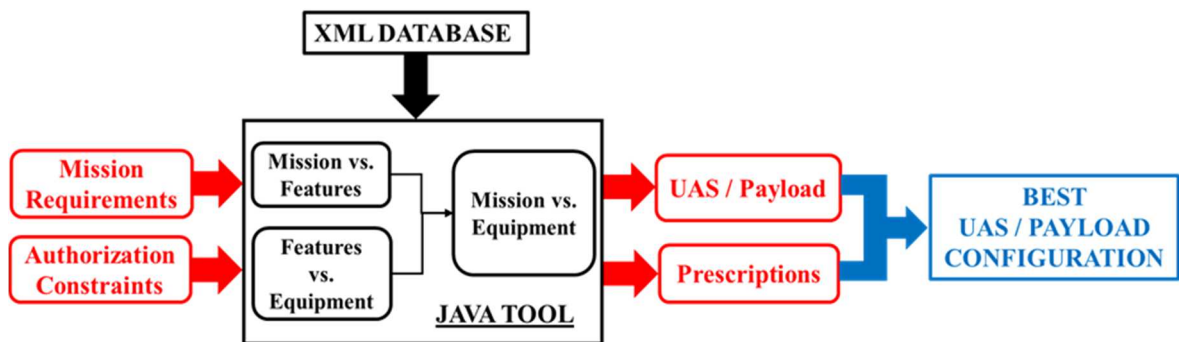


Figure 66. Tool processing logic.

#### 5.2.2.2. Missions vs. features

The main problem which affects the technological development of UAS is certainly connected to the need of maintaining a high level of safety integrating UAS into the civil airspace. In Ref. (Amazon.com Inc. 2015), the UAS capabilities required to access to a specific airspace are catalogued in four classes: Basic, Good, Better and Best. However, these requirements need to be further analysed and widen also taking into account safety

and security boundary conditions arising from each possible application in which UAS can play a significant role (Degarmo 2004).

In Table 18, the main considered applications and the features that characterize each of them are listed. The following applications have been chosen as representative for covering several commercial fields in which UAS are mainly used. Each of them can be considered as a synthesis of several others:

- Packet delivery: e.g. goods, sanitary equipment, first aids;
- Precision agriculture: e.g. crop monitoring, soil humidity, chemical and biological treatments;
- Mapping: e.g. thematic and cartographic mapping, digital elevation model;
- Surveillance: e.g. domestic perimeters;
- Law enforcement: e.g. border patrolling, surveillance of hostile demonstrations;
- Traffic monitoring: e.g. traffic flow management, monitor activities in the intersections;
- Infrastructure inspection: e.g. pipelines, railways, bridges;
- Aerial photo: e.g. filmography;
- Communication relay: e.g. extended Ground Control Station (GCS)-to-UAS communication range, aerial internet;
- Search and Rescue: e.g. natural disasters, victim detection.

Regarding the possible operations, three cases have been considered:

1. Visual Line of Sight (VLOS) in which the user keeps the UAS in visual-line-of-sight at all times;
2. Beyond Visual Line of Sight (BVLOS) in which the user does not keep the UAS in visual line of sight at all times, but a Line of Sight (LOS) radio communication is still available between the Ground Control Station (GCS) and the UAS;
3. Beyond Line of Sight (BLOS) in which both the LOS communication and the visual LOS are not available. Sometimes, it is referred as Beyond Radio Line of Sight (BRLOS).

The mission profiles can be classified into three classes:

1. Point to Point (P2P), where the flight mission requires to reach a well identified destination;
2. Hovering/Loitering, where the aircraft is limited to overfly a very small area;
3. Area Coverage, where the application requires the aerial coverage of a large area.

Table 18. Mission vs. features compliance matrix.

<b>FEATURES</b>	<b>MISSIONS</b>									
	<b>Packet Delivery</b>	<b>Precision Agriculture</b>	<b>Mapping</b>	<b>Surveillance</b>	<b>Law Enforcement</b>	<b>Traffic Monitoring</b>	<b>Infrastructure Inspection</b>	<b>Aerial Photo</b>	<b>Communication Relay</b>	<b>Search and Rescue</b>
<b>VLOS</b>	No	Yes	Yes	Yes	Yes	No	Yes	Yes	No	Yes
<b>BVLOS</b>	Yes	Yes	Yes	Yes	Yes	Yes	Yes	Yes	Yes	Yes
<b>BLOS</b>	Yes	No	No	No	Yes	Yes	No	No	Yes	Yes
<b>Mission Profile</b>	P2P	Area Coverage	Area Coverage	Area Coverage	Area Coverage	Loiter	Area Coverage/ Loiter	P2P/Loiter	Loiter	Area Coverage
<b>Risk</b>	H	L	L to H	L	H	H	M	L to H	M	M
<b>Interaction - Human</b>	H	L	L	L	L	L	L	L to H	L	H
<b>Interaction - UAS</b>	H	L	L to M	L	H	H	L	L	H	H
<b>Interaction - Manned Aircraft</b>	H	L	L	L	H	M to H	L	L	H	H
<b>Landing Accuracy</b>	H	L	L	L to M	H	H	L to H	L to M	L	H
<b>Range</b>	>5 km	<1km to >5km	1 km ÷ 5 km	1 km ÷ 5 km	<1km to >5km	>5 km	<1km to >5km	1 km ÷ 5km	<1km to >5km	<1km to >5km
<b>Endurance</b>	H	H	L	H	H	H	H	L	H	H
<b>Real-time Payload Data</b>	No	No	No	Yes	Yes	Yes	No	Yes	Yes	Yes

It is worth noting that these operational conditions are strictly related to the range, which is classified into three classes: <1km, 1 km ÷ 5 km and >5 km. The other features are classified into three levels: Low (L), Medium (M) and High (H). Range and endurance are strictly connected, although the coverage of large areas can be performed within a low range, but requires high endurance. The landing accuracy depends on how, where, and when the mission is performed, requiring a high accuracy in case of a small landing area such as goods distribution hubs or a moving vehicle, and low or medium accuracy when landing can be

performed in large areas such as in the case of precision agriculture or mapping, leaving to VLOS or GNSS the possibility of recovering the aerial platform.

### **5.2.2.3. Features vs. equipment**

For each feature, the equipment that should be required, or might be required is identified, in terms of navigation systems, data links and systems to ensure the situational awareness. The result of this analysis is the compliance matrix presented in Table 19. The C2 data link is considered always present.

#### **A. Navigation Systems.**

- For high values of maximum range and BLOS operations, high-performance navigation systems (such as high-performance or barometric altimeter and airspeed sensor) should be required;
- High-performance navigation systems (such as advanced autopilot, advanced GNSS receiver and high-performance or barometric altimeter) should be required in case of medium and high risk missions. The use of redundant navigation units should be also required in high risk missions;
- To reduce the risk related to UAS interaction with manned aircraft, an advanced autopilot, an advanced GNSS receiver, high-performance or barometric altimeter and a redundant configuration of navigation units should be required;
- To reduce the risk related to the interaction with other UAS, an advanced autopilot, an advanced GNSS receiver and the barometric altimeter should be required.

#### **B. Data Link.**

- In case of BLOS operations, a communication network or SATCOM based link should be required;
- A redundant C2 data link and an encrypted/protected C2 data link is associated to high risk level;
- Payload data link is related to the necessity of real-time payload data, without a significant correlation with other aspects;
- An encrypted/protected C2 data link can also reduce the risks related to UAS interaction with manned aircraft.

Table 19. Features vs. equipment compliance matrix (● - necessary; ✓ - optional; no symbol indicates incompatibility).

		FEATURES																			
		Range			Operations			Mission Profile			Risk			Real-time Payload Data	Landing Accuracy			Interaction			
		<1km	1 km ÷ 5	>5 km	VLOS	BVLOS	BLOS	P2P	Area	Loiter	Low	Medium	High		Low	Medium	High	Human	Manned Traffic	Unmanned	
EQUIPMENT	Navigation	Manual control	✓			✓	✓		✓	✓	✓	✓	✓				✓	✓	✓		
		Low level autopilot	●	✓	✓	✓	✓		✓	✓	✓	●			✓	✓	✓	✓			
		Advanced autopilot		✓	✓	✓	✓	✓	✓	✓	✓	●	●		✓	✓	✓	✓	●	●	
		Standard GNSS receiver	●	●	●	●	●	●	●	●	●				●	✓		✓		✓	
		Augmented (SBAS/GBAS) GNSS receiver	✓	✓	✓	✓	✓	✓	✓	✓	✓	✓	✓	✓		✓	✓		✓	✓	
		RTK enabled GNSS receiver	✓	✓	✓	✓	✓	✓	✓	✓	✓	✓	✓	✓		✓	✓	✓	✓	✓	
		Advanced GNSS receiver (RAIM, Anti-jamming)	✓	✓	✓	✓	✓	✓	✓	✓	✓		●	●		✓	✓	✓	●	●	
		Optical Navigation Unit	✓	✓	✓	✓	✓	✓	✓	✓	✓	✓	✓	✓			✓	✓	✓	✓	
		High Performance Altimeter	✓	✓	●	✓	✓	●	✓	✓	✓	✓	✓	●		✓	✓	✓	✓	●	✓
		Ultrasonic altimeter	✓	✓	✓	✓	✓	✓	✓	✓	✓	✓	✓	✓		✓	✓	✓	✓	✓	
		Barometric altimeter	●	●	●	●	●	●	●	●	●	●	●	●		●	●	●	●	●	●
	Airspeed sensor	✓	✓	●	✓	●	●	✓	✓	✓	✓	✓	✓		✓	✓	✓	✓	✓		
	Multiple navigation units	✓	✓	✓	✓	✓	✓	✓	✓	✓		✓	●		✓	✓	✓	✓	●	✓	
	Data Link	Redundant C2 data link	✓	✓	✓	✓	✓	✓	✓	✓		✓	●		✓	✓	✓	✓	✓	✓	
		Encrypted/Protected C2 data link	✓	✓	✓	✓	✓	✓	✓	✓		✓	●	●	✓	✓	✓	✓	●	✓	
		Payload data link	✓	✓	✓	✓	✓	✓	✓	✓	✓	✓	✓		✓	✓	✓	✓	✓	✓	
		BLOS C2 data link (communication network or SATCOM based)		✓	✓		✓	●	✓	✓	✓	✓	✓		✓	✓	✓	✓	✓	✓	
	Situational Awareness and Decision Making	ADS-B		✓	●	✓	✓	●	✓	✓	✓	✓	●		✓	✓	✓	✓	●	✓	
		UAS Traffic monitoring system	✓	✓	●	✓	✓	✓	✓	✓		✓	●		✓	✓	✓	✓	✓	●	
		Terrain Awareness and Warning System (TAWS)	✓	✓	●		●	●	✓	✓		✓	✓	●		✓	✓	✓	✓	✓	
		Fixed obstacle sensors	✓	✓	●	✓	●	●	✓	✓	✓	✓	●		✓	✓	✓	●	✓	✓	
		Traffic Sensors	✓	✓	✓	✓	✓	✓	✓	✓		✓	●	✓	✓	✓	✓	✓	✓	✓	
		Autonomous Collision Avoidance	✓	✓	✓	✓	✓	●	✓	✓		✓	●	✓	✓	✓	✓	✓	✓	✓	
		Remotely Operated Collision Avoidance	✓	✓		✓	●	●	✓	✓		✓	●		✓	✓	✓	✓	✓	✓	
		Ground Based Sense and Avoid	✓	✓	✓	✓	✓	✓	✓	✓		✓	✓	✓		✓	✓	✓	✓	✓	
		Autonomous Landing	✓	✓	✓	✓	✓	✓	✓	✓	✓	✓	✓	●		✓	✓	●	✓	✓	
		Autonomous Takeoff	✓	✓	✓	✓	✓	✓	✓	✓	✓	✓	✓	✓		✓	✓	✓	✓	✓	
		Lost Link Safety Mode	●	●	●	●	●	●	✓	✓	✓	✓	✓	●		✓	✓	✓	✓	✓	
	Contingency Management	✓	●	●	✓	●	●	✓	✓	✓	✓	●	●		✓	✓	✓	✓	✓		
	Link to Traffic Infrastructure	✓	✓	✓	✓	✓	✓	✓	✓	✓	✓	✓	●		✓	✓	✓	✓	✓		

C. Situational Awareness.

- For high values of maximum range, BLOS operations and high risk level missions, several systems should be required, such as ADS-B (or ADS-B like), Terrain

Awareness and Warning System (TAWS), fixed obstacle sensors, lost link safety mode, contingency management systems and collision avoidance systems.

- Fixed obstacle sensors may reduce the risk related to UAS interaction with people, while ADS-B is the primary system associated with potential interaction with manned aircraft.

#### **5.2.2.4. Missions vs. equipment**

Previous considerations regarding the features characterizing different mission types, and the link between technologies and mission features, can be synthesized linking missions and related equipment. This is done in Table 20. The table points out equipment, which should be required, or might be required, for the different mission types. Since each mission category may actually include different cases, e.g. in terms of range/endurance and operating scenarios (consider local vs. long range infrastructure inspection), considerations on required equipment actually combine different cases. However, the table is useful to summarize how different needs are related to technological requirements.

Analysing the table, it is clear that packet delivery missions are among the ones that pose the most significant requirements regarding equipment, especially if carried out in urban environments. This derives from the fact that they couple different challenging aspects, such as long range, interaction with humans/UAS/manned traffic, flight in critical environments, end-to-end mission profile with possible landing in constrained areas, and 1-to-N high level control concepts. These needs impact all navigation requirements, with particular emphasis on integrity, continuity and availability, besides accuracy. As in other cases, manual control does not represent a required technology, and can indeed be impractical in this mission scenario. On the other hand, it is likely that consumer grade avionics (e.g., including low-cost and low-performance inertial units) will not fulfil mission needs. This derives mainly from requirements in terms of integrity and robustness. As an example, protection against spoofing/jamming will be needed in critical environments. Also, redundancy of inertial units will increase reliability in high risk environments. The need to land in relatively unprepared areas is such that optical navigation techniques can represent a key concept to be applied. As regards data link, encryption, redundancy, and the capability to exploit existing communication networks are important features. Finally, in terms of situational awareness and decision making, UAS delivery is likely to require an

ample spectrum of capabilities and systems. It may be noticed that goods delivery in lower risk environments, outside manned/unmanned traffic routes, may represent an easier case thus being a good candidate for first routine operations.

Technological needs of precision agriculture derive in part from the mission objectives. In particular, highly precise measurements or operations involving physical interaction with the crops, will likely require RTK enabled GNSS receivers and possibly high accuracy inertial systems. However, requirements in terms of navigation integrity and robustness with respect to GNSS dropouts and spoofing/jamming, and in terms of data link security, are significantly relaxed. At the same time, the operating environment has benign characteristics (low manned/unmanned traffic density) which reduces the need for autonomous situational awareness and decision making. Long range agriculture missions are likely to pose major requirements, while local operations will represent the easiest case.

Mapping missions may ask for high accuracy navigation, however their local nature relaxes other requirements. This is similar to local surveillance missions, though security aspects and related technologies play a major role in the latter case.

Law enforcement poses challenges in terms of situational awareness and decision making that are similar to packet delivery, due to the criticality of the operating environment. A difference is that take off and landing are likely to take place where the operator is, thus reducing the requested level of autonomy in these phases.

Infrastructure related operations also comprise local (e.g., bridge inspection) and long range (e.g., railway inspection) operations. Longer range missions will ask for more advanced technologies in terms of autonomy, contingency management and interaction with manned/unmanned traffic.

As regards aerial photography/cinematography, these missions have mostly a local nature which makes operations easier, though the operating environment (rural vs. urban) may pose significant safety and security requirements.

Communication relay based on small UAS is likely to be needed in disaster scenarios, where additional risks could be accepted based on the situation of emergency. However, possibly high traffic density will require proper surveillance and decision making levels.

Finally, search and rescue operations may pose challenges of different levels, depending on the environment where they are conducted.

Table 20. Missions vs. required equipment (● - necessary; ✓ - optional; no symbol indicates incompatibility).

EQUIPMENT	MISSION									
	Packet Delivery	Precision Agriculture	Mapping	Surveillance	Law Enforcement	Traffic Monitoring	Infrastructure Inspection	Aerial Photo	Communication Relay	Search and Rescue
<b>NAVIGATION</b>										
Manual control		✓	✓	✓	✓	✓	✓	✓		✓
Autopilot with low level inertial unit		●		●	●	●	●	●	●	●
Autopilot with advanced inertial unit	●	✓	●							
Standard GNSS receiver	●	●	●	●	●	●	●	●	●	●
Differential GNSS receiver		✓	●				●			
RTK enabled GNSS receiver		✓	●				●			
Antispoofing GNSS receiver	●			●	●	●	✓		●	
Optical Navigation Unit	●	✓					✓	✓		●
High Performance Altimeter	●		●		●					✓
Ultrasonic altimeter	●	●	●	✓	✓		✓			✓
Barometric altimeter	●	●	●	●	●	●	●	●	●	●
Airspeed sensor	●	●	●	●	●	●	✓	✓	●	●
Multiplication of navigation units	●			✓	●	●	✓	✓	✓	✓
<b>DATA LINK</b>										
C2 data link	●	●	●	●	●	●	●	●	●	●
Redundant C2 data link	●			✓	●	●	●		●	●
Encrypted/Protected C2 data link	●		●	●	●	●	●	●	●	●
Payload data link		✓		●	●	●	✓	●	●	●
BLOS C2 data link	✓	✓					✓			
Communication Network based C2 data link	●	✓	✓	✓	✓	✓	✓		✓	●
<b>Situational awareness</b>										
Cooperative Collision Avoidance System	●	●	✓	✓	●	●	✓	✓	●	●
TAWS	●	●			●	●	✓	✓	●	●
Fixed obstacle sensors	●	✓		✓	●	●	✓	✓	●	●
Traffic Sensors	●			✓	●	●	✓		●	●
<b>DECISION MAKING</b>										
Autonomous Collision Avoidance	●	✓		✓	●	●	✓	✓	●	✓
Remotely Operated Collision Avoidance	●	✓		✓	●	●	✓	✓	●	✓
Ground Based Collision Avoidance	●				●	●	✓		✓	✓
Autonomous Landing	●	✓			✓			✓		✓
Autonomous Takeoff	●	✓			✓			✓		✓
Lost Link Safety Mode	●	✓	✓	✓	●	●	●	✓	●	●
Contingency Management	●	✓	✓	✓	●	●	●	✓	●	●
Link to Traffic Infrastructure	●	✓	✓	✓	●	●	✓	✓	●	✓

### 5.2.3. System architecture

The tool architecture is presented in Figure 67, whereas Figure 68 illustrates the flow-chart that summarizes how the tool works. The details about packages are reported in the following subsections:

1. Reference packages (“Main” and “Data” packages);
2. “Input/Output” package;
3. “XML Data” package;
4. “Test” package;
5. “Scoring” package.

#### 5.2.3.1. Reference packages

- The “Main” package includes all the developed components;
- The “Data” package contains the mission requirements and the weather conditions defined by the user in the user-input interface, the regulations database and the compliance matrixes defined in the previous sections.

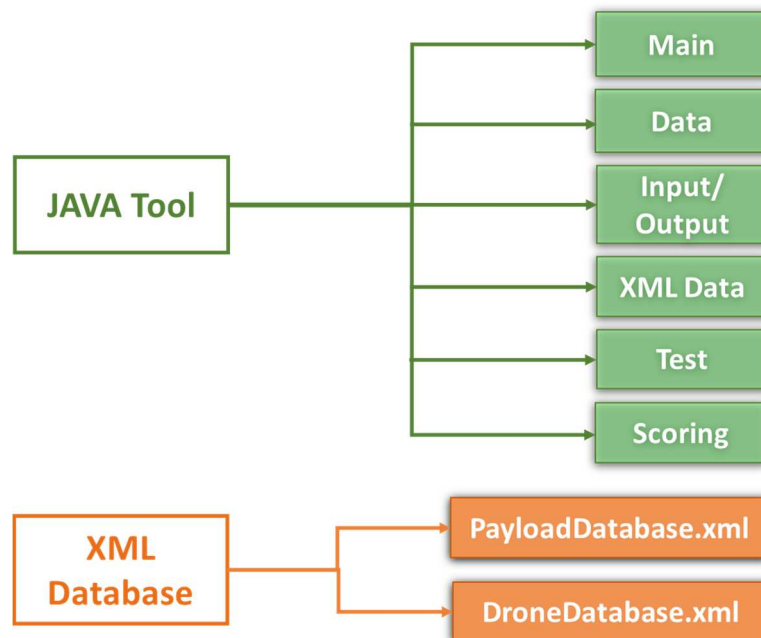


Figure 67. Tool Architecture.

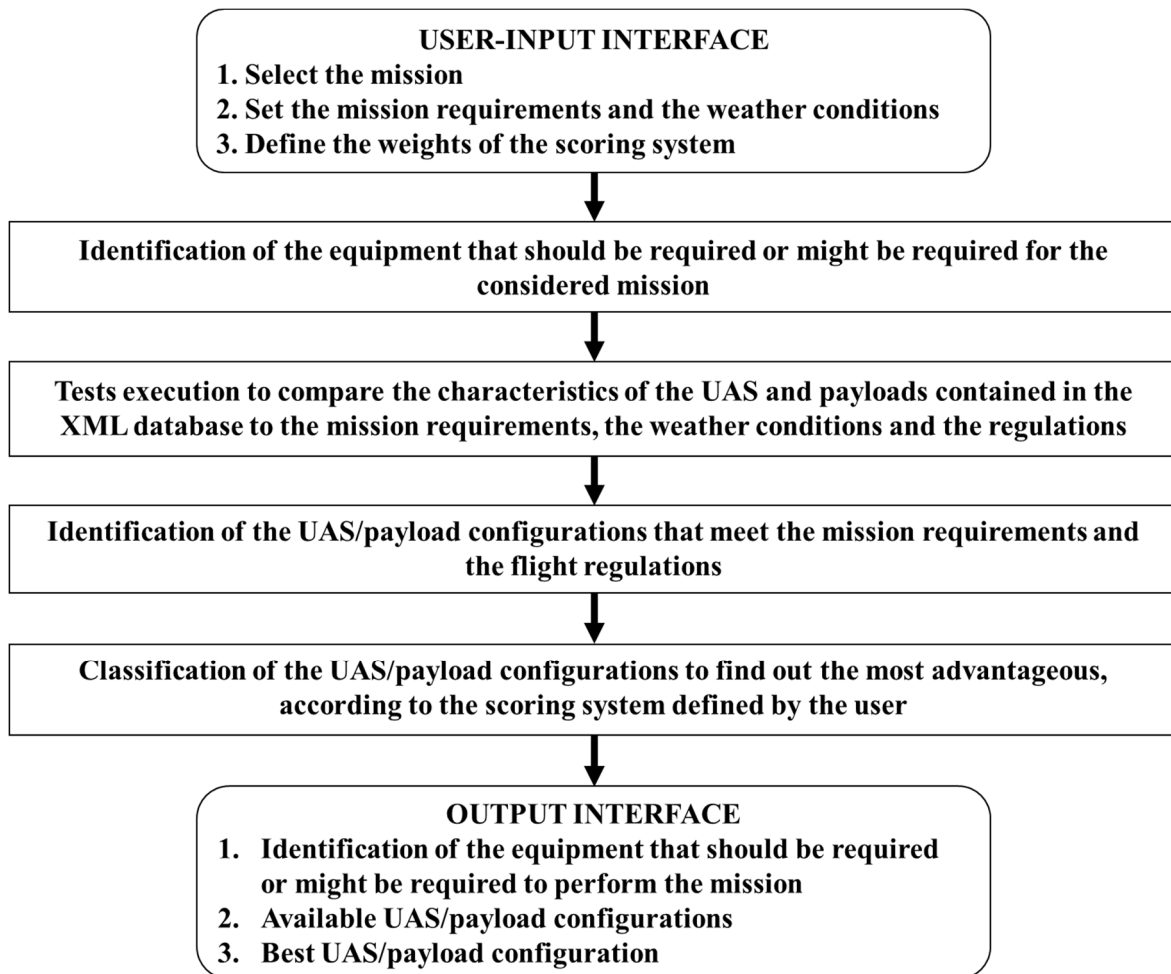


Figure 68. Flow-chart of the tool.

### **5.2.3.2. "Input/Output" package**

The "Input/Output" package generates the user-input interface and the output interface. The user-input interface (Figure 69) has been designed to improve the usage of the tool by proposing an ergonomic interface, in which the user can choose the type of mission, set the mission requirements and the weather conditions, and check the current regulations and the XML database. The mission requirements include indications about the maximum range of the mission, flight altitude, payload characteristics and if a GNSS-based autopilot is required. The user can also select the weights of the scoring system that classifies the UAS/payload configurations that meet the mission requirements, in order to select the most advantageous.

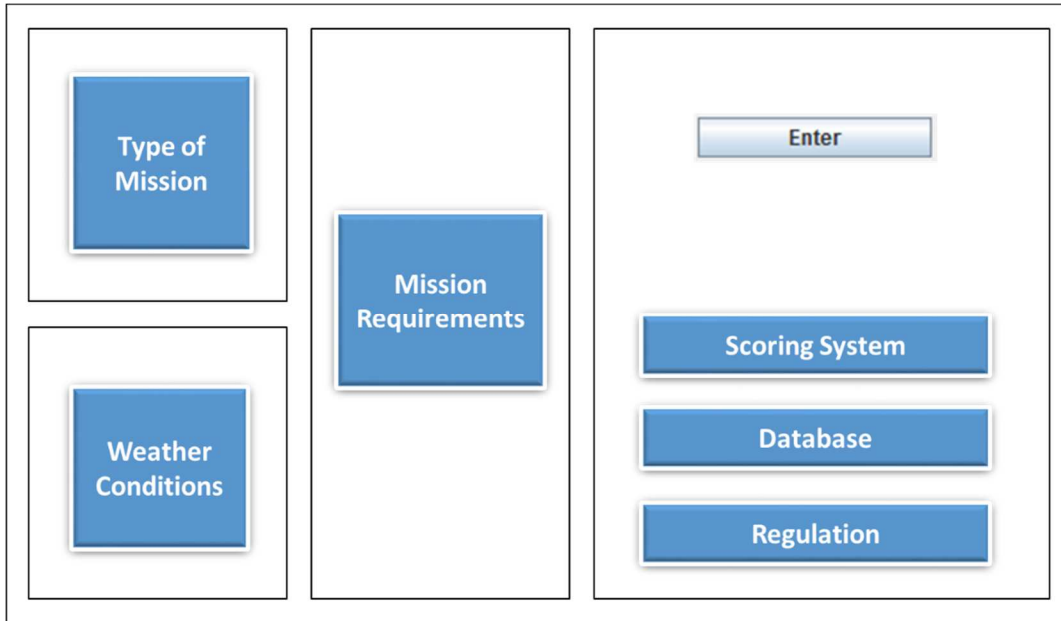


Figure 69. Layout of the user-input interface.

The output interface (Figure 70) presents:

1. The equipment required to perform the mission, in terms of navigation systems, data links, and systems to ensure the situational awareness;
2. The UAS and payload types that meet the mission requirements;
3. The list of available UAS/payload configurations, classified by using the scoring system.

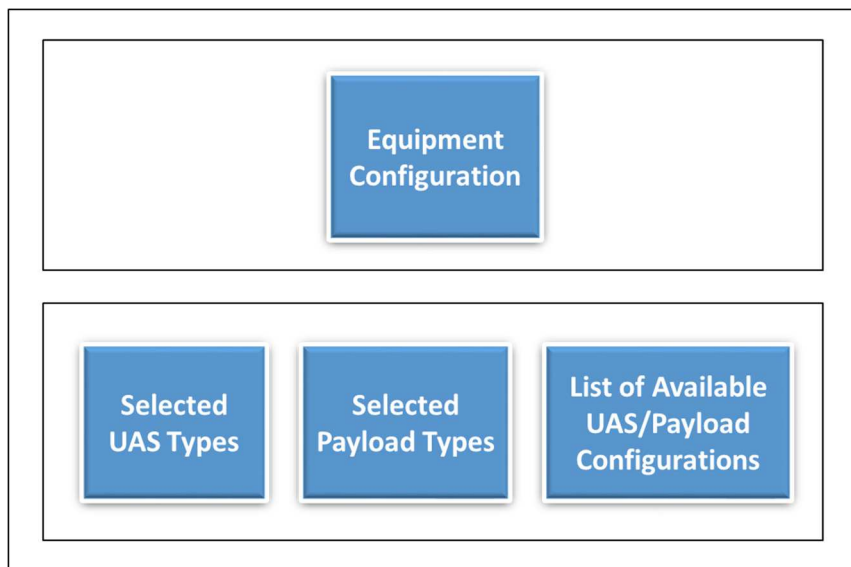


Figure 70. Layout of the output interface.

### 5.2.3.3. “XML Data” package

The “XML Data” package is linked to the XML databases, which have been organized to contain large amount of data and to facilitate the access by the user. They have been structured according to the following criteria: the name of the producer, the name of the device, characteristics (weight, price, etc.). Having data with a fixed format makes the tool faster and more accurate. Table 21 presents the structure of the XML databases. In the current version of the tool, only different types of camera are considered, being the most commonly adopted payload.

Table 21. Structure of the XML databases.

<b>UAS</b>	<b>Camera</b>
<i>Producer</i>	<i>Producer</i>
<i>Name</i>	<i>Name</i>
Cost	Cost
Wingspan	Type
Weight	Weight
Max Flight Time	Horizontal Field of View
Payload Capacity	Resolution Length
Max Speed	Resolution Width
Max Flying Altitude	
Max Operating Range	

### 5.2.3.4. “Test” package

The “Test” package performs tests aimed to select the best UAS/payload solutions, comparing the UAS and payload characteristics (contained in the databases) with the mission requirements, the current regulations and the weather conditions.

1. The first test compares the UAS maximum velocity with the wind speed. Indeed, to be able to fly and move in all directions, the relative velocity between the UAS and the wind must be positive (Figure 71).

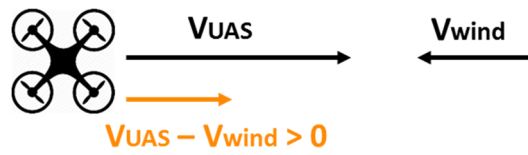


Figure 71. Test to compare the UAS maximum velocity ( $V_{UAS}$ ) with the wind velocity ( $V_{wind}$ ).

2. The second test compares the UAS endurance with the maximum distance to be covered during the mission. It takes into account the extra energy or fuel consumption due to the wind.
3. The third test compares the maximum altitude the UAS can reach during the flight with the altitude required to perform the mission.
4. The last test compares the relative UAS velocity with respect to the wind with the maximum velocity required to perform the mission.

Other tests are performed to check if the camera characteristics meet the requirements defined by the user (e.g. expected resolution, maximum size of the target).

1. The first test compares the Horizontal Field of View (HFOV) of the different types of camera included in the database with the required HFOV, computed as follows:

$$\alpha = 2\arctan\left(\frac{L}{2h}\right) \quad (60)$$

where  $\alpha$  is the HFOV required to cover the size of the target,  $L$  is the length of the target and  $h$  is the maximum altitude authorized by the current regulations (Figure 72).

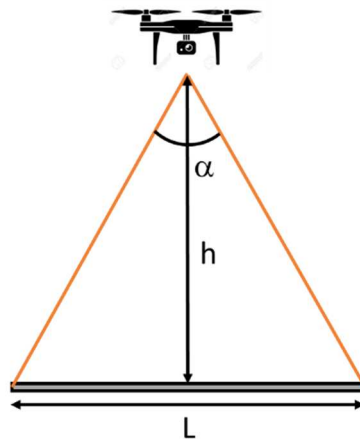


Figure 72. Required HFOV.

- The second test compares the desired ground resolution with the resolution of each camera included in the database at the maximum altitude allowed by the regulations.

The final test is aimed to retain only the UAS types with a payload capacity higher than the payload weight. Figure 73 synthetizes the procedure developed for the testing phase.

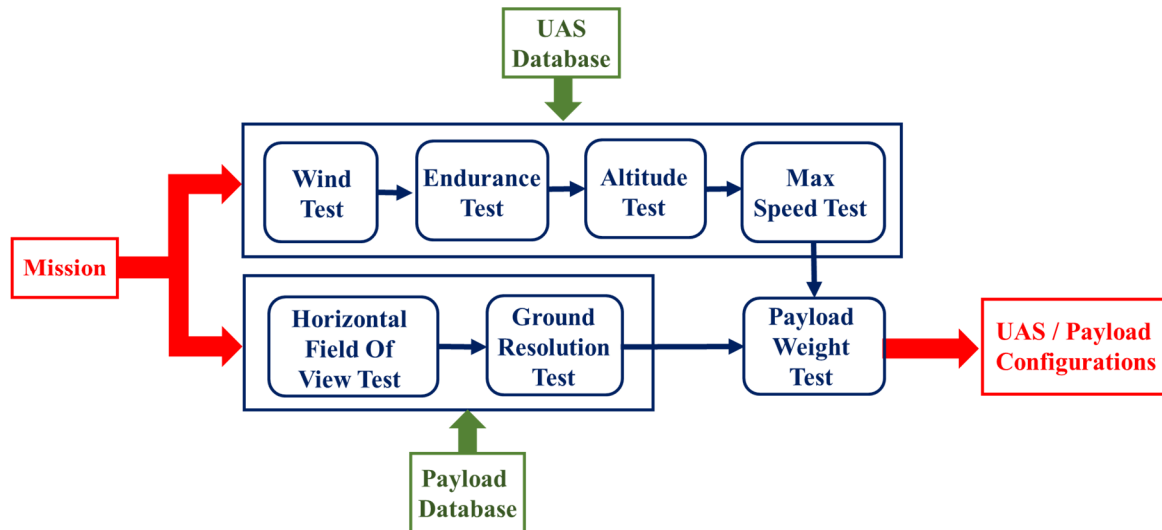


Figure 73. Flow-chart of the testing phase.

#### 5.2.3.5. “Scoring” package

The “Scoring” package automatically classifies the UAS/payload configurations that meet both the mission requirements and the current regulations, to select the most advantageous for the user. To each configuration, the tool assigns a score that depends on four parameters: the maximum endurance, the total weight and cost of the considered configuration and the angular resolution of the camera. The higher the score, the less the UAS/payload solution is close to the ideal configuration for the mission selected.

For each parameter, the user can select two reference terms (Figure 74), i.e. the target value and the maximum (or minimum) acceptable value. Thus, it is possible to define three ranges of values:

- Score = 0: the considered parameter meets the mission requirements;
- Score = 1: the considered parameter no longer meets the mission requirements;
- $0 < \text{Score} < 1$ : the considered parameter partially meets the mission requirements.

Finally, the tool assigns a weight to each score and then computes the weighted average. The weights can be defined by the user in the user-input interface.

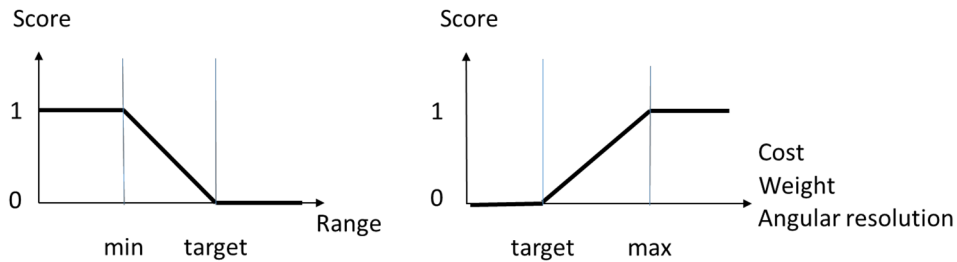


Figure 74. Scoring system transfer function.

#### 5.2.4. Application and results

Recently, the use of UAS equipped with small thermal, laser or spectral sensors has emerged as a promising alternative for assisting modelling, mapping and monitoring applications in rangelands, forests and agricultural environments (Salamí *et al.* 2014). Therefore, in this thesis, the mission considered to test the tool is the aerial photography of a field, by using a multispectral camera to obtain information (chlorophyll concentration, biomass monitoring) related to the productivity of the soil (Dickson *et al.* 2001; Navia *et al.* 2016; Von Bueren & Yule 2012).

As explained in the previous section, the user can set the mission requirements and the weather conditions in the user-input interface (Figure 75), check the current regulations and the XML database, by selecting respectively “Regulations” and “Open Database”, and define the weights of the scoring system, by selecting “Scoring System”.

Table 22 and Table 23 respectively present the mission requirements and the target and maximum (or minimum) values to be used in the scoring system. The parameters correspond to a realistic mission carried out at home location of authors. The best UAS/payload combinations are listed by considering the cost as the most important parameter.

The tool returns as output the equipment that should be required or might be required for the considered mission. The mandatory equipment is indicated with the “X” symbol in the output mask (Figure 76). All systems not indicated with “X” symbol can be considered as “suggested” rather than mandatory. Since the tool is linked to a database of existing subsystems, it also indicates the UAS and payload types that meet the mission requirements defined in the user-input interface. Finally, the tool classifies these solutions to find out the most advantageous. The 5 best UAS/payload configurations are listed in Table 24 . The total

score  $Score_{Total}$  is calculated as reported in Eq. (61). Being a combination of the scores related to each parameter (range, weight, cost and endurance),  $Score_{Total}$  can be higher than 1.

$$Score_{Total} = Score_{Range} + 0.75 \cdot Score_{Weight} + 1.25 \cdot Score_{Cost} + Score_{Resolution} \quad (61)$$

Table 22. Mission requirements (precision agriculture).

<b>Range</b>	1500 m
<b>Resolution</b>	0.05 m
<b>Image Size</b>	70 x 70 m
<b>Altitude</b>	50 m
<b>Imagery Type</b>	Multispectral
<b>Wind</b>	5 m/s
<b>Rain</b>	No
<b>Order by</b>	Cost
<b>GNSS autopilot</b>	Yes

Table 23. Target and maximum (or minimum) values for the scoring system (precision agriculture).

<b>Range</b>	Min: 1500 m Target: 5000 m
<b>Weight</b>	Target: 800 g Max: 1600 g
<b>Cost</b>	Target: 4000 \$ Max: 7000 \$
<b>Angular Resolution</b>	Target: 0.01° Max: 0.06°

Table 24. Best UAS/payload configurations (precision agriculture).

<b>UAS</b>	<b>Camera</b>	<b>Score<sub>Total</sub></b>
Phantom 4	Micro ADC	1.18
Hexacopter Hawk	Micro ADC	1.34
Phantom 4	Snap ADC	1.56
Based 1	Micro ADC	1.64
Phantom 3	Micro ADC	1.65

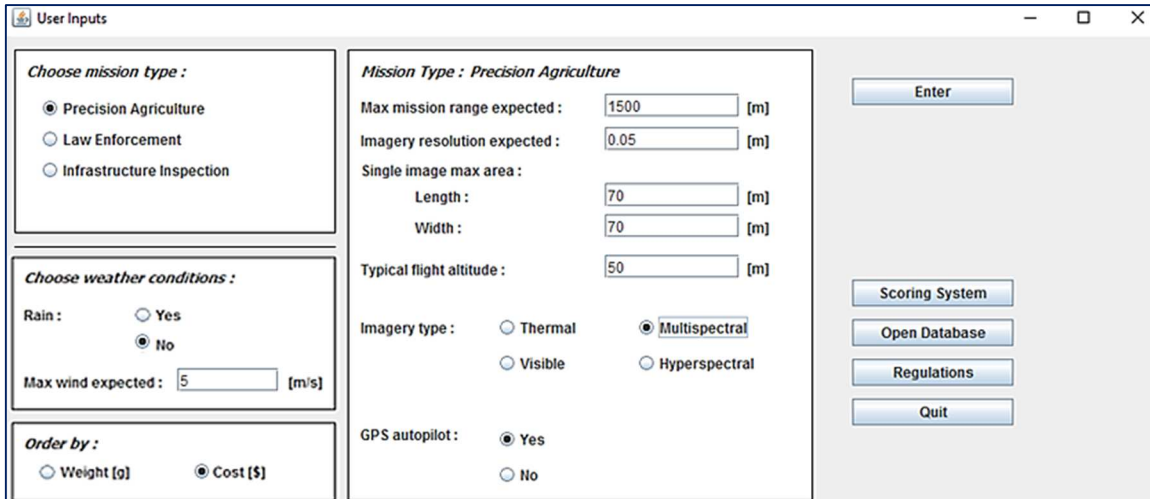


Figure 75. User-input interface (precision agriculture).

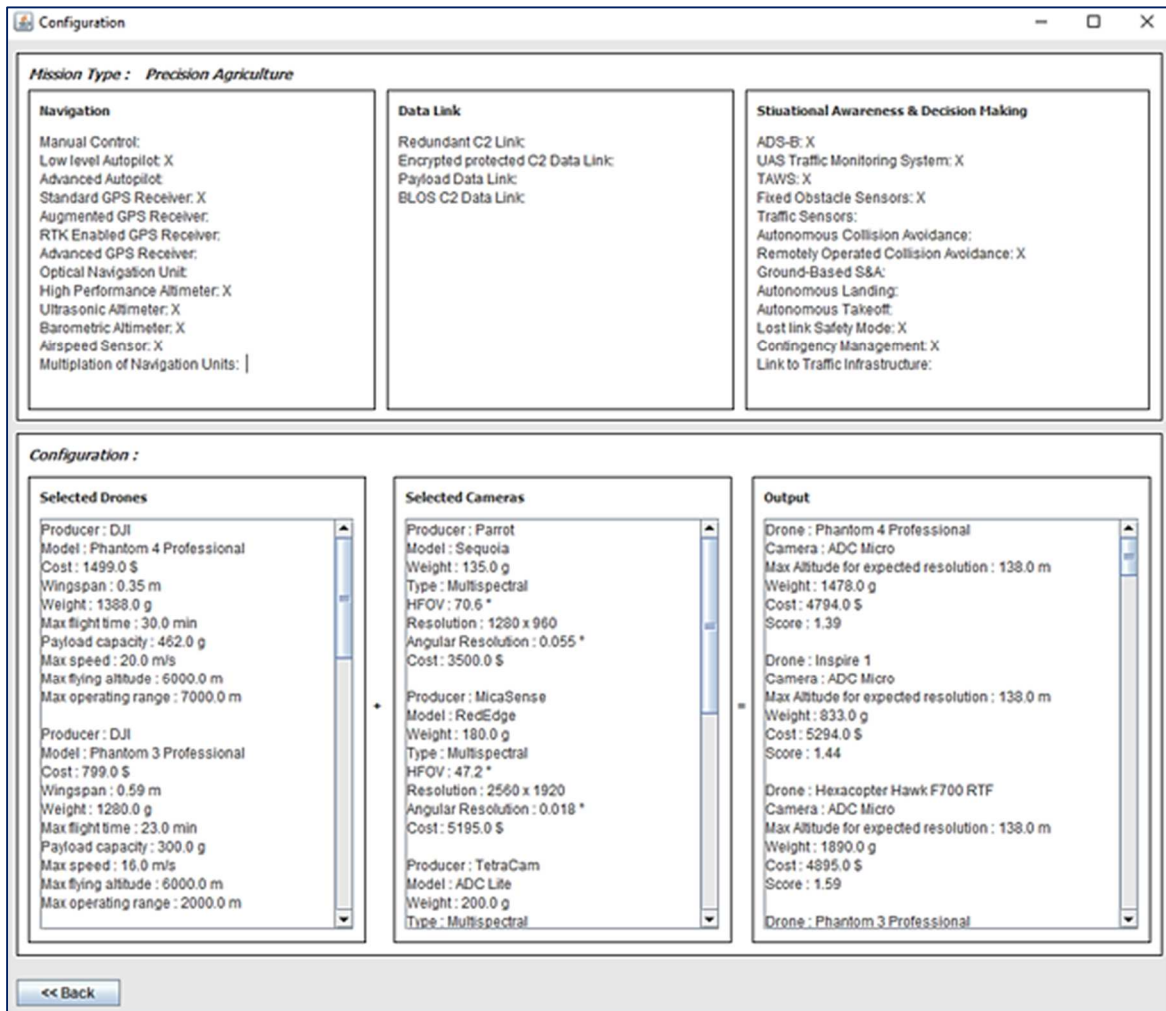


Figure 76. Output interface.

# Chapter 6

---

## Conclusions and Future Developments

The aim of this thesis was to support the safe integration of UAS operations, taking into account the user's requirements and flight regulations. The main technical and operational issues were identified, and two objectives were defined:

- A. Improving navigation performance of UAS by exploiting low-cost sensors. Two innovative calibration solutions were proposed to enhance the dead-reckoning performance of Micro Electro-Mechanical Systems inertial sensors for handling intermittent GNSS coverage in an integrated GNSS/MEMS-based inertial navigation solution;
- B. Proposing novel solutions for UAS mission management to support the Unmanned Traffic Management system in monitoring and coordinating the operations of a large number of UAS.

The findings related to each objective are discussed in the following sections and some suggestions for further research are proposed.

## **6.1. Improving navigation performance of UAS by exploiting low-cost sensors**

The thesis proposed two calibration methods for improving the dead-reckoning performance of MEMS gyros. The first one was the innovative Thermal Compensated Zero Velocity Update filter to estimate and compensate the inertial sensors bias. It is well-suitable for industrial grade gyros, which have significant limitations in terms of sensitivity to environmental conditions (Niu *et al.* 2013). The other method consisted in exploiting redundancy, which guaranteed a partial self-calibration of typical inertial sensors bias, reducing the uncertainty in attitude determination. It is well-suitable for consumer grades gyros, characterized by reduced weight, compact configuration, low power consumption and easy integration with electronic boards.

### **6.1.1. Thermal Compensated Zero Velocity Update filter**

The innovative Thermal Compensated Zero Velocity Update filter was proposed in this thesis to estimate and correct MEMS gyros bias, which drifts with temperature with a strongly non-linear trend (Niu *et al.* 2013).

It was compared with the traditional method, characterized by a cascading of two processing steps. The first step consisted in performing tests in a climatic chamber over the requested temperature intervals, in order to derive the calibration function (by exploiting the polynomial fitting technique) to allow the correction of bias thermal drift during the real-time operation of the unit (Wang *et al.* 2010). The second step consisted in a further reduction of bias that can be realized by estimating its residual amount by exploiting the Zero Velocity Update filter.

The proposed Thermal Compensated Zero Velocity Update filter, instead, embedded the compensation of thermal effect on bias in the filter itself and used Back-Propagation Neural Networks to build the calibration function.

The standard and innovative method were tested by exploiting the Attitude and Heading Reference System Axitude AX1-[]<sup>TM</sup> experimental data, in two conditions, i.e. 1) nominal condition, and 2) residual bias after rough initial alignment of 15 degrees/h (Earth's angular

rate) which was compatible with industrial grade gyros performance. The TCZUPT filter presented several advantages over the traditional method:

1. No calibration pre-processing stage was required to keep measurement drift under control, reducing the computational burden of the IMU processing software and improving its accuracy, reliability, and maintainability;
2. It accounted for the deterministic effect of temperature variations on bias drift, increasing the accuracy of bias estimation. In the standard ZUPT, instead, this effect was accounted by calibration processing and the residual uncertainty was included in the overall random uncertainty on bias determination;
3. It exploited Back-Propagation Neural Networks, that, being self-adaptive in constructing a mathematical model after several repetitive learning and testing phases, guaranteed better performance on mapping the highly non-linear bias trend with temperature than traditional polynomial fitting;
4. Since the TCZUPT filter was not based on direct correction of thermal bias (as the standard ZUPT filter), but on the estimation of the derivative of bias as a function of temperature:
  - It was faster in mapping significant bias variations. This is an important result for many applications that require a very fast ZUPT process, like missile systems;
  - The TCZUPT filter presented better performance in the overall testing period. This result can be useful in the case of stationary condition for long timeframe, e.g., the aircraft in parking stall for a time longer than the usual in a sunny day.

### **6.1.2. Redundant configuration of MEMS inertial sensors**

A high-performance and low-cost calibration solution for consumer grade MEMS gyros was proposed in this thesis. It exploited a redundant configuration of sensors. The proposed calibration solution was tested by exploiting the world's densest sensor board, the SensorTile™, by STMicroelectronics™. In particular, a redundant IMU prototype was designed and realized by using six SensorTiles™ in a cubic configuration.

By assembling a set of inertial sensors with a certain designed configuration, the redundancy of each axis in the navigation framework was efficiently improved, as well as

the accuracy of the whole IMU. Indeed, the IMU was able to make full use of the redundant observation data of these sensors, by averaging multiple measurements about the same axis.

Results showed that the adoption of a redundant IMU geometry allowed for a partial self-calibration of typical inertial sensors biases, reducing the uncertainty in attitude determination.

## **6.2. Novel solutions for UAS mission management**

This thesis proposed two solutions to support the Unmanned Traffic Management system in monitoring and coordinating the operations of a large number of UAS, speeding up the flight authorization process, and supporting the increasing level of autonomy in UAS operations. These solutions were developed by considering weight, size, power consumptions and economic limitations, and the diversity in UAS types, configurations and operational objectives.

The first solution was a trajectory prediction tool, aimed at supporting the UTM system in predicting UAS separation and collision threats within a safe time-frame. The second solution was a JAVA tool, aimed at supporting standardized procedures for decision-making process in order to identify UAS types, payload, and prescriptions adequate for any type of missions that can be authorized standing flight regulations.

### **6.2.1. Trajectory prediction**

This thesis proposed a trajectory prediction tool for small UAS, based on Learning Vector Quantization Neural Networks. First of all, the trajectory model implemented in the LVQ Neural Network was described. It consisted in the discretization of a generic trajectory in a certain number of elements, characterized by three representative features: the angle between the two segments that compose each trajectory element, the wind direction and the wind speed.

Subsequently, for each feature, a certain number of classes was selected as a trade-off between the required accuracy and the processing loads and by considering the symmetry of the problem. Finally, experimental tests were performed by flying the DJI Phantom 4<sup>TM</sup> in waypoint mode and telemetry data acquired in real-time were used to train and test the LVQ Neural Networks.

Results showed that, by exploiting flight data collected when the Phantom 4™ executed a pre-assigned flight path, the tool was able to predict the time taken to fly generic trajectory elements. Moreover, being self-adaptive in constructing a mathematical model after several training and testing steps, LVQ Neural Networks allow creating different models for the myriad of different UAS types in several environmental conditions.

### **6.2.2. Standardized procedures for decision-making**

The thesis proposed a software tool, aimed at supporting standardized procedures for decision-making process in order to identify UAS types, payload, and prescriptions suitable for any type of missions that can be authorized standing flight regulations.

The tool was developed in JAVA and it was linked to an external eXtensible Markup Language database composed by several UAS and payload types, organized in a dataset easily usable by the tool. The XML database can be stored on a different server and updated online, considering all new technologies that will be developed with time, making the tool able to adapt to the UAS ever-changing scenario, characterized by a high tendency to automation, the continuous development of new technologies and the evolution of regulations.

The mission considered to test the tool was the aerial photography of a field, by using a multispectral camera to obtain information (chlorophyll concentration, biomass monitoring) related to the productivity of the soil. By setting the mission requirements and the weather conditions in the user-input interface, the tool identified the required and recommended on-board equipment and suggested off-the-shelf solutions to realize the customer needs, in terms of hardware (e.g. UAS frame-structure and payload characteristics) and prescriptions (e.g. weight and cost), taking into account the current regulations. Furthermore, by using a scoring system defined by the user in the input interface, the tool classified the available UAS / payload configurations, selecting the most suitable to the considered mission.

## **6.3. Future developments**

The findings of this thesis identify some potential areas of research to explore:

- Investigating the TCZUPT filter performance when the gyro bias is affected by hysteresis. Indeed, the presence of hysteresis due to successive heating and

cooling cycles (Gulmammadov 2009) causes an additive bias. In other words, for each value of temperature the hysteresis branches have different offset but often almost identical derivative as a function of temperature. While the traditional ZUPT filter adopts the transfer function as a fixed reference, the TCZUPT filter exploits the derivative of the calibration transfer function with temperature, which tends to be constant on the different branches that form the hysteresis loop (Gulmammadov 2009). Therefore, while the standard ZUPT filter can correct only a branch of the hysteresis loop, the TCZUPT filter have the potential to correct all the branches of the hysteresis loop;

- Exploiting a Kalman filter-based data fusion technique to integrate multiple measurements of the redundant IMU about the same axis. The Kalman filter can be performed by a concentrator (one of the six SensorTiles™ or an external microcontroller);
- Exploiting deep learning for trajectory prediction. Indeed, compared to traditional machine learning, deep learning does not have a "plateau in performance" i.e. the more data they are given, the better it would perform (LeCun *et al.* 2015);
- Exploiting the novel solutions for UAS mission management to:
  1. Support the future Mission Manager system for UAS (Royo *et al.* 2013) in assessing a broad range of mission-level conditions;
  2. Aid the on-board Sense & Avoid system (Fasano *et al.* 2016b) in defining the optimal avoidance manoeuvre, by exploiting future trajectories predictions of surrounding traffic;
  3. Support mutual tracking of UAS swarms by cooperative navigation systems (Leonard *et al.* 2012; Vetrella *et al.* 2015a);
  4. Improve UAS mission surveillance, which is a relevant technology to enable safe UAS application (FAA 2018);
  5. Support the flight termination system, utilized as a last resort to bring down an UAS expeditiously in order to maintain some level of safety to the public or property (Santamaria *et al.* 2009)(Stansbury *et al.* 2009).

## 6.4. Publications and awards

The following journal papers have been produced to support this research:

- R. Fontanella, D. Accardo, R. Schiano Lo Moriello, L. Angrisani, D. De Simone, An Innovative Strategy for Accurate Thermal Compensation of Gyro Bias in Inertial Units by Exploiting a Novel Augmented Kalman Filter, *Sensors (Basel, Switzerland)*, **2018**, Vol. 18, n. 5, doi: 10.3390/s18051457.
- R. Fontanella, D. Accardo, R. Schiano Lo Moriello, L. Angrisani, D. De Simone, MEMS Gyros Temperature Calibration through Artificial Neural Networks, *Sensors and Actuators A: Physical*, **2018**, Vol. 279, pp. 553-565, doi: 10.1016/j.sna.2018.04.008.

In addition, the following conference proceedings have been produced:

- R. Fontanella, G. de Alteriis, D. Accardo, R. Schiano Lo Moriello, L. Angrisani, Advanced Low-Cost Integrated Inertial Systems with Multiple Consumer Grade Sensors, *37th AIAA/IEEE Digital Avionics Systems Conference, DASC*, London, UK, **2018**.
- R. Fontanella, F. Buonavolontà, R. Schiano Lo Moriello, D. Accardo, L. Angrisani, Exploiting Low-Cost Compact Sensor Configurations Performance by Redundancy, *AIAA Information Systems-AIAA Infotech, AIAA SciTech Forum*, Kissimmee, Florida, **2018**, doi: 10.2514/6.2018-0194.
- R. Fontanella, A. R. Vetrella, G. Fasano, D. Accardo, A Solution for Trajectory Prediction of Small Unmanned Aircraft by Exploiting Artificial Neural Networks, *RAeS Modelling and Simulation in Flight Simulation Conference*, London, UK, **2017**.
- R. Fontanella, A. R. Vetrella, G. Fasano, D. Accardo, R. Schiano Lo Moriello, L. Angrisani, R. Girard, A Standardized Approach to Derive System Specifications for Drones Operating in the Future UTM Scenario, *5th IEEE International Conference on Models and Technologies for Intelligent Transportation Systems, MT-ITS*, Naples, Italy, **2017**, pp. 250-255, doi: 10.1109/MTITS.2017.8005675.

- R. Fontanella, D. Accardo, E. Caricati, S. Cimmino, D. De Simone, Improving Inertial Attitude Measurement Performance by Exploiting MEMS Gyros and Neural Thermal Calibration, *AIAA Information Systems-AIAA Infotech, AIAA SciTech Forum*, Grapevine, Texas, **2017**, doi: 10.2514/6.2017-1134.
- R. Fontanella, A. R. Vetrella, G. Fasano, D. Accardo, R. Schiano Lo Moriello, L. Angrisani, Requirements, Platform Specifications, and System Architectures for Future Unmanned Traffic Management Systems, *AIAA Information Systems-AIAA Infotech, AIAA SciTech Forum*, Grapevine, Texas, **2017**, doi: 10.2514/6.2017-0225.
- R. Fontanella, D. Accardo, E. Caricati, S. Cimmino, D. De Simone, An Extensive Analysis for the Use of Back Propagation Neural Networks to Perform the Calibration of MEMS Gyro Bias Thermal Drift, *IEEE/ION Position, Location and Navigation Symposium, PLANS*, Savannah, Georgia, **2016**, pp. 672-680, doi: 10.1109/PLANS.2016.7479760.

Finally, the author, member of the UNINA team, was awarded for the Special Mention at the IEEE International Sensors and Measurement Systems Student Contest, IEEE I2MTC 2018, Houston, TX, USA, (14-17 May 2018) for the project named “*POLYTILE: Self-Compensating IMU Exploiting Redundant Configuration on Regular POLYhedron of SensorTILES*”.

# References

- Airbus. (2018). *Blueprint UTM roadmap*.
- Albani, D., Nardi, D., & Trianni, V. (2017). Field coverage and weed mapping by UAV swarms. In *IEEE International Conference on Intelligent Robots and Systems*. doi:10.1109/IROS.2017.8206296
- Amaro Carmona, M. A., Rudinskas, D., & Barrado, C. (2015). Design of a flight management system to support four-dimensional trajectories. *Aviation*, **19**(1), 58–65.
- Amazon.com Inc. (2015). *Determining Safe Access with a Best-Equipped, Best-Served Model for Small Unmanned Aircraft Systems*. *NASA UTM 2015: The Next Era of Aviation*.
- Atkins, E. M., & Di Donato, P. F. A. (2016). Chapter 36. In *Unmanned aircraft systems*, John Wiley & Sons.
- Austin, R. (2010). *Unmanned Aircraft Systems: UAVS Design, Development and Deployment*, John Wiley & Sons.
- Barbour, N. (2010). *Inertial navigation sensors*. *NATO RTO Lecture Series*.
- Barbour, N. M., Hopkins, R., & Kourepenis, A. (2011). *Inertial MEMS Systems and Applications*. *NATO Lecture Series*.
- Barrado, C., Ramírez, J., Pérez-Batlle, M., Santamaria, E., Prats, X., & Pastor, E. (2013). Remote Flight Inspection Using Unmanned Aircraft. *Journal of Aircraft*, **50**(1), 38–46.
- Bhatt, D., Aggarwal, P., Bhattacharya, P., & Devabhaktuni, V. (2012). An enhanced MEMS error modeling approach based on Nu-Support vector regression. *Sensors (Switzerland)*, **12**(7), 9448–9466.
- Bhatti, U. I., Ochieng, W. Y., & Feng, S. (2007). Integrity of an integrated GPS/INS system in the presence of slowly growing errors. Part I: A critical review. *Gps Solutions*, **11**(3), 173–181.
- Brenner, M. (1995). Integrated GPS/Inertial Fault Detection Availability. In *ION GPS-95*, Palm Springs, CA, USA.
- Broggi, A., Buzzoni, M., Debattisti, S., ... Versari, P. (2013). Extensive tests of autonomous

- driving technologies. *IEEE Transactions on Intelligent Transportation Systems*, **14**(3), 1403–1415.
- Bruch, M., Gilbreath, G., Muelhauser, J., & Jq, L. (2002). Accurate waypoint navigation using nondifferential GPS. In *AUVSI Unmanned Systems*.
- CAAC. (2018). *UOMS in China*.
- Cai, G., Chen, B. M., & Lee, T. H. (2011). Coordinate Systems and Transformations. In *Unmanned Rotorcraft Systems*, Springer, London.
- Castillo-Effen, M., Ren, L., Yu, H., & Ippolito, C. A. (2017). Off-nominal trajectory computation applied to unmanned aircraft system traffic management. In *AIAA/IEEE Digital Avionics Systems Conference Proceedings*. doi:10.1109/DASC.2017.8102075
- Cheng, J., Dong, J., Landry, R., & Chen, D. (2014). A novel optimal configuration form redundant MEMS inertial sensors based on the orthogonal rotation method. *Sensors (Switzerland)*, **14**(8), 13661–13678.
- Cuadrado, R., Royo, P., Barrado, C., Pérez, M., & Pastor, E. (2013). Architecture issues and challenges for the integration of rpas in non-segregated airspace. In *AIAA/IEEE Digital Avionics Systems Conference - Proceedings*. doi:10.1109/DASC.2013.6712622
- Cui, J., Chi, X. Z., Ding, H. T., Lin, L. T., Yang, Z. C., & Yan, G. Z. (2009). Transient response and stability of the AGC-PI closed-loop controlled MEMS vibratory gyroscopes. *Journal of Micromechanics and Microengineering*, **19**(12). doi:10.1088/0960-1317/19/12/125015
- D'Souza, S., Ishihara, A., Nikaido, B., & Hasseeb, H. (2016). Feasibility of varying geofence around an unmanned aircraft operation based on vehicle performance and wind. In *AIAA/IEEE Digital Avionics Systems Conference - Proceedings*. doi:10.1109/DASC.2016.7777987
- D'Souza, S. N. (2017). Developing a Generalized Trajectory Modeling Framework for Small UAS Performance in the Presence of Wind. In *AIAA Information Systems-AIAA Infotech @ Aerospace*. doi:10.2514/6.2017-0447
- de Pasquale, G., & Somà, A. (2010). Reliability testing procedure for MEMS IMUs applied to vibrating environments. *Sensors*, **10**(1), 456–474.
- Degarmo, M. T. (2004). *Issues Concerning Integration of Unmanned Aerial Vehicles in Civil Airspace*. Center for Advanced Aviation System Development, The MITRE Corporation.

- Dickson, M. A., Hendrickson, L. L., & Reid, J. F. (2001). Multi-spectral imaging sensor, Google Patents.
- Diebel, J. (2006). Representing attitude: Euler angles, unit quaternions, and rotation vectors. *Matrix*, **58**, 1–35.
- Diesel, J., & King, J. (1995). Integration of navigation systems for fault detection, exclusion, and integrity determination-Without WAAS. In *Institute of Navigation, National Technical Meeting*, Anaheim, CA, pp. 683–692.
- DJI. (2018). *PHANTOM 4 Release Notes*.
- Doukhi, O., Fayjie, A. R., & Lee, D. J. (2017). Intelligent Controller Design for Quad-Rotor Stabilization in Presence of Parameter Variations. *Journal of Advanced Transportation*, 1–10.
- Duc-tan, T., Fortier, P., & Huynh, H. (2011). Design , Simulation , and Performance Analysis of an INS / GPS System using Parallel Kalman Filters Structure, **1**(2), 88–96.
- El-Diasty, M., El-Rabbany, A., & Pagiatakis, S. (2007). Temperature variation effects on stochastic characteristics for low-cost MEMS-based inertial sensor error. *Measurement Science and Technology*, **18**(11), 3321–3328.
- Elias, B. (2012). *Pilotless Drones: Background and Considerations for Congress Regarding Unmanned Aircraft Operations in the National Airspace System*.
- Elwenspoek, M., & Wiegerink, R. (2012). *Mechanical Microsensors*, Springer Science & Business Media. doi:10.1088/0957-0233/12/9/704
- European Aviation Safety Agency. (2015a). *A-NPA 2015-10, Introduction of a regulatory framework for the operation of drones*.
- European Aviation Safety Agency. (2015b). *Opinion of a technical nature, Introduction of a regulatory framework for the operation of unmanned aircraft*.
- European Aviation Safety Agency. (2018). *Opinion No 01/2018, Introduction of a regulatory framework for the operation of unmanned aircraft systems in the ‘open’ and ‘specific’ categories*.
- FAA. (2012). *TSO-C201, Technical Standard Order*, Washington D.C.
- FAA. (2013a). *Integration of Civil Unmanned Aircraft Systems (UAS) in the National Airspace System (NAS) Roadmap*.
- FAA. (2013b). *NextGen Implementation Plan*.
- FAA. (2015). *Overview of Small UAS Notice of Proposed Rulemaking*.

- FAA. (2018). *UTM Concept of Operations - v1.0*.
- Fahlstrom, P. G., & Gleason, T. J. (2012). *Introduction to UAV Systems*, 4th edn, John Wiley & Sons. doi:10.1002/9781118396780
- Faruqi, F. A. (2016). Chapter 18. In *Unmanned aircraft systems*, John Wiley & Sons.
- Fasano, G., Accardo, D., & Moccia, A. (2016a). Chapter 22. In *Unmanned Aircraft Systems*, John Wiley & Sons.
- Fasano, G., Accardo, D., Moccia, A., & Maroney, D. (2016b). Sense and avoid for unmanned aircraft systems. *IEEE Aerospace and Electronic Systems Magazine*. doi:10.1109/MAES.2016.160116
- Fasano, G., Forlenza, L., Tirri, A. E., Accardo, D., & Moccia, A. (2011). Multi-sensor data fusion: A tool to enable UAS integration into civil airspace. In *AIAA/IEEE Digital Avionics Systems Conference - Proceedings*. doi:10.1109/DASC.2011.6096082
- Feng, S., Ochieng, W., Samson, J., ... Jofre, M. (2012). Integrity monitoring for carrier phase ambiguities. *Journal of Navigation*, **65**(1), 41–58.
- Feng, S., Ochieng, W. Y., Walsh, D., & Ioannides, R. (2006). A measurement domain receiver autonomous integrity monitoring algorithm. *GPS Solutions*, **10**(2), 85–96.
- Foina, A. G., Krainer, C., & Sengupta, R. (2015). An Unmanned Aerial Traffic Management solution for cities using an air parcel model. In *2015 International Conference on Unmanned Aircraft Systems, ICUAS 2015*, pp. 1295–1300.
- Fong, W. T., Ong, S. K., & Nee, A. Y. C. (2008). Methods for in-field user calibration of an inertial measurement unit without external equipment. *Measurement Science and Technology*, **19**(8). doi:10.1088/0957-0233/19/8/085202
- Fontanella, R., Accardo, D., Caricati, E., Cimmino, S., & De Simone, D. (2016). An extensive analysis for the use of back propagation neural networks to perform the calibration of MEMS gyro bias thermal drift. In *Proceedings of the IEEE/ION Position, Location and Navigation Symposium, PLANS 2016*, pp. 672–680.
- Fontanella, R., Accardo, D., Caricati, E., Cimmino, S., De Simone, D., & Lucignano, G. (2017a). Improving Inertial Attitude Measurement Performance by Exploiting MEMS Gyros and Neural Thermal Calibration. In *AIAA Information Systems-AIAA Infotech @ Aerospace*, American Institute of Aeronautics and Astronautics. doi:10.2514/6.2017-1134
- Fontanella, R., Accardo, D., Lo Moriello, R. S., Angrisani, L., & De Simone, D. (2018a).

- An innovative strategy for accurate thermal compensation of Gyro Bias in inertial units by exploiting a novel Augmented Kalman Filter. *Sensors (Switzerland)*, **18**(5). doi:10.3390/s18051457
- Fontanella, R., Accardo, D., Lo Moriello, R. S., Angrisani, L., & De Simone, D. (2018b). MEMS Gyros Temperature Calibration through Artificial Neural Networks. *Sensors and Actuators A: Physical*, **279**, 553–565.
- Fontanella, R., Bonavolontà, F., Schiano Lo Moriello, R., Accardo, D., & Angrisani, L. (2018c). Exploiting low-cost compact sensor configurations performance by redundancy. In *AIAA Information Systems-AIAA Infotech at Aerospace, 2018*. doi:10.2514/6.2018-0194
- Fontanella, R., Vetrella, A. R., Fasano, G., & Accardo, D. (2017b). A Solution for Trajectory Prediction of Small Unmanned Aircraft by Exploiting Artificial Neural Networks. In *RAeS Modelling and Simulation in Flight Simulation Conference*.
- Fontanella, R., Vetrella, A. R., Fasano, G., Accardo, D., Rosario, S. L. M., & Angrisani, L. (2017c). Requirements, Platform Specifications, and System Architectures for Future Unmanned Traffic Management Systems. In *AIAA Information Systems-AIAA Infotech @ Aerospace*. doi:10.2514/6.2017-0225
- Fontanella, R., Vetrella, A. R., Fasano, G., ... Girard, R. (2017d). A standardized approach to derive system specifications for drones operating in the future UTM scenario. In *5th IEEE International Conference on Models and Technologies for Intelligent Transportation Systems, MT-ITS 2017 - Proceedings*. doi:10.1109/MTITS.2017.8005675
- Francis, M. S. (2016). Chapter 1. In *Unmanned aircraft systems*, John Wiley & Sons.
- Gardi, A., Ramasamy, S., & Sabatini, R. (2015). 4-dimensional trajectory generation algorithms for RPAS Mission Management Systems. In *2015 International Conference on Unmanned Aircraft Systems, ICUAS 2015*. doi:10.1109/ICUAS.2015.7152314
- Gautier, J. D. (2003). *GPS/INS generalized evaluation tool (GIGET) for the design and testing of integrated navigation systems*, Stanford University.
- Gelb, A. (1974). *Applied optimal estimation*, MIT press.
- Gleason, T. J., & Fahlstrom, P. (2016). Chapter 6. In *Unmanned aircraft systems*, John Wiley & Sons.
- GMA. (2018). Attitude & Heading Reference System (AX1-[ ]).

- Gold, K. L., & Brown, A. K. (2004). A hybrid integrity solution for precision landing and guidance. In *Position Location and Navigation Symposium, PLANS 2004*. doi:10.1109/PLANS.2004.1308990
- Gross, J., Gu, Y., Gururajan, S., Seanor, B., & Napolitano, M. (2010a). A Comparison of Extended Kalman Filter, Sigma-Point Kalman Filter, and Particle Filter in GPS/INS Sensor Fusion. In *AIAA Guidance, Navigation, and Control Conference*, American Institute of Aeronautics and Astronautics. doi:10.2514/6.2010-8332
- Gross, J., Gu, Y., & Napolitano, M. (2010b). A Systematic Approach for Extended Kalman Filter Tuning and Low-Cost Inertial Sensor Calibration within a GPS/INS Application. In *AIAA Guidance, Navigation, and Control Conference*, American Institute of Aeronautics and Astronautics. doi:10.2514/6.2010-7759
- Gross, J., Gu, Y., Rhudy, M., Barchesky, F., & Napolitano, M. (2011). On-line Modeling and Calibration of Low-Cost Navigation Sensors. In *AIAA Modeling and Simulation Technologies Conference*, American Institute of Aeronautics and Astronautics. doi:10.2514/6.2011-6332
- Gross, J. N., Gu, Y., Rhudy, M. B., Gururajan, S., & Napolitano, M. R. (2012). Flight-test evaluation of sensor fusion algorithms for attitude estimation. *IEEE Transactions on Aerospace and Electronic Systems*. doi:10.1109/TAES.2012.6237583
- Groves, P. D. (2013). *Principles of GNSS, Inertial, and Multisensor Navigation Systems*, 2nd edn, Artech House Publishers.
- Gulmammadov, F. (2009). Analysis, modeling and compensation of bias drift in MEMS inertial sensors. In *RAST 2009 - Proceedings of 4th International Conference on Recent Advances Space Technologies*. doi:10.1109/RAST.2009.5158260
- Günhan, Y., & Ünsal, D. (2014). Polynomial degree determination for temperature dependent error compensation of inertial sensors. In *Record - IEEE PLANS, Position Location and Navigation Symposium*. doi:10.1109/PLANS.2014.6851494
- Hagan, M. T., Demuth, H. B., & Beale, M. H. (1996). *Neural network design*, Boston: PWS Publishing Co.
- Hasan, A. M., Samsudin, K., Ramli, A. R., Azmir, R. S., & Ismaeel, S. A. (2009). A review of navigation systems (integration and algorithms). *Australian Journal of Basic and Applied Sciences*, **3**(2), 943–959.
- Hecht-Nielsen, R. (1992). Theory of the Backpropagation Neural Network. *Neural*

*Networks for Perception*, 65–93.

- Humphreys, T. (2012). *Statement on the vulnerability of civil unmanned aerial vehicles and other systems to civil GPS spoofing. Submitted to the Subcommittee on Oversight, Investigations, and Management of the House Committee on Homeland Security.*
- ICAO. (2013). *ICAO Environmental Report 2013.*
- IEEE Standards Board. (2004). *IEEE Standard Specification Format Guide and Test Procedure for Coriolis Vibratory Gyros. IEEE Std 1431-2004.*
- IEEE Standards Coordinating Committee 27 on Time and Frequency. (2009). *IEEE Standard Definitions of Physical Quantities for Fundamental Frequency and Time Metrology - Random Instabilities. IEEE Std 1139-2008.*
- Ishihara, A. K., Jung, J., & Rios, J. (2016). Rapid Trajectory Feasibility Verification for UAS Traffic Management. In *16th AIAA Aviation Technology, Integration, and Operations Conference*. doi:10.2514/6.2016-3149
- Jafari, M. (2015). Optimal redundant sensor configuration for accuracy increasing in space inertial navigation system. *Aerospace Science and Technology*, **47**, 467–472.
- Jang, J. S. R., Sun, C. T., & Mizutani, E. (1997). *Neuro-Fuzzy and Soft Computing-A Computational Approach to Learning and Machine Intelligence*, New Jersey: Prentice Hall.
- Jarrell, J., Gu, Y., Seanor, B., & Napolitano, M. (2008). Aircraft Attitude, Position, and Velocity Determination Using Sensor Fusion. In *AIAA Guidance, Navigation and Control Conference and Exhibit*, American Institute of Aeronautics and Astronautics. doi:doi:10.2514/6.2008-7422
- Joint Air Power Competence Centre. (2010). *Strategic Concept of Employment for Unmanned Aircraft Systems in NATO.*
- Joo, J. W., & Choa, S. H. (2007). Deformation behavior of MEMS gyroscope sensor package subjected to temperature change. *IEEE Transactions on Components and Packaging Technologies*, **30**(2), 346–354.
- Karayiannis, N. B. (1997). A methodology for constructing fuzzy algorithms for learning vector quantization. *IEEE Transactions on Neural Networks*, **8**(3), 505–518.
- Kelner, J. M., & Ziółkowski, C. (2017). Doppler effect-based automatic landing procedure for UAV in difficult access environments. *Journal of Advanced Transportation*, **2017**, 9.

- Kendoul, F. (2012). Survey of advances in guidance, navigation, and control of unmanned rotorcraft systems. *Journal of Field Robotics*, **29**(2), 315–378.
- Kim, H.-S., Bu, S.-C., Jee, G.-I., & Park, C. G. (2003). An ultra-tightly coupled GPS/INS integration using federated Kalman filter. In *Proceedings of the 16th International Technical Meeting of the Satellite Division of The Institute of Navigation (ION GPS/GNSS 2003)*.
- Kohonen, T. (1989). *Self-organization and Associative Memory: 3rd Edition*, Berlin, Heidelberg: Springer-Verlag.
- Kohonen, T. (1990). Improved versions of learning vector quantization. *Proceedings of the International Joint Conference on Neural Networks*. doi:10.1109/IJCNN.1990.137622
- Kopardekar, P., Rios, J., Prevot, T., Johnson, M., Jung, J., & Robinson, J. E. (2016). Unmanned aircraft system traffic management (UTM) concept of operations. *16th AIAA Aviation Technology, Integration, and Operations Conference*, 1–16.
- KVH. (2014). *Guide to comparing gyro and IMU technologies – Micro-electro-mechanical systems and fiber optic gyros*.
- Lacher, A., Zeitlin, A., & Maroney, D. (2010). *Airspace integration alternatives for unmanned aircraft*. Center for Advanced Aviation System Development, The MITRE Corporation.
- LeCun, Y. A., Bengio, Y., & Hinton, G. E. (2015). Deep learning. *Nature*, **521**(7553), 436–444.
- Lee, Y. C., & Ericson, S. D. (2004). Analysis of coast times upon loss of GPS signals for integrated GPS/inertial systems. *Air Traffic Control Quarterly*, **12**(1), 27–51.
- Lee, Y. C., & O’Laughlin, D. G. (2000). Performance Analysis of a Tightly Coupled GPS/Inertial System for Two Integrity Monitoring Methods. *Navigation*, **47**(3), 175–189.
- Leonard, J., Savvaris, A., & Tsourdos, A. (2012). Towards a fully autonomous swarm of unmanned aerial vehicles. In *Proceedings of the 2012 UKACC International Conference on Control, CONTROL 2012*. doi:10.1109/CONTROL.2012.6334644
- Leonard, J., Savvaris, A., & Tsourdos, A. (2014). Energy management in swarm of unmanned aerial vehicles. *Journal of Intelligent and Robotic Systems: Theory and Applications*, **74**, 233–250.
- Maenaka, K., Fujita, T., Konishi, Y., & Maeda, M. (1996). Analysis of a highly sensitive

- silicon gyroscope with cantilever beam as vibrating mass. *Sensors and Actuators, A: Physical*, **54**(1–3), 568–573.
- Malandrakis, K., Dixon, R., Savvaris, A., & Tsourdos, A. (2016). Design and Development of a Novel Spherical UAV. *IFAC-PapersOnLine*, **49**(17), 320–325.
- Manfred, M., & Ryno, T. (2008). Tightly Coupled GPS/IRS Navigation for ADS-B. In *2008 Integrated Communications, Navigation and Surveillance Conference*.
- Melega, M., Lazarus, S., Lone, M., & Savvaris, A. (2014). Autonomous sense & avoid capabilities based on aircraft performances estimation. *Proceedings of the Institution of Mechanical Engineers, Part G: Journal of Aerospace Engineering*, **228**(4), 492–517.
- Melega, M., Lazarus, S., & Savvaris, A. (2011). Autonomous collision avoidance based on aircraft performances estimation. In *AIAA/IEEE Digital Avionics Systems Conference - Proceedings*. doi:10.1109/DASC.2011.6096077
- Melega, M., Lazarus, S., Savvaris, A., & Tsourdos, A. (2015). Multiple Threats Sense and Avoid Algorithm for Static and Dynamic Obstacles. *Journal of Intelligent and Robotic Systems: Theory and Applications*, **77**(1), 215–228.
- Melin, P., Amezcua, J., Valdez, F., & Castillo, O. (2014). A new neural network model based on the LVQ algorithm for multi-class classification of arrhythmias. *Information Sciences*, **279**, 483–497.
- METI. (2017). *UTM Project in Japan*.
- Ministry of Defence, & Military Aviation Authority. (2016). *Regulatory Article (RA) 1600: remotely piloted air systems (RPAS)*, United Kingdom.
- Moir, I., Seabridge, A., & Jukes, M. (2013). *Civil Avionics Systems*, John Wiley & Sons. doi:10.1002/9781118536704
- Mueller, E. (2016). Chapter 34. In *Unmanned aircraft systems*, John Wiley & Sons.
- Murphy, J. R., Otto, N., Jovic, S., & Carniol, T. (2016a). Demonstration of an Adaptable NextGen Interface for the UAS Ground Control Station. In *16th AIAA Aviation Technology, Integration, and Operations Conference*, American Institute of Aeronautics and Astronautics. doi:10.2514/6.2016-3293
- Murphy, J. R., & Otto, N. M. (2017). Evolution of A Distributed Live, Virtual, Constructive Environment for Human in the Loop Unmanned Aircraft Testing. In *RAeS Modelling and Simulation in Air Traffic Management Conference*.

- Murphy, J. R., Williams-Hayes, P. S., Kim, S. K., Bridges, W., & Marston, M. (2016b). Flight Test Overview for UAS Integration in the NAS Project. In *AIAA Atmospheric Flight Mechanics Conference*. doi:10.2514/6.2016-1756
- Mutuel, L. H., Neri, P., & Paricaud, E. (2013). Initial 4D Trajectory Management Concept Evaluation. In *Tenth USA/Europe Air Traffic Management Research and Development Seminar*.
- NASA. (2006). Past Projects: HALE ROA in the NAS. Retrieved from [https://www.nasa.gov/centers/dryden/research/HALE\\_ROA/index.html](https://www.nasa.gov/centers/dryden/research/HALE_ROA/index.html)
- NASA. (2016). *UAS-NAS Flight Test Series 3, UAS-NAS Flight Test Series 3, Test Environment Report, Document No. UAS-ITE-5.1-016-001*.
- Navia, J., Mondragon, I., Patino, D., & Colorado, J. (2016). Multispectral mapping in agriculture: Terrain mosaic using an autonomous quadcopter UAV. In *2016 International Conference on Unmanned Aircraft Systems, ICUAS 2016*, pp. 1351–1358.
- Nikiforov, I. V. (1995). A generalized change detection problem. *IEEE Transactions on Information Theory*, **41**(1), 171–187.
- Niu, X., Li, Y., Zhang, H., Wang, Q., & Ban, Y. (2013). Fast thermal calibration of low-grade inertial sensors and inertial measurement units. *Sensors (Basel, Switzerland)*, **13**(9), 12192–12217.
- Niu, X., Nassar, S., & El-Sheimy, N. (2007). An Accurate Land-Vehicle MEMS IMU/GPS Navigation System Using 3D Auxiliary Velocity Updates. *Journal of the Institute of Navigation*, **54**(3), 177–188.
- Nova, D., & Estévez, P. A. (2013). A review of learning vector quantization classifiers. *Neural Computing and Applications*, **25**(3–4), 511–524.
- NovAtel. (2018). An introduction to GNSS: GPS, GLONASS, BeiDou, Galileo and other Global Navigation Satellite Systems. <https://www.novatel.com/an-introduction-to-gnss/chapter-4-gnss-error-sources/error-sources/>.
- Ochieng, W. Y., Sauer, K., Walsh, D., Brodin, G., Griffin, S., & Denney, M. (2003). GPS integrity and potential impact on aviation safety. *Journal of Navigation*. doi:10.1017/S0373463302002096
- Opromolla, R., Fasano, G., & Accardo, D. (2018). A Vision-Based Approach to UAV Detection and Tracking in Cooperative Applications. *Sensors (Basel, Switzerland)*,

**18(10).**

- Panagiotakopoulos, D., Majumdar, A., & Ochieng, W. Y. (2013). Extreme value theory-based integrity monitoring of global navigation satellite systems. *GPS Solutions*, **18**(1), 133–145.
- Pany, T., & Eissfeller, B. (2006). Use of a vector delay lock loop receiver for GNSS signal power analysis in bad signal conditions. In *IEEE PLANS, Position Location and Navigation Symposium*, pp. 893–903.
- Passaro, V. M. N., Cuccovillo, A., Vaiani, L., De Carlo, M., & Campanella, C. E. (2017). Gyroscope technology and applications: A review in the industrial perspective. *Sensors (Switzerland)*, **17**(10). doi:10.3390/s17102284
- Pastor, E., Perez-Battle, M., Royo, P., Cuadrado, R., & Barrado, C. (2014). Real-time simulations to evaluate the RPAS integration in shared airspace. In *SIDs 2014 - Proceedings of the SESAR Innovation Days*.
- Paulson, C. A., Sóbester, A., & Scanlan, J. P. (2017). The rapid development of bespoke small unmanned aircraft. *The Aeronautical Journal*, **121**(1245), 1683–1710.
- Prevot, T., Rios, J., Kopardekar, P., Robinson III, J. E., Johnson, M., & Jung, J. (2016). UAS Traffic Management (UTM) Concept of Operations to Safely Enable Low Altitude Flight Operations. In *16th AIAA Aviation Technology, Integration, and Operations Conference*. doi:10.2514/6.2016-3292
- RAMA UAV Control System. (2009). Control System Architecture. Retrieved October 25, 2018, from [http://rttime.felk.cvut.cz/helicopter/control\\_system\\_architecture](http://rttime.felk.cvut.cz/helicopter/control_system_architecture)
- Ren, L., Castillo-Effen, M., Yu, H., ... Ippolito, C. A. (2017). Small Unmanned Aircraft System (sUAS) Trajectory Modeling in Support of UAS Traffic Management (UTM). In *17th AIAA Aviation Technology, Integration, and Operations Conference*. doi:10.2514/6.2017-4268
- Rhudy, M., Gross, J., Gu, Y., & Napolitano, M. (2012). Fusion of GPS and Redundant IMU Data for Attitude Estimation. In *AIAA Guidance, Navigation, and Control Conference*. doi:10.2514/6.2012-5030
- Ristic, B., Arulampalam, M., & Gordon, A. (2004). *Beyond Kalman Filters: Particle Filters for Target Tracking*. doi:10.1159/000170955
- Royo, P., Cuadrado, R., Barrado, C., Salamí, E., Pérez-Battle, M., & Pastor, E. (2013). Towards the automation of the UAS mission management. In *AIAA/IEEE Digital*

- Avionics Systems Conference - Proceedings*. doi:10.1109/DASC.2013.6712626
- Ruff, H. A., Narayanan, S., & Draper, M. H. (2002). Human interaction with levels of automation and decision-aid fidelity in the supervisory control of multiple simulated unmanned air vehicles. *Presence: Teleoperators and Virtual Environments*, **11**(4), 335–351.
- Ryan, M. W., & Miller, G. (2010). MEMS based AHRS with adaptive bias estimation for high performance rate sensor replacement. In *IEEE PLANS, Position Location and Navigation Symposium*, pp. 214–220.
- Sabatini, R., Moore, T., & Hill, C. (2013a). A New Avionics-Based GNSS Integrity Augmentation System: Part 1 – Fundamentals. *Journal of Navigation*, **66**(3), 363–384.
- Sabatini, R., Moore, T., & Hill, C. (2013b). A new avionics-based GNSS integrity augmentation system: Part 2 - Integrity flags. *Journal of Navigation*, **66**(4), 501–522.
- Sabatini, R., Moore, T., Hill, C., & Ramasamy, S. (2015). Assessing avionics-based GNSS integrity augmentation performance in UAS mission- and safety-critical tasks. In *2015 International Conference on Unmanned Aircraft Systems, ICUAS 2015*, pp. 650–659.
- Salamí, E., Barrado, C., & Pastor, E. (2014). UAV flight experiments applied to the remote sensing of vegetated areas. *Remote Sensing*, **6**(11), 11051–11081.
- Santamaria, E., Royo, P., Barrado, C., & Pastor, E. (2009). An Integrated Mission Management System for UAS civil applications. In *AIAA Guidance, Navigation, and Control Conference and Exhibit*.
- Savage, P. G. (1998). Strapdown Inertial Navigation Integration Algorithm Design Part 1 : Attitude Algorithms. *Journal of Guidance, Control, and Dynamics (AIAA)*, **21**(1), 19–28.
- Savvaris, A., Xie, Y., Malandrakis, K., Lopez, M., & Tsourdos, A. (2016). Development of a fuel cell hybrid-powered unmanned aerial vehicle. In *24th Mediterranean Conference on Control and Automation, MED 2016*. doi:10.1109/MED.2016.7536038
- Schmidt, G. T. (2010). *INS / GPS Technology Trends. NATO RTO Lecture Series*.
- Schmidt, G. T. (2015). Navigation sensors and systems in GNSS degraded and denied environments. *Chinese Journal of Aeronautics*, **28**(1), 1–10.
- SESAR. (2012a). *European ATM Master Plan - Edition 2. The Roadmap for Sustainable Air Traffic Management*.
- SESAR. (2012b). *Factsheet: I-4D - Flying a new dimension*.

- SESAR. (2015). *E.02.34-D08 ERAINT Project Closeout Report*.
- Shcheglov, K., Evans, C., Gutierrez, R., & Tang, T. K. (2000). Temperature dependent characteristics of the JPL silicon MEMS gyroscope. In *2000 IEEE Aerospace Conference. Proceedings (Cat. No.00TH8484)*. doi:10.1109/AERO.2000.879420
- Shen, X., & Chen, J. (2009). Study on prediction of traffic congestion based on LVQ neural network. In *2009 International Conference on Measuring Technology and Mechatronics Automation, ICMTMA 2009*. doi:10.1109/ICMTMA.2009.242
- Sheng, H., & Zhang, T. (2015). MEMS-based low-cost strap-down AHRS research. *Measurement*, **59**, 63–72.
- Skinner, S. W., Urdahl, S., Harrington, T., Balchanos, M. G., Garcia, E., & Mavris, D. N. (2018). UAV Swarms for Migration Flow Monitoring and Search and Rescue Mission Support. In *2018 AIAA Information Systems-AIAA Infotech @ Aerospace*. doi:10.2514/6.2018-1489
- Sotak, M. (2010). Testing the coarse alignment algorithm using rotation platform. *Acta Polytechnica Hungarica*, **7**(5), 87–107.
- SPH Engineering. (2018). *UgCS User Manual*.
- Stansbury, R., Wilson, T., & Tanis, W. (2009). A Technology Survey of Emergency Recovery and Flight Termination Systems for UAS. In *AIAA Infotech@Aerospace Conference*. doi:10.2514/6.2009-2038
- STMicroelectronics. (2017). STEVAL-STLKT01V1 SensorTile development kit.
- Tang, Q. J., Wang, X. J., Yang, Q. P., & Liu, C. Z. (2014). Static temperature analysis and compensation of MEMS gyroscopes. *International Journal of Metrology and Quality Engineering*, **4**(3), 209–214.
- Thompson, R. M. I. (2015). *Domestic Drones and Privacy: A Primer*. Congressional Research Service.
- Tirri, A. E. (2014). *Exploiting innovative sensor data fusion techniques for Sense and Avoid units to be installed on-board Unmanned Aerial Systems*, Università degli Studi di Napoli Federico II.
- Titterton, D. H., & Weston, J. L. (2004). *Strapdown Inertial Navigation Technology*, 2nd edn, The American Institute of Aeronautics and Astronautics. doi:10.1049/PBRA017E
- Tyagi, A., Ayyalasomayajula, S., Nigam, N., Zhang, C., & Hwang, I. (2017). Predicting Trajectories for Small Electric UASs for Safety Analyses. In *17th AIAA Aviation*

- Technology, Integration, and Operations Conference*, American Institute of Aeronautics and Astronautics. doi:10.2514/6.2017-4267
- U.S. Government Accountability Office. (2012). *Unmanned Aircraft Systems: Use in the National Airspace System and the Role of the Department of Homeland Security*.
- Vergouw, B., Nagel, H., Bondt, G., & Custers, B. (2016). Drone Technology: Types, Payloads, Applications, Frequency Spectrum Issues and Future Developments. *The Future of Drone Use*, **27**, 21–45.
- Vetrella, A. R., Fasano, G., & Accardo, D. (2016). Cooperative navigation in GPS-challenging environments exploiting position broadcast and vision-based tracking. In *2016 International Conference on Unmanned Aircraft Systems, ICUAS 2016*, pp. 447–456.
- Vetrella, A. R., Fasano, G., Renga, A., & Accardo, D. (2015a). Cooperative UAV navigation based on distributed multi-antenna GNSS, vision, and MEMS sensors. In *2015 International Conference on Unmanned Aircraft Systems, ICUAS 2015*, pp. 1128–1137.
- Vetrella, A. R., Savvaris, A., Fasano, G., & Accardo, D. (2015b). RGB-D camera-based quadrotor navigation in GPS-denied and low light environments using known 3D markers. In *2015 International Conference on Unmanned Aircraft Systems, ICUAS 2015*. doi:10.1109/ICUAS.2015.7152290
- Von Bueren, S., & Yule, I. (2012). *Multispectral aerial imaging of pasture quality and biomass using unmanned aerial vehicles (UAV). Accurate and Efficient Use of Nutrients on Farms, Occasional Report*.
- Wahdan, A., Georgy, J., Abdelfatah, W. F., & Noureldin, A. (2014). Magnetometer calibration for portable navigation devices in vehicles using a fast and autonomous technique. *IEEE Transactions on Intelligent Transportation Systems*, **15**(5), 2347–2352.
- Wander, A., & Förstner, R. (2013). Innovative fault detection, isolation and recovery on-board spacecraft: Study and implementation using cognitive automation. In *Conference on Control and Fault-Tolerant Systems, SysTol*, pp. 336–341.
- Wang, L., Hao, Y., Wei, Z., & Wang, F. (2010). Thermal calibration of MEMS inertial sensors for an FPGA-based navigation system. In *Proceedings - 3rd International Conference on Intelligent Networks and Intelligent Systems, ICINIS 2010*, pp. 139–

143.

- Wang, W., Liu, S., Luo, Z., ... Wu, X. (2014). Modeling and analysis of frequency shift of MEMS gyroscope subjected to temperature change. In *Proceedings - Electronic Components and Technology Conference*. doi:10.1109/ECTC.2014.6897616
- Wang, Z., Zhao, H., Qiu, S., & Gao, Q. (2015). Stance-Phase Detection for ZUPT-Aided Foot-Mounted Pedestrian Navigation System. *IEEE/ASME Transactions on Mechatronics*, **20**(6), 3170–3181.
- Wargo, C. A., Church, G. C., Glaneueski, J., & Strout, M. (2014). Unmanned Aircraft Systems (UAS) research and future analysis. In *IEEE Aerospace Conference Proceedings*. doi:10.1109/AERO.2014.6836448
- Weibel, R. E., & Hansman, R. J. (2005). *Safety Considerations for Operation of Unmanned Aerial Vehicles in the National Airspace System*. MIT International Center for Air Transportation.
- Weiss, Neil A., and C. A. W. (2001). *Elementary Statistics*, 4 th ed., Addison-Wesley Longman Publishing Co.,Inc., MA.
- Wertz, J. R. (1978). *Spacecraft attitude determination and control*, Kluwer Academic Publishers, The Netherlands. doi:10.1007/978-94-009-9907-7
- Wheeler, D. O. (2016). Chapter 14. In *Unmanned aircraft systems*, John Wiley & Sons.
- Wilamowski, B. M., & Yu, H. Y. H. (2010). Improved computation for Levenberg-Marquardt training. *IEEE Transactions on Neural Networks*, **21**(6), 930–937.
- Xia, D., Chen, S., Wang, S., & Li, H. (2009). Microgyroscope temperature effects and compensation-control methods. *Sensors*, **9**(10), 8349–8376.
- Xue, M. (2017). UAV Trajectory Modeling Using Neural Networks. In *17th AIAA Aviation Technology, Integration, and Operations Conference*. doi:10.2514/6.2017-3072
- Zhang, C. X., Li, Y., Mumford, P., & Rizos, C. (2008). Allan Variance Analysis on Error Characters of MEMS Inertial Sensors for an FPGA-based GPS/INS System. *Int. Symp. on GPS/GNSS*, 127–133.
- Zhang, Q., Tan, Z., & Guo, L. (2009). Compensation of temperature drift of MEMS gyroscope using BP neural network. In *Proceedings - 2009 International Conference on Information Engineering and Computer Science, ICIECS 2009*. doi:10.1109/ICIECS.2009.5365140
- Zhuang, Y., & El-Sheimy, N. (2016). Tightly-Coupled Integration of WiFi and MEMS

Sensors on Handheld Devices for Indoor Pedestrian Navigation. *IEEE Sensors Journal*, **16**(1), 224–234.